

A cold atom electron source

Citation for published version (APA):

Taban, G. (2009). *A cold atom electron source*. [Phd Thesis 1 (Research TU/e / Graduation TU/e), Applied Physics and Science Education]. Technische Universiteit Eindhoven. <https://doi.org/10.6100/IR641383>

DOI:

[10.6100/IR641383](https://doi.org/10.6100/IR641383)

Document status and date:

Published: 01/01/2009

Document Version:

Publisher's PDF, also known as Version of Record (includes final page, issue and volume numbers)

Please check the document version of this publication:

- A submitted manuscript is the version of the article upon submission and before peer-review. There can be important differences between the submitted version and the official published version of record. People interested in the research are advised to contact the author for the final version of the publication, or visit the DOI to the publisher's website.
- The final author version and the galley proof are versions of the publication after peer review.
- The final published version features the final layout of the paper including the volume, issue and page numbers.

[Link to publication](#)

General rights

Copyright and moral rights for the publications made accessible in the public portal are retained by the authors and/or other copyright owners and it is a condition of accessing publications that users recognise and abide by the legal requirements associated with these rights.

- Users may download and print one copy of any publication from the public portal for the purpose of private study or research.
- You may not further distribute the material or use it for any profit-making activity or commercial gain
- You may freely distribute the URL identifying the publication in the public portal.

If the publication is distributed under the terms of Article 25fa of the Dutch Copyright Act, indicated by the "Taverne" license above, please follow below link for the End User Agreement:

www.tue.nl/taverne

Take down policy

If you believe that this document breaches copyright please contact us at:

openaccess@tue.nl

providing details and we will investigate your claim.

A Cold Atom Electron Source

PROEFSCHRIFT

ter verkrijging van de graad van doctor aan de
Technische Universiteit Eindhoven, op gezag van de
Rector Magnificus, prof.dr.ir. C.J. van Duijn, voor een
commissie aangewezen door het College voor
Promoties in het openbaar te verdedigen
op dinsdag 7 april 2009 om 16.00 uur

door

Gabriel Taban

geboren te Focşani, Roemenië

Dit proefschrift is goedgekeurd door de promotor:

prof.dr. H.C.W. Beijerinck

Copromotoren:

dr.ir. E.J.D. Vredenburgt

en

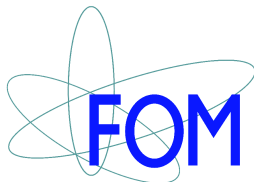
dr.ir. O.J. Luiten

Druk: Universiteitsdrukkerij Technische Universiteit Eindhoven

Ontwerp omslag: G. Taban & Oranje Vormgevers.

A catalogue record is available from the Eindhoven University of Technology Library

ISBN: 978-90-386-1612-4



The work described in this thesis has been carried out at the Physics Department of the Eindhoven University of Technology, and is part of the research program of the 'Stichting voor Fundamenteel Onderzoek der Materie' (FOM), which is financially supported by the 'Nederlandse Organisatie voor Wetenschappelijk Onderzoek' (NWO).

Contents

1 Pulsed bright electron sources	1
1.1 Phase-space and brightness	1
1.1.1 Phase-space description of a beam	1
1.1.2 Definition of brightness	3
1.2 Applications of pulsed bright electron sources	6
1.2.1 Ultrafast electron diffraction	6
1.2.2 X-ray free electron laser	8
1.3 Overview of pulsed bright electron sources	9
1.3.1 Photo-emission sources	10
1.3.2 Field-emission sources	11
1.4 Limitations of the present pulsed electron sources	12
1.5 New approach: cold electron source	13
Bibliography	13
2 Basic principles of an electron source based on ultracold plasma	15
2.1 The new electron source based on ultracold plasma	15
2.2 The steps to produce an ultracold plasma	16
2.2.1 Laser cooling	16
2.2.2 Magneto-optical trapping	18
2.2.3 Rubidium atoms	18
2.2.4 Ultracold plasma formation	19
2.3 Expectations from the cold atom electron source	22
2.4 This Thesis	24
Bibliography	26
3 Design and validation of an accelerator for an ultracold electron source	29
3.1 Bright electron sources and their applications	30
3.2 Accelerator design	31
3.3 Fast high voltage generation	35
3.4 Electric field measurement	37
3.4.1 Static electric field measurement with cold ions	37
3.4.2 Pulsed electric field measurement with Pockels effect	39

3.5	Valorization of the design	42
3.6	Conclusions and outlook	43
	Bibliography	44
4	Pulsed photoionization source	47
4.1	Introduction	48
4.1.1	Cold electron sources	48
4.1.2	This experiment: an overview	49
4.2	Experimental setup	50
4.2.1	Electron production from cold atoms	50
4.2.2	Charged particle beamline	52
4.2.3	Electron bunches detection	54
4.3	The experimental method for the source temperature measurement	56
4.3.1	Size dependent measurement	57
4.3.2	Size independent measurement	57
4.3.3	Image analysis	58
4.4	Experimental results	58
4.5	Discussion	61
4.6	Conclusions and outlook	64
	Bibliography	65
5	Pulsed field-ionization source	67
5.1	Cold electron sources	68
5.1.1	The new idea of a cold electron source	68
5.1.2	This experiment: an overview	69
5.2	Experimental setup	69
5.2.1	Electron production from cold atoms	69
5.2.2	Charged particle beamline	72
5.2.3	Electron bunch detection	73
5.3	Measurement procedure	75
5.3.1	Temperature determination using different Rydberg states	75
5.3.2	Beam energy measurement	76
5.3.3	Data analysis	78
5.4	Experimental results	80
5.5	Conclusions and outlook	81
	Bibliography	82
6	High energy bunches	83
6.1	Introduction	84
6.2	Experimental setup	85
6.2.1	Production of high energy electron bunches from Rydberg atoms	85
6.2.2	Einzel lens	86
6.2.3	Optical matrix	87

6.3	Method	87
6.4	Results	88
6.5	Conclusions	91
	Bibliography	92
7	Concluding remarks	93
7.1	Improvements and limitations	94
7.2	New directions opened by this project	96
	Bibliography	97
	Summary	99
	Samenvatting	103
	Dankwoord	107
	Curriculum vitae	111

Pulsed bright electron sources

Pulsed bright electron sources offer the possibility to study the structure of matter in great spatial and temporal detail, directly or indirectly. For example, to generate hard X-ray flashes with high brilliance, a new Free Electron Laser facility is under construction [1]. It requires an electron source with a very high quality. Electron beams may also be used directly to study matter with, e.g., ultrafast electron diffraction [2]. This also requires a pulsed electron source with high brightness.

Brightness is an important figure of merit for electron source quality. It is expressed in its most general form as the current density per unit solid angle and unit energy spread. Recent brightness improvements are based on increasing the current density at the source [3], [4], [5], but this is not sufficient for all types of experiments. While the sources based on photo-emission and field-emission are developed to a high degree of quality, in this Thesis an entirely new path is explored. The new approach employs an ultracold plasma as a source of electrons. Till now, ultracold plasmas have mainly been the subject of fundamental research. This project investigates whether ultracold plasma has the potential of improving the quality of state-of-the-art electron sources. This Thesis presents the new concept and the first advances towards the realization of a bright, pulsed electron source.

In this Chapter we show the present possibilities of pulsed electron sources.

1.1 Phase-space and brightness

Before we start presenting the technical aspects of the pulsed electron sources development in some detail, first the quality of a source has to be defined, so that different types can be compared.

1.1.1 Phase-space description of a beam

The motion of a charge particle is generally described by an equation of motion with $x(t)$, $y(t)$, and $z(t)$ position coordinates as function of time. For a large number of particles it is not effective to describe their motion with this equation of motion. Another representation

uses the particle trajectories in a six-dimensional space with coordinates in both position and velocity $x, y, z, v_x, v_y,$ and v_z . This is called the phase-space. At a certain moment, a particle is therefore represented as a point in phase-space.

The quality of the beam is defined as the effective volume occupied by a distribution in a six-dimensional phase-space. The smaller the volume, the better. Here, the term quality means focusability or parallelism for the transverse (x and y) degrees of freedom. When a beam propagates through a series of linear lenses and drift spaces, a linear optical component can always restore the distribution to its original representation. Processes that increase the phase-space volume are undesirable. Irreversible processes lead to emittance growth of a distribution, meaning that they degrade the parallelism of a beam. Therefore the final emittance of a beam on a detector represents the sum of the intrinsic emittance from the source and emittance growth during acceleration.

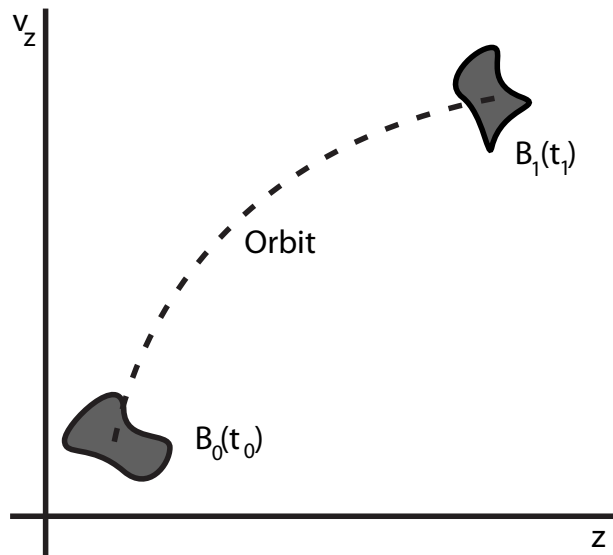


Figure 1.1: The phase-space volume conservation at two different moments. With the dashed line the trajectory of a single particle is represented.

Conservation of the phase-space volume occupied by a particle distribution is a fundamental phenomenon known as the Liouville's theorem. Fig. 1.1 illustrates the concept of phase-space volume conservation, here actually for a two-dimensional phase-space. At the initial moment t_0 , a set of particles in phase-space is represented by a boundary B_0 . At a moment t_1 , the particle positions and velocities have changed. The dashed line in Fig. 1.1 indicates the phase-space motion of a particle orbit as time evolves. The set can be represented by another boundary B_1 . The theorem of phase-space conservation states that the area enclosed by B_1 is equal to the original area B_0 . It is important to note that the theorem is valid only when the number of particles in a phase-volume is large; the forces on particles vary smoothly in space and time, i.e., there are no collisions; and the frictional forces that depend on particle velocity are excluded. The conservation of phase-space volume implies that a bunch is incompressible in phase-space. The incompress-

sibility condition is equivalent to saying that the 6D density distribution function $f(\vec{r}, \vec{p})$ is constant if a particle trajectory is followed.

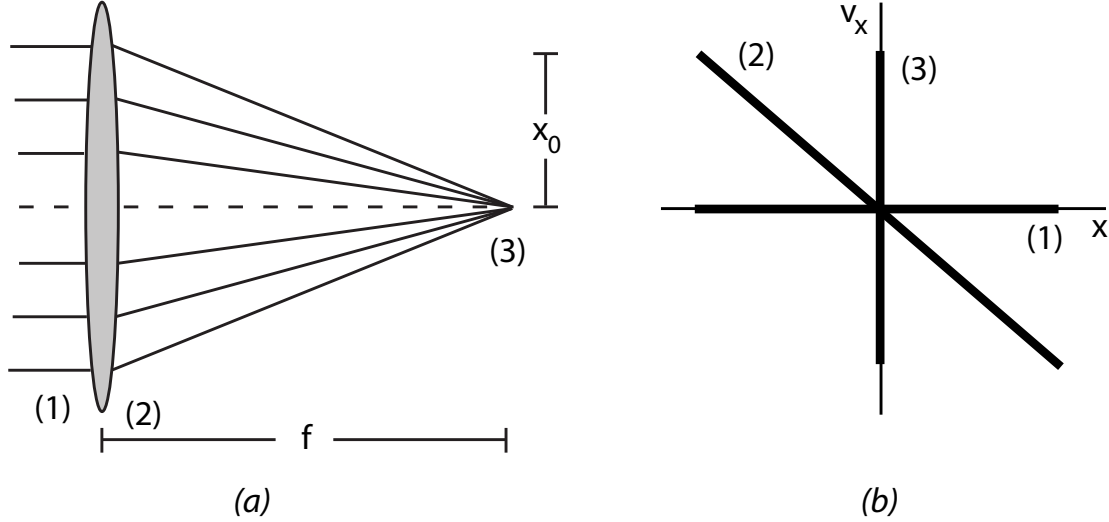


Figure 1.2: Representation of a laminar beam that is focused by a lens: (a) The particles trajectories; (b) The phase-space representation at three different positions represented in (a).

An ideal classical particle beam has a laminar flow, i.e., the orbits do not intersect each other except in the focus, or in other words, the phase-space volume is zero. For such an ideal beam, all the particles at a certain position have the same transverse velocity, which in turn is linearly proportional with the displacement from the symmetry axis. Consider a laminar beam with a width $2x_0$ which is parallel and is focused by a positive lens with focal length f (Fig. 1.2(a)). Its phase-space representation is shown in Fig. 1.2(b) at three different positions. When the beam is parallel (1), it is represented as an horizontal line with dimension zero in v_x , meaning no transverse velocity. Till converging to the focus (3), where the phase-space representation is aligned with the v_x axis at the focal point, the beam is rotated in the phase-space representation (2). At focus, the distribution has the x -dimension equal to zero, because a laminar beam can be focused by an ideal lens to a point of zero dimension.

For a realistic non-laminar beam of finite size, i.e., finite phase-space volume, the particles at the same point move in different directions (Fig. 1.3(a)). If they are focused by a lens, the focus is not a point as in Fig. 1.2(a), but an area with non-zero spatial dimension. The phase-space representation of a non-laminar beam is shown in Fig. 1.3(b) at three different positions. The finite size x_0 and finite divergence $\Delta\theta_0$ determine the focusability of the beam.

1.1.2 Definition of brightness

For an electron source, the parameter that describes its quality is the brightness. The 6D brightness is defined as the current density per unit solid angle and unit energy spread [6]:

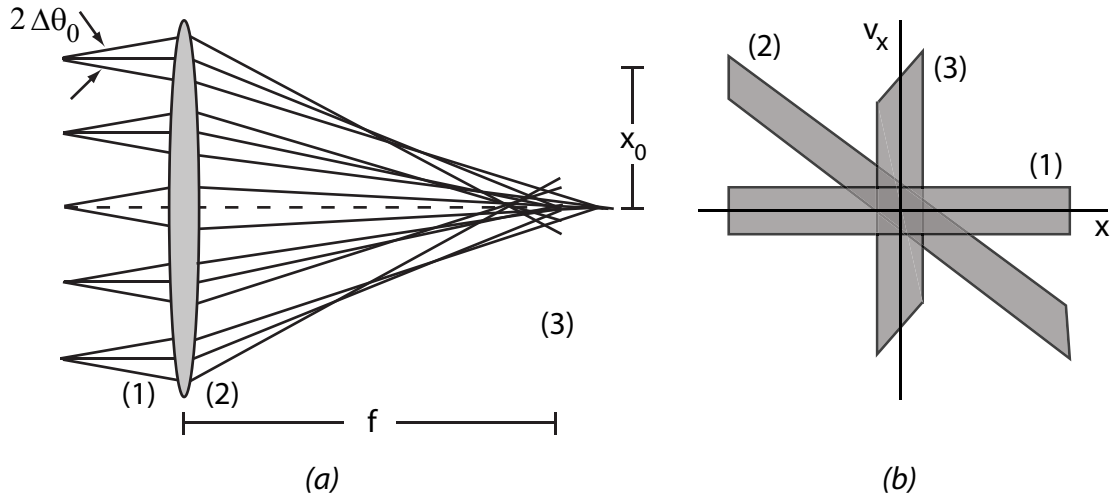


Figure 1.3: Representation of a non-laminar beam of size x_0 and divergence $\Delta\theta_0$ that is focused by a lens: (a) The particles trajectories; (b) The phase-space representation at three different positions represented in (a).

$$B \equiv \frac{I}{\Delta A \Delta \Omega \Delta U}, \quad (1.1)$$

where I is the beam current, ΔA the cross-sectional area of the beam, $\Delta \Omega$ the beam solid angle, and ΔU the energy spread. A representation of some of these parameters is shown in Fig. 1.4.

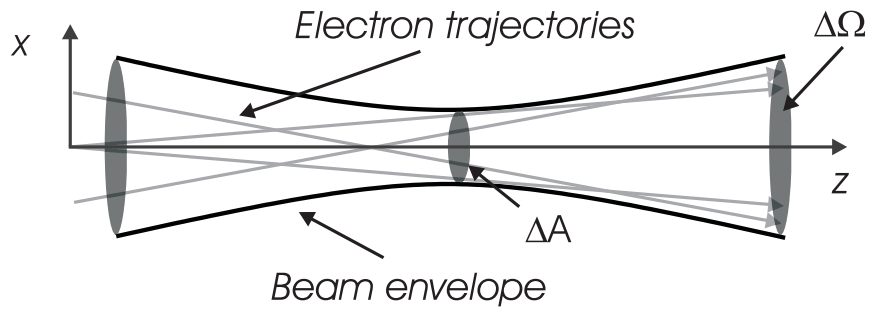


Figure 1.4: Geometry of an electron bunch at the focus. Indicated are the beam envelope and the electron trajectories. ΔA is the transverse area of the beam, and $\Delta \Omega$ the solid angle.

In [6] it is shown that the brightness B from Eq. (1.1) is proportional to the Lorentz-invariant local phase-space density $f(\vec{r}, \vec{p})$:

$$B(\vec{r}, \vec{p}) = e\beta^2\gamma^2 m^2 c^2 f(\vec{r}, \vec{p}), \quad (1.2)$$

where e and m are the electron charge and mass, respectively, c the speed of light, $\beta \equiv v/c$,

$\gamma \equiv 1/\sqrt{1-\beta^2}$ the Lorentz factor, and $f(\vec{r}, \vec{p})$ is normalized to the number N of particles in the bunch.

The brightness from Eq. (1.2) can be normalized to the beam energy and rewritten as:

$$B_n(\vec{r}, \vec{p}) = em^2c^2 f(\vec{r}, \vec{p}) = \frac{1}{\beta^2\gamma^2} B(\vec{r}, \vec{p}). \quad (1.3)$$

For a beam in which the three degrees of freedom x , y , and z are decoupled - as is a good approximation for a freely propagating beam - and described by a Gaussian distribution, the normalized brightness of Eq. 1.3 can be written as:

$$B_n = \frac{1}{mc} \frac{Ne}{(2\pi)^3 \varepsilon_x \varepsilon_y \varepsilon_z}. \quad (1.4)$$

Here, the root-mean-square (rms) normalized emittance ε for x , y , and z directions is defined as:

$$\varepsilon_x \equiv \frac{1}{mc} \sqrt{\langle x^2 \rangle \langle p_x^2 \rangle - \langle xp_x \rangle^2}, \quad (1.5)$$

where $\langle \dots \rangle$ means averaging over the entire phase-space distribution, with x the particle transverse position and p_x its transverse momentum. Emittance ε is an energy-independent for the surface area of Fig. 1.1.

When the longitudinal energy spread, i.e., σ_{p_z} , is less important, the peak normalized transverse brightness B_\perp is instead used as the figure of merit:

$$B_\perp = \frac{I_p}{4\pi^2 \varepsilon_x \varepsilon_y}. \quad (1.6)$$

The peak current I_p for a Gaussian bunch can be calculated from the total charge $Q = Ne$ and the temporal bunch length σ_t :

$$I_p = \frac{Q}{\sqrt{2\pi}\sigma_t}. \quad (1.7)$$

If there is no correlation between position and momentum coordinates, i.e., $\langle xp_x \rangle^2 = 0$, such as in a beam waist or at the source, then Eq. (1.5) reduces to:

$$\varepsilon_x \equiv \frac{1}{mc} \sqrt{\langle x^2 \rangle \langle p_x^2 \rangle} = \frac{1}{mc} \sigma_x \sigma_{p_x}, \quad (1.8)$$

with σ_x the rms transverse beam size and σ_{p_x} the rms transverse momentum spread. For a purely thermal momentum distribution,

$$\sigma_{p_x} = \sigma_{p_y} = \sqrt{mkT}, \quad (1.9)$$

so that the normalized emittance becomes:

$$\varepsilon_x = \sigma_x \sqrt{\frac{kT}{mc^2}}. \quad (1.10)$$

Therefore, with the help of Eqs. (1.7) and (1.10), Eq. (1.6) can be rewritten as:

$$B_{\perp} = \frac{mc^2Q}{(2\pi)^{5/2}\sigma_x\sigma_y\sigma_t kT}. \quad (1.11)$$

It can be seen from Eq. (1.11) that for a pulsed high brightness electron source, the total charge Q of a bunch should be maximized, its temporal bunch length σ_t should be minimized, the rms beam size $\sigma_{x,y}$ should be minimized, and the electron temperature T should be as low as possible.

When one wants to reach the maximum possible brightness, the limitation is given by the Pauli exclusion principle, which says that no two fermions may occupy the same quantum state. The maximum phase-space density f_{max} of a fermi system is reached at $T = 0$, and it is given by $f_{max} = h^{-3}$, where h is Planck's constant. Therefore the maximum normalized brightness $B_{n,max}$ from Eq. (1.3) has the value:

$$B_{n,max} = \frac{em^2c^2}{h^3} = 6.4 \times 10^{18} \text{ A}/(\text{m}^2 \text{ sr} \cdot \text{eV}). \quad (1.12)$$

This equation is available for a polarized beam; for an unpolarized beam it is twice as high.

1.2 Applications of pulsed bright electron sources

A pulsed bright electron source is of high importance in many scientific and technological applications. Examples of state-of-the-art applications where pulsed bright electron sources play an important role are ultrafast electron diffraction (UED) [2] and X-ray free electron lasers (XFEL) [1]. The electrons or the X-rays can make it possible, for example, to gain understanding of the precise sequence of events in a chemical reaction [7]. Also such beams can be used to analyze in detail the structure of biomolecules, and even to record their structural dynamics [8]. The properties of hot plasmas and processes that take place inside the plasma can also be studied with X-ray pulses: a first X-ray pulse of extremely high intensity creates a hot plasma and a second X-ray pulse can be used to take a high resolution snapshot of the subsequent state of matter. With such pump-probe experiments, also the structural dynamics during condensed matter phase transition can be followed [9].

An overview of both applications, UED and XFEL, together with the importance of a high quality electron beam, are presented below.

1.2.1 Ultrafast electron diffraction

UED is an experimental method that can follow atomic motions in real time [2]. In a bond breaking event of a chemical reaction [7], for example, one initial molecule will dissociate into two different products. Finding the trajectories of the atoms and the relative distribution of energies requires an experimental technique with atomic scale resolution. In a time-resolved diffraction experiment as shown in Fig. 1.5, the dynamics is initiated by a laser pulse and the structure of the sample after initiation is determined by delaying the

arrival of an electron pulse with respect to the initial pulse and monitoring the diffraction pattern at the detector. The term "*molecular movie*" is broadly used to describe the relative atomic motions of a many-body system in 3D coordinates. The shortest time scale of these processes is in the order of 100 fs, the time it takes for two atoms to move one bond length.

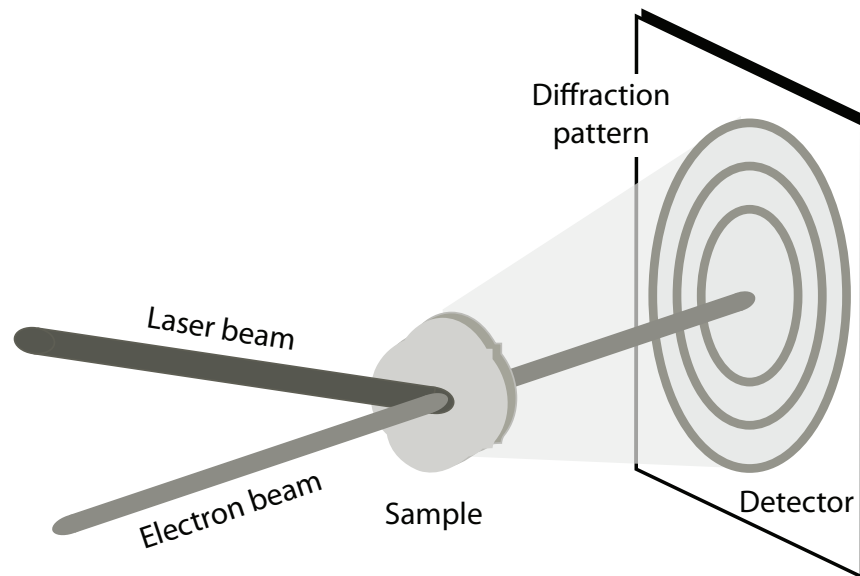


Figure 1.5: The schematic representation of an UED experiment.

It is not only challenging to generate short electrons pulses with 100 fs duration, but in particular to generate a sufficient number of electrons to be able to capture enough information with single shot experiments. In [9], for instance, 30 keV sub-picosecond electron beams were used to study the melting of aluminium initiated by an ultrafast laser pulse (Fig. 1.6). The brightness of the electron source used was such that multiple shots were needed to obtain useful information. Bunches with more than 0.1 pC charge are needed for a single shot experiment [2]. For a long time it was believed that for such bunch charges uncontrollable space-charge effects would destroy the time resolution. The solution to overcome such effects has been found in the use of ellipsoidal bunches [10]. In this way the Coulomb expansion is brought under control and made reversible. One of the first diffraction experiments that uses ellipsoidal bunches is reported in [11].

An ideal source for single shot transmission UED experiments would operate at (several) 100 keV energies, would have bunches shorter than 100 fs, and would contain a minimum of 0.1 pC electron charge. Recently, a new electron source concept for UED experiments was presented in [12], which uses ellipsoidal bunches [10] and RF compression techniques [14] to achieve these parameters. For a thermal source with 25 μm rms size and 10000 K temperature, the normalized emittance and transverse brightness of this source concept are 0.03 mm mrad and 1×10^{13} A/(m² sr), respectively. This is good enough to carry out a single-shot UED experiment with 500 μm samples with a periodicity of ~ 1 nm.

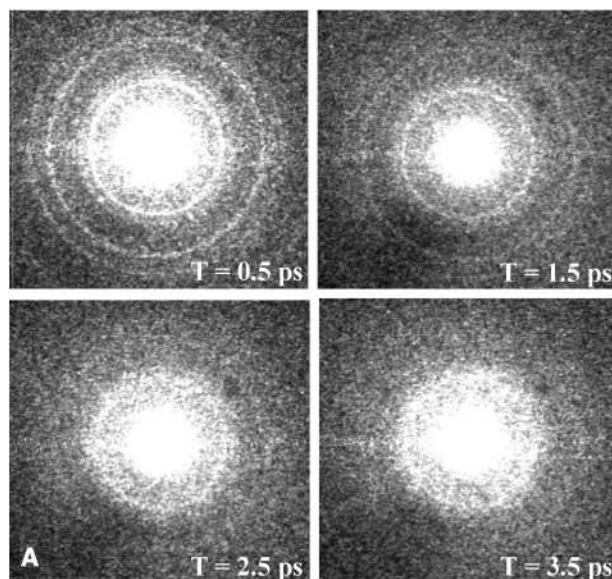


Figure 1.6: Sequence of ultrafast electron diffraction patterns of polycrystalline aluminium in a solid-liquid phase transition, taken at different pump-probe delay intervals [9].

Even with these achievements, this source is not bright enough to study biomolecules. Protein crystals, for example, have a single crystal size smaller than $100\ \mu\text{m}$ and a lattice spacing larger than $1\ \text{nm}$, and present photoemission sources are not bright enough to obtain a useful single shot diffraction pattern [15]. Achieving this goal therefore requires the development of pulsed electron sources with higher brightness.

1.2.2 X-ray free electron laser

In an XFEL [1], electron bunches moving at almost the speed of light are induced to emit short, intense X-ray flashes that exhibit laser-like properties. This radiation is also suitable for the study of the changes of matter on a very short time scale, analogous to what is possible with UED. Again, chemical reactions take place on femtosecond timescale, so very short X-ray pulses are required to follow these processes. Due to the short wavelength of the X-rays, atomic details become visible.

The basic principle of any XFEL (Fig. 1.7) is that electron beams with relativistic energies pass through a periodic, transverse magnetic field created by magnets with alternating poles. This array of magnets is called undulator. The electrons are forced to follow a sinusoidal path and consequently emit radiation. Because the electrons are moving in phase with the radiation already emitted, the emission adds coherently, which leads to the high intensities and the laser-like properties. The XFEL can operate over a large range of wavelengths, tuned by adjusting the energy of the electron beam or the periodicity of the magnetic field of the undulators.

An essential component of the XFEL is a good quality electron beam. At the European XFEL facility in Hamburg, Germany [1], the electron beam is produced by illuminating

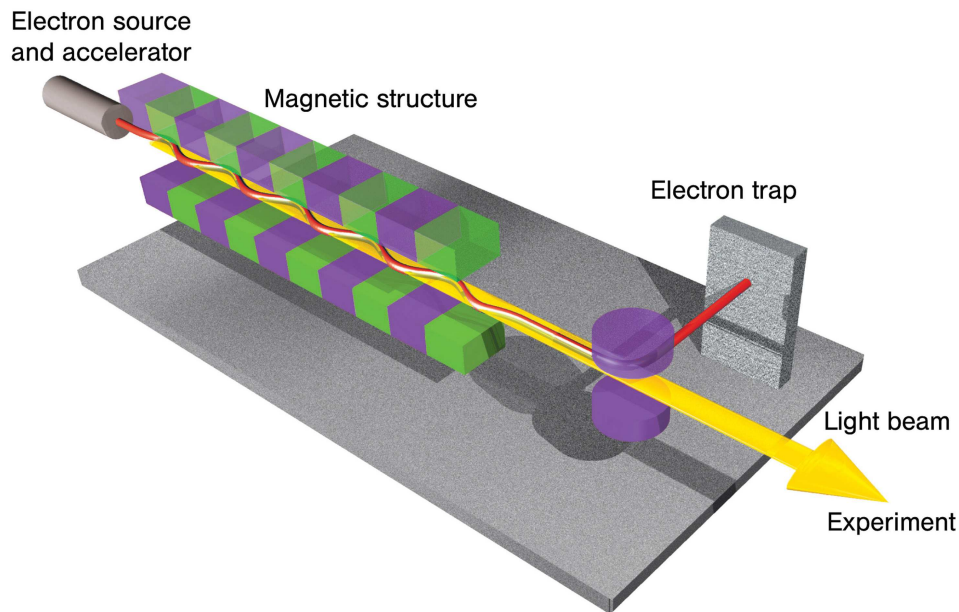


Figure 1.7: The electrons pass through a series of undulators, follow a sinusoidal path, and emit laser-like X-ray flashes. This is the basic working principle of the XFEL [1].

a metal cathode with a very short UV laser pulse in a high electric field of 60 MV/m, followed by acceleration of the generated electron pulse to 6.6 MeV in a radio-frequency (RF) gun. The beam is subsequently accelerated in many stages, reaching energies up to 20 GeV before entering the undulator. The other electron beam parameters required are a charge of 1 nC, a bunch length of ~ 100 fs, and an emittance of 1.4 mm mrad, resulting in a brightness $B_{\perp} = 5 \times 10^{13}$ A/(m² sr). It can be shown [16] that the initial emittance of the electron source is of higher importance than the current, because with a sufficiently small emittance, the electron beam energy can be decreased, together with the accelerator length. The costs for such a facility could therefore be minimized if suitable pulsed electron sources with lower emittance could be developed.

1.3 Overview of pulsed bright electron sources

As explained above, many applications benefit from a high brightness electron beam. Photo-emission and field-emission sources are the most developed techniques that produce high brightness electron bunches. Below we present a short overview of the basic principles of these two types of sources.

1.3.1 Photo-emission sources

One possibility to produce free electrons is to use the photoelectric effect by hitting the surface of a metal with a laser beam. This is the basis of all current UED experiments. A large range of energies, between 30 keV and 4 MeV are used for UED experiments [2], [11], [12]. To reach very high kinetic energies, as needed by an XFEL, the electrons are accelerated in an RF field in a so-called RF gun. An example of an RF gun is depicted in Fig. 1.8. The state-of-the-art of RF guns is the LCLS gun at SLAC [5], commissioned in 2007. The copper cathode of the LCLS gun is illuminated by a UV laser operating at 253 nm, with a repetition frequency of 30-120 Hz, an energy of 500 μJ per pulse, and a duration of the laser pulse of 6 ps FWHM (full-width-at-half-maximum). The resulting electron beam can reach a 6 MeV kinetic energy.

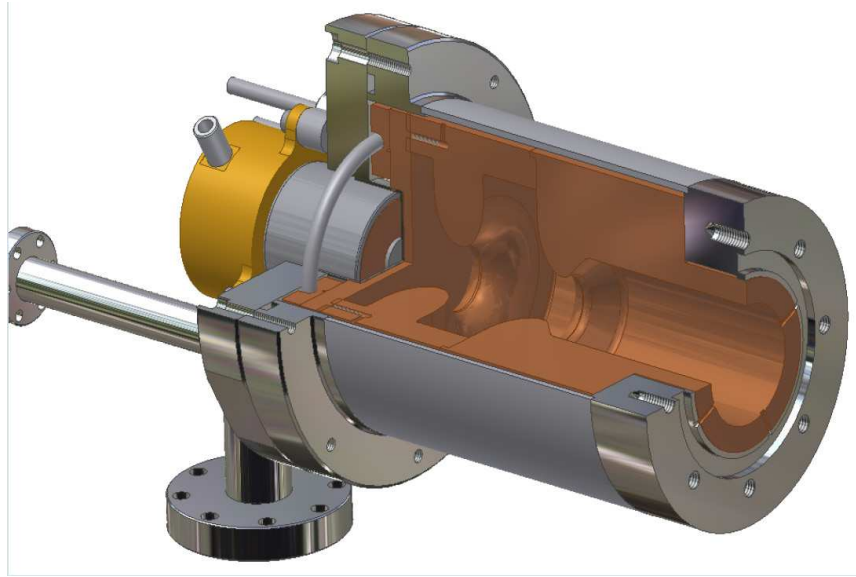


Figure 1.8: A representation of an RF gun with a 1.5 cell cavity used at the Eindhoven University of Technology.

After the RF gun, the electrons are subsequently accelerated by more accelerating sections to a final energy of 250 MeV. Typical bunch parameters are 1 nC charge, 0.5 ps FWHM bunch length, and transverse emittance $\varepsilon_x = 1.2$ mm mrad, resulting in a brightness $B_{\perp} = 3 \times 10^{12}$ A/(m² sr). That gives this gun the status of state-of-the-art. The brightness is so high because, even though the emission surface is relatively large, the pulse length is very short; therefore the current density is high and the brightness becomes large. More recently an emittance of 0.6 mm mrad has been measured at a charge of 250 pC, or even lower 0.14 mm mrad at a charge of 20 pC [13].

A few important effects limit the current density at the cathode. First, the intensity of the photoemission laser pulse which is applied to the cathode surface is limited by the damage threshold of the cathode material. Second, the maximum amount of charge which can be extracted for a given acceleration field is limited by image charge fields. The

acceleration fields should be at least an order of magnitude stronger than the image charge fields, which tend to pull the electrons back into the cathode. Image charge forces affect mainly longitudinal beam quality. For an RF acceleration field of 100 MV/m, this implies that maximally a few hundreds of pC can be extracted per mm² emission area. Third, space-charge forces during the extraction and the first stage of acceleration of the bunch are comparable in strength to the image charge forces. These strong space-charge forces tend to disrupt the transverse beam quality.

1.3.2 Field-emission sources

Another possibility to produce free electrons is by field emission. Here, the electrons tunnel through the surface energy barrier that is thinned in the presence of a strong electric field of about 10⁹ V/m. These fields can be produced by using, for example, a very sharp tip. Two examples are relevant for the latest developments: needle cathodes [17], with sizes in the μm range, and the extreme case of carbon nanotubes, with nm sizes.

In the experiment reported in [17], a tungsten needle with a radius of about 1 μm and a cone half angle of 15° is used. The extracted current depends very strongly on the applied electric field. At high current densities, space-charge effects become significant. A major disadvantage of this method is that after a few hours of operation, even at low currents, the extracted current becomes erratic and the tip needs additional treatment. A carbon nanotube (CNT) is also based on field emission [3]. It is an extreme case of the needle cathodes because the electrons are emitted from an area with a virtual radius of only 3 nm. An angular current density $dI/d\Omega = 16\mu\text{A}/\text{sr}$ has been measured in [3]. The typical brightness for this source is $B_{\perp} = 2 \times 10^{15} \text{ A}/(\text{m}^2 \text{ sr})$. An even more extreme case is the point field-emission electron source [18], which is an atomic pyramid terminated by a single atom that generates electrons at high rate by field emission. The point source generates electrons at currents in the μA regime. The field emission starts at fields of 2 V/nm, and the resulted kinetic energy is in the order of 50 – 300 eV, depending on the distance between the emitter and the extraction electrode.

In principle, field emitters are used in the continuous regime, but they can also be used as pulsed electron sources. With current technology, a pulsed electric field of such a high amplitude cannot be switched on within 100 fs. Therefore, a hybrid solution has been found. This uses a short laser pulse to hit the tip. Recently it has been shown in [4] that the illumination of a ZrC needle (Fig. 1.9) with short laser pulses (16 ps, 266 nm) while high voltage pulses (60 kV, 2 ns, 30 Hz) are being applied, produces photo-field emitted electron bunches. Up to 150 pC (2.9 A peak current) has been extracted by photo-field emission from this needle. The effective emitting area has an estimated radius below 50 μm, leading to a theoretical emittance below 0.05 mm mrad. This source has therefore a brightness $B_{\perp} = 3 \times 10^{13} \text{ A}/(\text{m}^2 \text{ sr})$.

Arrays of needles, so-called Field Emitters Array Cathodes [19], can be used to obtain higher currents. A nice example is shown in Fig. 1.10. Care should be taken to align the beamlets with respect to each other. If this is not done, the trajectories of neighboring emitters cross each other and the resulting emittance is degraded.

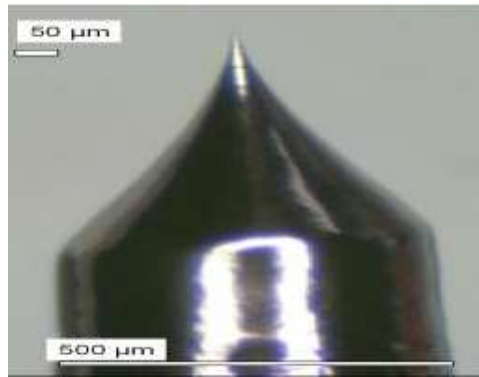


Figure 1.9: Photo of the ZrC needle used in [4].

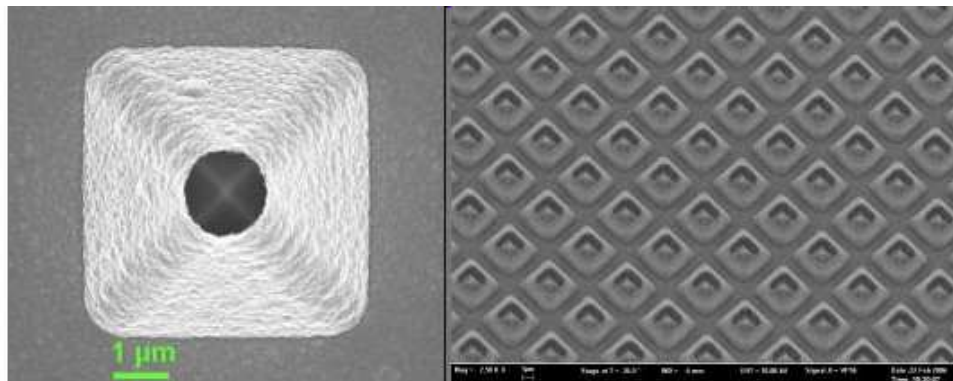


Figure 1.10: Top view of one gated molybdenum pyramid tip (left) and an array of pyramidal tips (right) [19].

In this approach of needle emission surfaces, to obtain a high brightness, the emission area is kept very low so that a high current density can be obtained. A problem with this approach is the large effect that the space-charge forces might have.

1.4 Limitations of the present pulsed electron sources

While the electron sources described in this Chapter have been developed to a high degree of sophistication, they nevertheless give rise to a few limitations, that we have also touched upon. For instance, the XFEL would benefit from a lower emittance, given that the length of the setup could be decreased. Also, a single-shot UED experiment to study biomolecular samples requires a brightness that is higher than what can be achieved at this moment.

Furthermore, space-charge effects play an important role in the quality of the electron beams, in particular with needle sources, where the current density can be very high. With photo-emission sources, shaping of the initial electron distribution to cancel space-charge effects was tried and it starts to be considered as a solution in a few experiments.

The electron sources presented above suffer also from physical damage. Using high power laser pulses, the metal cathode of an RF gun can be damaged to the extent that replacement is required. An advantage of a new source could also be that it would not suffer from these damages.

For all these reasons, an improvement in the quality of pulsed electron sources is desired.

1.5 New approach: cold electron source

As shown above, the usual approach to increase the brightness of the field-emission and photo-emission sources is to increase the current density $\partial I/\partial A$. At very small emission surfaces, however, the effects of the Coulomb repulsion can deteriorate the quality of the source. Therefore, a different path to high brightness that can be followed is to increase the angular intensity $\partial I/\partial\Omega$, for moderate values of the emission area. In the examples presented before, the effective electron temperature of the source T is typically $10^3 - 10^4$ K. If one is able to lower these temperatures at the source, then a gain in brightness proportional to the reduction of the temperature can be achieved for the same current density (see Eq. (1.6) and Eq. (1.10)).

The new source concept based on this idea proposes pulsed extraction of electrons from an ultracold plasma (UCP), which is created from a laser-cooled cloud of neutral atoms by photo-ionization just above threshold [20]. These plasmas are characterized by electron temperatures of 10 K [21], or even lower down to 1 K [22].

A simple estimate serves to illustrate the possible performance of such a source. Laser-cooled atomic clouds can have central densities up to $n = 10^{18} \text{ m}^{-3}$ and contain up to 10^{10} atoms, requiring a cloud with rms size $\sigma = 1$ mm. If all these atoms could be ionized to form a UCP with an electron temperature $T = 10$ K, then an electron bunch with a charge $Q = 1$ nC and an emittance $\varepsilon = 0.04$ mm mrad could be extracted. If, in addition, all of these electrons can be packed into a temporal bunch length on the order of $\sigma_t = 100$ fs, the transverse brightness of the resulting electron bunch would be $B_{\perp} = 6 \times 10^{16} \text{ A}/(\text{m}^2 \text{ sr})$. This is substantially higher than what has been achieved so far in the regime of (sub)-ps electron bunches.

This Thesis presents the potential of the new type of pulsed electron source and the first steps made in practice towards its achievement.

Bibliography

- [1] <http://www.xfel.eu/en/documents/>.
- [2] J.R. Dwyer, C.T. Hebeisen, R. Ernstorfer, M. Harb, V.B. Deyirmenjian, R.E. Jordan, and R.J.D. Miller, *Phil. Trans. R. Soc.* **A364**, 741 (2006).
- [3] N. de Jonge, Y. Lamy, K. Schoots, and T.J. Oosterkamp, *Nature*, **420**, 393 (2002).
- [4] R. Ganter, R. Bakker, C. Gough, S.C. Leemann, M. Paraliiev, M. Pedrozzi, F. Le Pimpec, V. Schlott, L. Rivkin, and A. Wrulich, *Phys. Rev. Lett.* **100**, 064801 (2008).

- [5] R. Akre, D. Dowell, P. Emma, J. Frisch, S. Gilevich, G. Hays, Ph. Hering, R. Iverson, C. Limborg-Deprey, H. Loos, A. Miahnahri, J. Schmerge, J. Turner, J. Welch, W. White, and J. Wu, *Phys. Rev. ST Accel. Beams* **11**, 030703 (2008).
- [6] O.J. Luiten, B.J. Claessens, S.B. van der Geer, M.P. Reijnders, G. Taban, and E.J.D. Vredenburg, *Int. J. Mod. Phys. A* **22**, 3882 (2007).
- [7] R.J.D. Miller, John C. Polanyi Award Lecture, *Can. J. Chem.* **80**, 1 (2002).
- [8] F. Schotte, M. Lim, T.A. Jackson, A.V. Smirnov, J. Soman, J.S. Olson, G.N. Philips, Jr., M. Wulff, and P.A. Anfinrud, *Science* **300**, 1944 (2003).
- [9] B.J. Siwick, J.R. Dwyer, R.E. Jordan, R.J.D. Miller, *Science* **302**, 1382 (2003).
- [10] O.J. Luiten, S.B. van der Geer, M.J. de Loos, F.B. Kiewiet, and M.J. van der Wiel, *Phys. Rev. Lett.* **93**, 094802 (2004).
- [11] P. Musumeci, J.T. Moody, and C.M. Scoby, *Ultramicroscopy* **108**, 1450 (2008).
- [12] T. van Oudheusden, E.F. de Jong, S.B. van der Geer, W.P.E.M. Op 't Root, O.J. Luiten, and B.J. Siwick, *J. Appl. Phys.* **102**, 093501 (2007).
- [13] R. Akre, A. Brachmann, F.-J. Decker, Y. Ding, D. Dowell, P. Emma, J. Frisch, S. Gilevich, G. Hays, Ph. Hering, Z. Huang, R. Iverson, C. Limborg-Deprey, H. Loos, S. Molloy, A. Miahnahri, H.-D. Nuhn, D. Ratner, J. Turner, J. Welch, W. White, and J. Wu, *Phys. Rev. ST Accel. Beams*, Special Edition *Proceedings FEL Conference 2008*.
- [14] S.B. van der Geer, M.J. de Loos, T. van Oudheusden, W.P.E.M. Op 't Root, M.J. van der Wiel, and O.J. Luiten, *Phys. Rev. ST Accel. Beams* **9**, 044203 (2006).
- [15] S.B. van der Geer, M.J. de Loos, E.J.D. Vredenburg, and O.J. Luiten, submitted to *Microscopy and Microanalysis* (2008).
- [16] C.H. Boulware, J.D. Davis, H.L. Andrews, and C.A. Brau, *Int. J. Mod. Phys. A* **22**, 3784 (2007).
- [17] C. Hernandez-Garcia and C.A. Brau, *Nucl. Instr. Meth. Phys. Res. A* **429**, 257 (1999).
- [18] H.-W. Fink, W. Stocker, and H. Schmid, *J. Vac. Sci. Technol.* **B8**, 1323 (1990).
- [19] R. Ganter, R.J. Bakker, R. Betemps, M. Dehler, T. Gerber, J. Gobrecht, C. Gough, M. Johnson, E. Kirk, G. Knopp, F. Le Pimpec, K. Li, M. Paraliiev, M. Pedrozzi, L. Rivkin, H. Sehr, L. Schulz, and A. Wrulich, *J. Vac. Sci. Technol.* **B24**, 974 (2006).
- [20] T.C. Killian, S. Kulin, S.D. Bergeson, L.A. Orozco, C. Orzel, and S.L. Rolston, *Phys. Rev. Lett.* **83**, 4776 (1999).
- [21] J.L. Roberts, C.D. Fertig, M.J. Lim, and S.L. Rolston, *Phys. Rev. Lett.* **92**, 253003 (2004).
- [22] R.S. Fletcher, X.L. Zhang, and S.L. Rolston, *Phys. Rev. Lett.* **99**, 145001 (2007).

Basic principles of an electron source based on ultracold plasma

In Chapter 1, Section 1.5, a new concept for a bright pulsed electron source was proposed, that has the potential of improving the brightness of pulsed sources compared to the state-of-the-art. This chapter presents the basic principles of the new type of source. Also, practical performances of the source are investigated with particle simulations.

2.1 The new electron source based on ultracold plasma

To realize a UCP-based electron source in practice, a four-step procedure is proposed. It is illustrated schematically in Fig. 2.1:

- (I) Atoms are cooled and trapped in a magneto-optical trap (MOT) [1].
- (II) Part of the cold atom cloud is excited to an intermediate state with a quasi-continuous laser pulse.
- (III) A pulsed laser beam propagating at right angles to the excitation laser ionizes the excited atoms only within the volume irradiated by both lasers. Subsequently, a UCP is formed [2].
- (IV) The electrons of the UCP are extracted by an externally applied electric field pulse.

If a cloud of atoms is trapped in a MOT, then up to 10^{10} atoms can be trapped, with a maximum density of about 10^{18} m^{-3} [3]. The next step is to create a UCP [2]. By exciting the atoms to just above the ionization limit with a multi-ns laser pulse, the electrons are created at $T \approx 1 \text{ mK}$. Subsequently, ns-timescale heating processes inside the plasma increase the temperature to $T \approx 1 - 10 \text{ K}$ [4], [5]. The electrons are subsequently extracted by an electric field at least an order of magnitude stronger than what is minimally required for pulling the electrons and ions apart. If rapid switching ($< 1\text{ns}$) of high voltages is possible by using, for example, laser-triggered spark gap technology [6], then a voltage of 1 MV can be applied across a 10 mm gap. The bunches might gain kinetic energies in the order of 1 MeV.

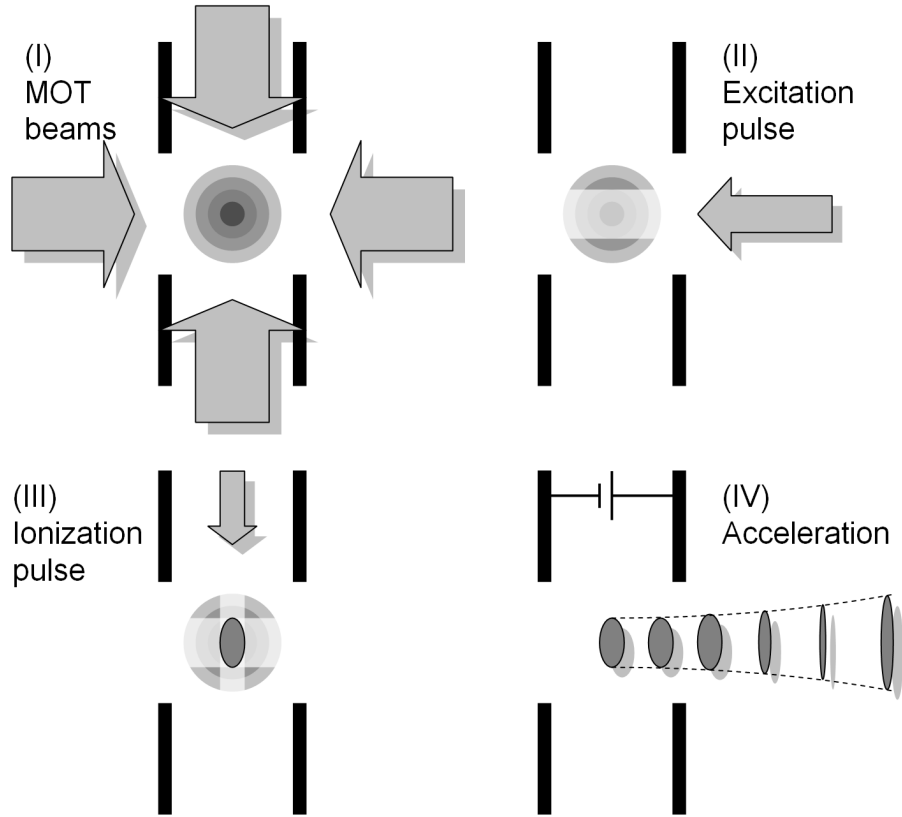


Figure 2.1: Schematic of the four-step procedure to realize a pulsed UCP electron source: (I) atom cooling and trapping; (II) excitation; (III) ionization; (IV) acceleration of the charged particles.

2.2 The steps to produce an ultracold plasma

As explained above, to obtain a UCP, the atoms must be first cooled and trapped, then ionized. Each of these steps is explained in some detail below.

2.2.1 Laser cooling

Consider an atomic beam propagating with longitudinal momentum $m\vec{v}$ from a source and a laser beam with momentum $\hbar\vec{k}$ propagating in the opposite direction (Fig. 2.2). When a two level atom absorbs a photon from the laser beam, it is excited from the ground state $|1\rangle$ to the excited state $|2\rangle$. Each absorbed photon gives the atom a kick in the direction opposite to its motion. When it decays back to the ground state, it spontaneously emits photons in a random direction. Therefore, the momentum kicks of the absorbed photons add up in the direction of the light, while the momentum kicks of the spontaneously emitted photons average to zero. The net effect is that the scattering of many photons gives a force that slows down the atoms. This process is called *laser cooling*. For this system, the cooling

force \vec{F}_{scatt} is given by [1]:

$$\vec{F}_{scatt} = \hbar \vec{k} \frac{\Gamma}{2} \frac{I/I_{sat}}{1 + I/I_{sat} + 4\delta^2/\Gamma^2}, \quad (2.1)$$

where I is the laser intensity, I_{sat} the saturation intensity, Γ the FWHM of the line-width of the atomic transition, and $\delta = \omega - \omega_0 + \vec{k} \cdot \vec{v}$ the detuning from resonance, with ω the laser frequency, ω_0 the atomic resonance frequency, and $\vec{k} \cdot \vec{v}$ the Doppler shift.

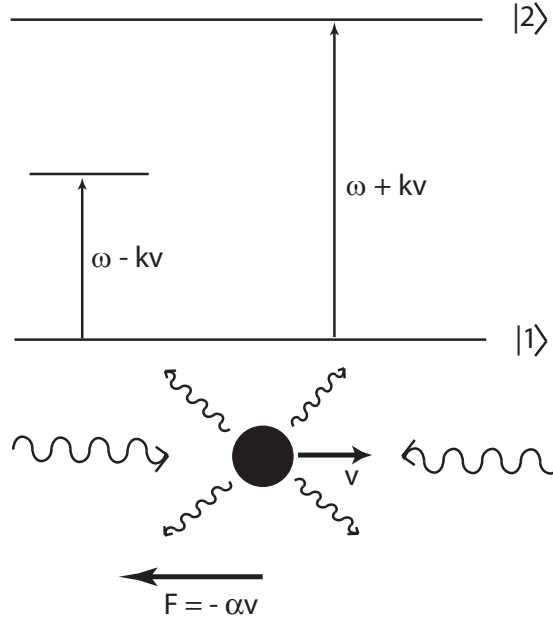


Figure 2.2: For an atom that moves with the velocity v , the Doppler effect leads to a damping in the atomic speed.

If two laser beams propagate in opposite directions, for a moving atom there is an imbalance in the forces caused by the two laser beams due to the Doppler shift. Therefore, they do not properly cancel each other. If the atom moves towards the right, due to the Doppler effect, the frequency of the laser propagating in the opposite direction (to the left) is increased towards resonance, while that from the other direction is just shifted further away from resonance. This subsequently leads to a resulting force F that slows down the atom, which is linearly proportional with the atom velocity v :

$$F = F_{scatt}(\omega - \omega_0 + kv) - F_{scatt}(\omega - \omega_0 - kv) \simeq -2 \frac{\partial F}{\partial \omega} kv. \quad (2.2)$$

The net force therefore results in cooling, i.e., a narrowing of the velocity distribution of the atoms.

Besides this cooling, there is also a heating effect due to the randomness of spontaneously emission, which induces a diffusion in space velocity. The balance between heating

and cooling gives rise to a minimum temperature T_D , called the "Doppler cooling limit":

$$k_B T_D = \frac{\hbar\Gamma}{2}. \quad (2.3)$$

2.2.2 Magneto-optical trapping

In the previously explained configuration, the atoms can diffuse out of the cooling region due to a random walk. An extra restoring force is therefore needed to keep the atoms at a fixed position in space. The force needs to be position dependent. This can be realized by the use of a quadrupole magnetic field generated by a pair of current loops arranged in an anti-Helmholtz configuration, together with a pair of σ^+ and σ^- circularly polarized laser beams. The functioning principle of a MOT is described schematically in Fig. 2.3. It is explained here for an atom with a ground state angular momentum quantum number $J = 0$ and excited state with $J = 1$. In the presence of a static magnetic field, a spectral line is split into several components, due to the so-called Zeeman effect. At the center of a trap, the magnetic field is zero. Out of the center, the Zeeman effect determines a splitting of the energy levels and thus a linear variation with axial position z of the energy of the sub-levels with $J = 1$. For red (negative) detuning of the laser beams, an atom that moves towards the right out of the center is resonant with a circularly polarized laser beam σ^- directed to the left and is sent back to the center. The same happens with an atom that moves towards the left, which is resonant with the σ^+ laser. Transition selection rules say that the σ^- light causes only $\Delta M_J = -1$ transitions, while σ^+ light causes only $\Delta M_J = +1$ transitions. The Zeeman effect thus causes an imbalance in the radiation force, directly proportional to the position z . Therefore, the atoms that enter the region of the laser beams are slowed down and pushed to the trap center by the force F_{MOT} , which both cools and traps the atoms,

$$F_{MOT} = -\alpha v - \kappa z, \quad (2.4)$$

where α and κ are constants that depend on laser intensity and detuning. This combination of velocity and position dependent forces therefore gives the opportunity to load atoms in a MOT and cool them to a temperature close to T_D .

2.2.3 Rubidium atoms

In our experiment, rubidium atoms (^{85}Rb) have been chosen. The optical transitions used for cooling and trapping are represented in Fig. 2.4. Laser cooling and trapping is done between the $5S_{1/2}$ ($J = 1/2$) and $5P_{3/2}$ ($J = 3/2$) levels. The isotopes have a nuclear spin (quantum number I) different from zero (here $I = 5/2$) which interacts with the angular momentum J . Therefore, the S and P states split in a hyperfine structure (characterized by a total spin $\vec{F} = \vec{I} + \vec{J}$). The trapping laser operates between the $5S_{1/2}, F = 3$ and $5P_{3/2}, F = 4$ at a wavelength of 780 nm. Some atoms can also be excited to a unwanted state, $5P_{3/2}, F = 3$, and if they decay to the $5S_{1/2}, F = 2$ level, it is no longer possible to excite them by the trapping laser. Therefore, a repumping laser is used in addition. It

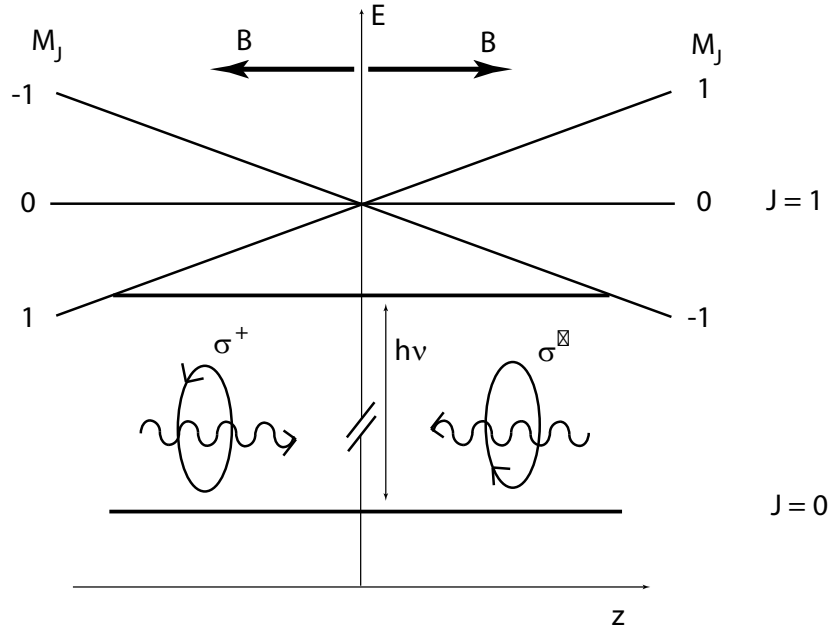


Figure 2.3: Energy level diagram for a $J = 0 \rightarrow J = 1$ transition in the presence of a magnetic field gradient, illustrating the working principle of a MOT. The Zeeman splitting together with the right choice of the laser beam polarizations induce a spatial restoring force.

Table 2.1: Characteristic quantities for the ^{85}Rb atom.

Quantity	Symbol	Value
Wavelength	λ	780.24 nm
Natural linewidth	Γ	5.98 MHz
Saturation intensity	I_{sat}	1.64 mW cm $^{-2}$
Doppler temperature	T_D	142.41 μK

excites the atoms back from the $5S_{1/2}, F = 2$ state to $5P_{3/2}, F = 3$. They can fall back to $5S_{1/2}, F = 3$ and the trapping process can continue. The cooling parameters of ^{85}Rb are listed in Table 2.1.

For cooling and trapping of the rubidium atoms, two commercial diode lasers are used: one is locked to the trapping transition, the other to the repumping transition. The trapping laser is locked using a polarization spectroscopy technique. The repumper is locked using a saturated absorption technique. Precise detuning of the lasers is obtained with the help of an acousto-optical modulator, which is computer-controlled. The laser system is described in detail in [7].

2.2.4 Ultracold plasma formation

The first step in creating a UCP is to cool and trap rubidium atoms, as explained above. With an additional narrow-bandwidth laser pulse, the atoms can be ionized. The difference

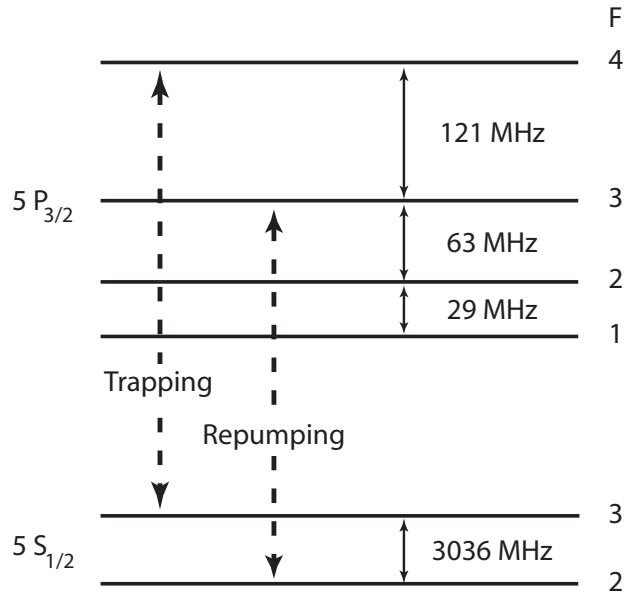


Figure 2.4: Energy levels for the rubidium atoms.

in mass between electrons and ions is very large; therefore the excess energy E_{exc} produced in the ionization process, i.e., the energy above the ionization limit (Fig. 2.5), is mainly carried away by the electrons. The ionization laser wavelength can be very accurately tuned above the ionization threshold, so that the electrons get a very well defined temperature, ranging from milli- to hundreds of kelvin. The ions receive only a small momentum kick and stay in the milli-kelvin regime. An ionized gas can be called a plasma when collective effects are important. To make a distinction, the Debye screening length λ_D is defined as $\lambda_D = \sqrt{\varepsilon_0 k_B T / e^2 n}$, with n the plasma density and T the electron temperature. If λ_D is larger than the size of the system σ , then that system is simply an ionized gas. On the contrary, if $\lambda_D < \sigma$, the gas can be called a plasma. A rough calculation with the parameters of Subsection 2.1 ($T = 10$ K and $n = 10^{18} \text{ m}^{-3}$) show that typical Debye length $\lambda_D = 0.2 \text{ } \mu\text{m}$ is much smaller than the $\sigma = 1 \text{ mm}$ size of the plasma. With these parameters we can talk therefore about a UCP.

The UCPs are formed in a completely disordered state, far from equilibrium. As they equilibrate, the potential energy is converted into kinetic energy and the electrons and ions heat up. This effect is called disorder-induced heating [8] - [11]. The result is that a plasma of 10 mK can be heated up to 10 K on a time scale of a few ns. The electrons can also recombine with atoms and form neutral atoms [12] - [15], which leads to additional heating effects.

An alternative way to create a UCP is to excite the cooled atoms just below the ionization limit and create a cloud of cold Rydberg atoms [16]. The evolution of a gas of excited Rydberg states to a UCP is described in [17]. The idea behind the plasma formation is that ionizing collisions between hot and cold Rydberg atoms and blackbody photoionization produce an essentially stationary cloud of cold ions, which then traps electrons. The

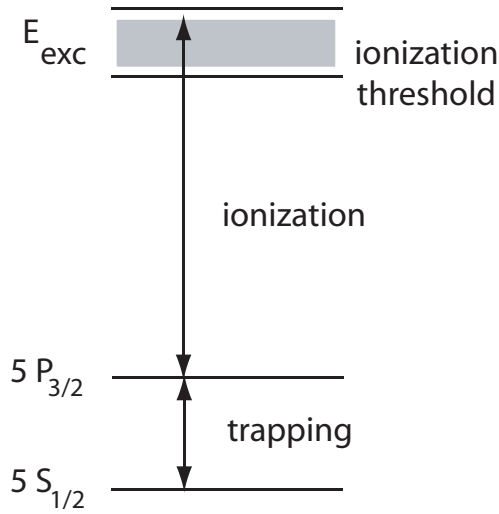


Figure 2.5: Excess energy for the rubidium atoms.

trapped electrons rapidly collisionally ionize the remaining cold Rydberg atoms to form a UCP.

For this project it is very important to know the electron temperature. A method to measure it in a UCP is reported in [4]. A few microseconds after a UCP is created, an electric field is turned on. The electron potential is subsequently lowered by an external electric field and a certain number of electrons escape. Their arrival is measured on a microchannel-plate (MCP) and the signal as function of the electric field gives an indication of the electron temperature. It is found that, as the plasma expands, the temperature becomes lower, thus a cooling process takes place. Heating processes were shown to be important at the early stages of plasma formation. Measured values of electron temperature as function of the plasma evolution time indicated a minimum temperature in the 10 K range.

At later stages of the UCP, i.e., times larger than $30 \mu s$, electron temperatures were extracted from three-body recombination measurements [5]. This process is dominant in plasmas at low electron temperatures. This time, the Rydberg atom production rate as function of the time after plasma creation was measured using two microwave pulses at a few microseconds after each other. From these measurements, electron temperatures as low as 1 K have been calculated, and it was shown that at a very late stage of the plasma, i.e., $200 \mu s$, temperatures of 200 mK can be achieved.

These measurements together show that UCPs form a unique medium with very low electron temperatures.

2.3 Expectations from the cold atom electron source¹

In Section 2.2, the steps that should be taken to realize a UCP-based electron source were explained. The present section tries to investigate what the performance of such a source might be in practice. For this investigation, simulations with the General Particle Tracer (GPT) code [18] are performed and the best specifications of the source that can be achieved are discussed.

We imagine an experiment where the starting point is a MOT containing rubidium atoms in a spherically symmetric, gaussian density distribution with an rms radius of 1 mm and a density in the center of $1 \times 10^{18} \text{ m}^{-3}$. The fact that the initial electron density is proportional to the product of the intensities of the excitation and the ionization laser beams in the region of overlap, offers an excellent opportunity to control the initial charge distribution. As it has been shown in [19], the detrimental effects of space charge forces may be virtually eliminated by the combination of lowering the dimensionality of the bunch and proper shaping. A highly desirable initial charge distribution, for example, is a *pancake* bunch (bunch length much smaller than radius R) with a *half-circle* radial charge density distribution [19]:

$$\rho(r) \propto \sqrt{1 - (r/R)^2}. \quad (2.5)$$

Such a distribution automatically evolves into a uniform, ellipsoidal bunch, which is characterized by perfectly linear space charge fields and thus zero space-charge-induced emittance growth. A second useful initial distribution is a *cigar* bunch (radius R much smaller than bunch length) with a *parabolic* longitudinal charge density distribution, which will also evolve into a uniform, ellipsoidal bunch. Using Eq. (1.5), one may show that the normalized rms emittance of such objects is given by:

$$\varepsilon = R \sqrt{\frac{kT}{5mc^2}}. \quad (2.6)$$

Due to the two-step ionization scheme shown in Fig. 2.1 it is possible to create the UCP in either the "half-circle-profile pancake" or the "parabolic-profile cigar" configuration, each with its own specific advantages. As we will show, the pancake bunches are characterized by a high charge, a small energy spread, and robust, stable behavior, while the cigar bunches offer a low emittance and high compressibility. Note that, in spite of the ideal initial distribution, rapid acceleration is necessary, because initially the electron bunch is still subjected to nonlinear forces due to the ion cloud. The time it takes to separate the electrons from the ions should therefore be kept as short as possible.

To create a pancake bunch, a fraction of the atoms is excited with a radial distribution given by Eq. (2.5), with $R = 2 \text{ mm}$. The ionization laser beam then cuts out a longitudinal slice of $15 \text{ } \mu\text{m}$ thickness. Assuming an overall ionization efficiency of 50%, this results in 10 pC charge. To create a cigar bunch, the atoms are excited within a radius of $80 \text{ } \mu\text{m}$ from

¹The results described in this Section are published by B.J. Claessens, S.B. van der Geer, G. Taban, E.J.D. Vredenburg, and O.J. Luiten in Phys. Rev. Lett. **85**, 164801 (2005).

the axis. Subsequently, the ionization laser cuts out a parabolic longitudinal density profile with a total length of 1 mm, resulting in 1 pC of charge. The initial electron temperature of both bunches is set at 10 K.

For the accelerating stage, a cylindrically symmetric field geometry is assumed, in which both the cathode and the anode are thin conducting plates with a circular hole of 5 mm radius, separated by a distance $d = 20$ mm, as it is shown in Fig. 2.6(a). The hole in the cathode enables optical access for both the trapping and excitation laser beams. The electric field is modeled by the product of an electrostatic field due to a voltage $V_0 = 1$ MV across the diode, calculated with SUPERFISH [20], and a linearly increasing time factor t/τ_r , with $\tau_r = 150$ ps. As it was later discovered and shown in [21], a more practical solution to switch very fast a high electric field is a combination between DC and RF technology. Nevertheless, here we restrict ourselves to the switched field.

In Fig. 2.6(a) the acceleration electric field geometry is shown, indicated by equipotential lines, as well as the radial bunch envelope as a function of z . In Fig. 2.6(b) and (c), respectively, the rms normalized emittance ε and the rms bunch length σ_z (in fs) are plotted as a function of z .

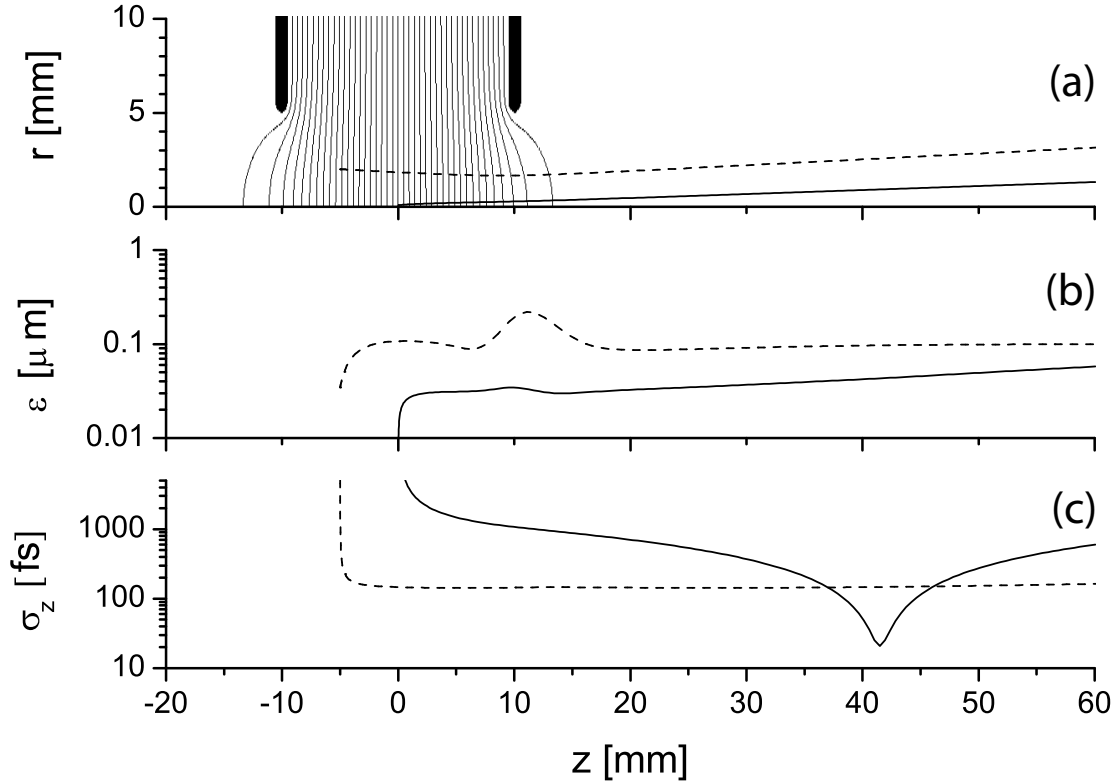


Figure 2.6: (a) Field geometry and radial bunch envelope as a function of z ; (b) rms normalized emittance as a function of z ; (c) rms bunch length as a function of z . Solid lines: cigar bunch; dashed lines: pancake bunch.

The pancake bunch is started upstream at $z = -5$ mm. As a result, the bunch is initially focused by the non-uniform electric field, as can be seen in Fig. 2.6(a), thus partially

compensating for the defocusing "exit kick" of the diode. The final energy of the pancake bunch is 470 keV. The cigar bunch is started at $z = 0$, as its small initial radius does not require any additional focusing. The final energy of the cigar bunch is 270 keV.

As it is shown in Fig. 2.6(b), very low normalized emittances are achieved, of the order of $\varepsilon \approx 0.1 \mu\text{m}$ for the pancake bunch and even lower for the cigar bunch. The behavior of ε as a function of z is similar for both configurations. Initially, $\varepsilon \approx 0.04 \mu\text{m}$ for the pancake bunch and $\varepsilon \approx 0.0015 \mu\text{m}$ for the cigar bunch, in agreement with Eq. (2.6). After initiation, ε first rises sharply due to space-charge forces and then levels off to slow monotonous growth, only briefly interrupted by a temporary rise while passing through the non-uniform field in the hole of the anode.

Fig. 2.6(c) shows that sub-ps bunch lengths can be realized without the use of ultra-fast lasers or magnetic compression. Compression is solely due to velocity bunching, which is particularly efficient for the cigar bunch: at $z = 42$ mm, an rms bunch length $\sigma_z = 20$ fs is achieved, resulting in a peak current $I > 25$ A. The position of the bunch length minimum can be conveniently adjusted over a range of several cm by shifting the initial position by a few mm.

The pancake bunch, on the other hand, almost immediately reaches a respectable bunch length value of $\sigma_z = 150$ fs, corresponding to $I = 25$ A, which is maintained over many cm of its trajectory. This steady behavior reflects a balance between space-charge force repulsion and velocity bunching, which is relatively weak due to the small acceleration potential difference experienced by pancake bunches.

The combination of very low emittances and very short bunch lengths results in extremely high brightness values: after leaving the diode, the pancake bunch attains a constant value $B_{\perp} = 6 \times 10^{13}$ A/(m² sr). This value is higher than the RF guns performance of 3×10^{12} A/(m² sr) [22]. The cigar bunch performs even better: at the bunch length minimum, $z = 42$ mm, $B_{\perp} \geq 1 \times 10^{14}$ A/(m² sr). The cigar bunch configuration clearly offers the highest peak brightness and the shortest bunch lengths, but only at specific positions and with a relatively large energy spread. The pancake bunch is typically less bright, but exhibits stable behavior.

From these simulations we conclude that UCP-based electron sources have enormous potential for advancing the state-of-the-art in ultra-short electron bunch brightness. This potential gain in brightness is due to the combination of a low initial thermal emittance and a short bunch length that results from velocity bunching.

Before showing what we have done in practice towards this goal, we summarize in Table 2.2 the essential parameters of different types of sources discussed here.

2.4 This Thesis

The work presented in this Thesis shows the first steps that have been realized in practice towards this new concept. Because of the technological complexity of the project, some simplifications were necessary.

First, a new dedicated accelerating structure has been designed. It is presented in

Table 2.2: The characteristics of the present electron sources (experimentally measured), together with the expectations from the ultracold source (calculated or simulated).

Source	Rms size σ_x	Temp. T [K]	Charge Q	Bunch length σ_t	Emittance ϵ [mm mrad]	Brightness B_\perp [A/(m ² sr)]	Ref.
CNT (<i>exp.</i>)	3 nm					2×10^{15}	Sec. 1.3
Needle (<i>exp.</i>)	50 μm		150 pC	20 ps	0.05	3×10^{13}	Sec. 1.3
LCLS (<i>exp.</i>)			1 nC	5 ps	1.2	3×10^{12}	Sec. 1.3
UCP (<i>calc.</i>)	1 mm	10	1 nC	100 fs	0.04	6×10^{16}	Sec. 1.5
Cigar (<i>sim.</i>)		10	1 pC	20 fs	0.07	1×10^{14}	Sec. 2.3
Pancake (<i>sim.</i>)		10	10 pC	150 fs	0.1	6×10^{13}	Sec. 2.3

Chapter 3, and has been published in [23]. It allows a MOT to be operated inside of it. The very short pulsed electric fields that can be used with this structure have been characterized with an electro-optic measurement and with an ion time-of-flight experiment. A power supply specially built for this project produces high voltage pulses up to 30 kV, with a rise time of 30 ns. The design of this pulsed high voltage source new switch is described in detail. The idea of switching 1 MV in 100 ps proved to be very difficult at this moment for a table top setup; therefore a more realistic setup has been built. However, the accelerating structure is in principle suited for guiding 1 ns - 1 MV pulses with 100 ps rise time.

Second, in the first experiment with cold atoms, presented in **Chapter 4**, we did not employ a UCP, but the cold atoms were photoionized slightly above the threshold in an already present DC electric field with a maximum field strength of 1.9 kV/cm. We measured the electron temperature of the source and showed that a temperature of 15 K can be achieved. The emittance and subsequently the temperature are deduced from images of the electron pulses created on a phosphor screen, using a model of the beam transport system. A bunch temporal length of 4.7 ns, limited by the ionization laser, has also been measured.

Third, to be able to achieve shorter bunch lengths, field ionization of Rydberg atoms with principal quantum number between 26 and 35 is employed, as explained in **Chapter 5**. Again, electrons with low source temperature of 10 K could be produced. Additionally, the bunch length becomes shorter. We measured an upper limit of 2 ns, but it is believed to be actually much shorter. Cold electron bunches with kinetic energies of a few keV were obtained.

Fourth, the goal of producing high energy beams has been put into practice, as explained in **Chapter 6**. To realize it, an extra charged particle optical element had to be used. The choice was for an Einzel lens. Employing again Rydberg states with principal quantum number between 15 and 25, electron beams with energies up to 14 keV were obtained. However, more work is needed here to measure the source temperature.

Finally, the thesis is rounded up with concluding remarks in **Chapter 7**. An overview of the achievements of this thesis is presented and it is discussed how this new idea of a cold electron source based on ultracold plasmas can be further developed. A few remarks on the

influence of this new concept on other types of charge particle sources are also presented.

Bibliography

- [1] H.J. Metcalf and P. van der Straten, *Laser Cooling and Trapping* (Springer, Berlin, 1999).
- [2] T.C. Killian, S. Kulin, S.D. Bergeson, L.A. Orozco, C. Orzel, and S.L. Rolston, *Phys. Rev. Lett.* **83**, 4776 (1999).
- [3] W. Ketterle, K.B. Davis, M.A. Joffe, A. Martin, and D.E. Pritchard, *Phys. Rev. Lett.* **70**, 2253 (1993).
- [4] J.L. Roberts, C.D. Fertig, M.J. Lim, and S.L. Rolston, *Phys. Rev. Lett.* **92**, 253003 (2004).
- [5] R.S. Fletcher, X.L. Zhang, and S.L. Rolston, *Phys. Rev. Lett.* **99**, 145001 (2007).
- [6] G.J.H. Brussaard and D. Vyuga, *IEEE Trans. Plasma Sci.*, **32**, 1993 (2004).
- [7] B.J. Claessens, PhD Thesis (Eindhoven University of Technology, The Netherlands, 2006).
- [8] M.S. Murillo, *Phys. Rev. Lett.* **87**, 115003 (2001).
- [9] S.G. Kuzmin, T.M. O'Neil, *Phys. Plasmas* **9**, 3743 (2002).
- [10] C.E. Simien, Y.C. Chen, P. Gupta, S. Laha, Y.N. Martinez, P.G. Mickelson, S.B. Nagel, and T.C. Killian, *Phys. Rev. Lett.* **92**, 143001 (2004).
- [11] E.A. Cummings, J.E. Daily, D.S. Durfee, and S.D. Bergeson, *Phys. Rev. Lett.* **95**, 235001 (2005).
- [12] S. Kulin, T.C. Killian, S.D. Bergeson, and S.L. Rolston, *Phys. Rev. Lett.* **85**, 318 (2000).
- [13] T.C. Killian, M.J. Lim, S. Kulin, R. Dumke, S.D. Bergeson, and S.L. Rolston, *Phys. Rev. Lett.* **86**, 3759 (2001).
- [14] S. Mazevet, L.A. Collins, and J.D. Kress, *Phys. Rev. Lett.* **88**, 055001 (2002).
- [15] F. Robicheaux and J.D. Hanson, *Phys. Plasmas* **10**, 2217 (2003).
- [16] T.F. Gallagher, *Rydberg atoms* (Cambridge University Press, 1994).
- [17] M.P. Robinson, B. Laburthe Tolra, M.W. Noel, T.F. Gallagher, and P. Pillet, *Phys. Rev. Lett.* **85**, 4466 (2000).
- [18] <http://www.pulsar.nl/gpt>.
- [19] O.J. Luiten, S.B. van der Geer, M.J. de Loos, F.B. Kiewiet, and M.J. van der Wiel, *Phys. Rev. Lett.* **93**, 094802 (2004).
- [20] J.H. Billen and L.M. Young, POISSON SUPERFISH, Los Alamos Nat. Lab. Rep. LA-UR-96-1834.
- [21] S.B. van der Geer, M.J. de Loos, E.J.D. Vredembregt, and O.J. Luiten, submitted to *Microscopy and Microanalysis* (2008).
- [22] R. Akre, D. Dowell, P. Emma, J. Frisch, S. Gilevich, G. Hays, Ph. Hering, R. Iverson, C. Limborg-Deprey, H. Loos, A. Miahnahri, J. Schmerge, J. Turner, J. Welch, W. White, and J. Wu, *Phys. Rev. ST Accel. Beams* **11**, 030703 (2008).

- [23] G. Taban, M.P. Reijnders, S.C. Bell, S.B. van der Geer, O.J. Luiten, and E.J.D. Vredenburg, *Phys. Rev. ST Accel. Beams* **11**, 050102 (2008).

3

Design and validation of an accelerator for an ultracold electron source²

Abstract.

We describe here a specially designed accelerator structure and a pulsed power supply that are essential parts of a high brightness cold atoms-based electron source. The accelerator structure allows a magneto-optical atom trap to be operated inside of it, and also transmits sub-nanosecond electric field pulses. The power supply produces high voltage pulses up to 30 kV, with a rise time of up to 30 ns. The resulting electric field inside the structure is characterized with an electro-optic measurement and with an ion time-of-flight experiment. Simulations predict that 100 fC electron bunches, generated from trapped atoms inside the structure, reach an emittance of 0.04 mm mrad and a bunch length of 80 ps.

²The work described in this Chapter is published by G. Taban, M.P. Reijnders, S.C. Bell, S.B. van der Geer, O.J. Luiten, and E.J.D. Vredenburg in *Phys. Rev. ST Accel. Beams* **11**, 050102 (2008).

3.1 Bright electron sources and their applications

Pulsed high brightness electron sources are used, for example, in measuring the temperature of surfaces after interaction with ultra-fast lasers [1], in observing transient structure in femtosecond chemistry [2], or in realizing high brightness X-ray sources [3]. The brightest pulsed electron sources are based on the photoemission process to produce electron bunches that are subsequently accelerated in strong electric fields [4].

A way to improve beam brightness is to reduce the source size, because the brightness is proportional to the beam current I divided by the surface area of the beam cross section ΔA , and the solid angle $\Delta\Omega$ associated with the uncorrelated angular spread,

$$B \sim \frac{I}{\Delta A \Delta\Omega}. \quad (3.1)$$

One example of this approach is an electron source based on Carbon Nanotubes (CNT) field-emitters [5]. They are actually the brightest electron sources available at the moment. Here, the electrons are emitted from a sub-micron surface and are able to produce a current of up to $1\mu\text{A}$. Some applications, as for example ultrafast electron diffraction [6], X-ray free-electron lasers [7], or X-ray production by Compton scattering [8], can also benefit from higher brightness, but require much larger currents than CNTs can provide. In fact, the required currents can only be produced in pulsed mode. For these cases, an alternative route to increasing brightness was proposed [9].

Brightness depends inversely on the square of beam emittance, which in turn depends on the square-root of the source temperature T ,

$$B \propto \frac{I}{\varepsilon^2} \propto \frac{I}{T \cdot \Delta A}, \quad (3.2)$$

where

$$\varepsilon = \frac{1}{mc} \sqrt{\langle x^2 \rangle \langle p_x^2 \rangle - \langle xp_x \rangle^2} \quad (3.3)$$

is the so called root-mean-square (rms) normalized emittance [4]. Here, m is the electron mass, c the speed of light, x the transverse position, p_x the transverse momentum, and $\langle \dots \rangle$ indicates averaging over the entire distribution.

Therefore, if we are able to produce electron bunches with a low initial temperature, emittance will also be low and the brightness high, without having to reduce the source size. In this way, pulsed operation with high peak currents and low emittance can be achieved. Our approach to improve the present brightness of pulsed electron beams is based on this idea of a low temperature source [9]. Here, laser-cooled atoms [10] are ionized just above threshold and an ultra-cold plasma (UCP) is created [11]. The electrons of this plasma are initially created with a temperature of approximately 1 mK. Due to the heating process inside the plasma, the electrons quickly equilibrate to a higher temperature in the order of 10 K, which is still orders of magnitude lower than the electron temperature in photoguns [4].

To prevent a space-charge-induced increase in emittance, high electric fields must be turned on with sub-nanosecond rise time to bring a beam as fast as possible to sufficiently

high energies. It has been shown in Claessens *et al.* [9] that the brightness of such an electron beam can be orders of magnitude higher than what exists now in the field of (sub)picosecond pulsed electron sources.

In order to achieve the full potential of this type of source, a specialized accelerator structure is required. It combines an atom trap [12] with the possibility to create fast high voltage fields. To this end, we developed a special diode structure together with a pulsed power supply. This article presents the design of both the accelerating structure and pulsed power supply and shows its value as an accelerator for our cold-atom-based electron source.

It is shown that in this first intermediate setup, ultra-low emittances of 0.04 mm mrad can be achieved in pulsed mode, for bunch charges up to 0.1 pC and 80 ps bunch lengths. The resulting brightness is ~ 130 times lower than that of the LCLS electron source at SLAC [13]. Further improvement of the pulsed high voltage supply, by sharpening the voltage pulse to sub-nanosecond risetimes, should lead to the same emittance, but much shorter pulses of ~ 0.1 ps, resulting in a brightness 10 times higher than the LCLS source. Our final goal is to combine the accelerator presented in this paper with a 1 MV - 0.1 ns rise time voltage power supply, as proposed in [9]. With that, the source can attain a brightness 30 times higher than the LCLS electron source. Using laser-triggered spark gap technology to switch MV voltages, it is possible to generate 1 ns long and 1 MV high pulses with 0.1 ns rise and fall time. As has been shown by several groups, including our own [14], such pulses can be applied across gaps as small as 1 mm without breakdown, for the simple reason that 1 ns is too short for a breakdown to occur. The acceleration structure presented in this paper is suited for guiding such voltage pulses. The setup presented here is a first step towards the realization of the electron source concept presented in [9].

3.2 Accelerator design

A technical drawing of the accelerator is given in Fig. 3.1. It has a coaxial structure. The advantage of using a coaxial geometry is that it can guide very steep field gradients. The designed structure is tapered to reduce reflections of the incoming electric field. The accelerator consists of an inner conductor on which a negative voltage is applied, and an outer conductor which is grounded. A glass ring is used to support the inner conductor of the structure. The structure is designed such as to allow the trapping of a cloud of cold atoms at the center of the accelerating structure, the so-called acceleration point, shown in Fig. 3.1. The design parameters are given in Table 3.1.

The atom trapping process needs six laser beams [10]. A typical size for the diameter of such a laser beam is ~ 10 mm. There are six holes of 20 mm diameter in the outer conductor for the access of these beams. The beams intersect each other in the acceleration point, where the electrons are initially created. One of the laser beams is brought to that point via a mirror placed inside the inner conductor. In addition, there are also holes for the ionizing laser beam and for the electron beam. The inner conductor is connected to a high voltage feedthrough.

In the design process we have maximized the electric field amplitude at the point where

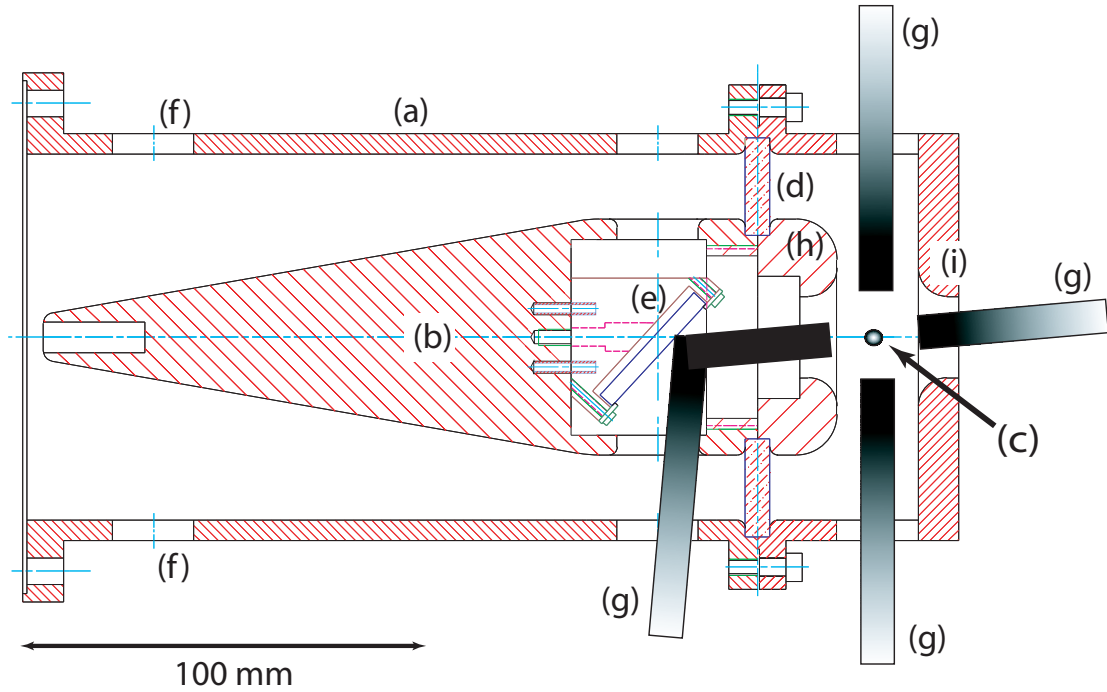


Figure 3.1: Technical drawing of the accelerator (cross-section): (a) outer conductor; (b) inner conductor; (c) acceleration point; (d) glass ring; (e) mirror; (f) pumping holes; (g) laser beams; (h) radius of curvature on the inner conductor R_i ; (i) radius of curvature at the acceleration point R_a .

the electrons will be initially created. This practically means that the distances between the inner and outer conductor are kept as small as possible. At the same time, the fields must be below the breakdown limit in vacuum, which we conservatively assumed to be 100 kV/cm. For that reason, the distance between the inner and outer conductor is 16 mm, the radius of curvature R_i at the end of the inner conductor is 10 mm, and the radius of curvature R_a at the acceleration point is 7 mm.

The accelerating structure was first tested with a DC voltage in order to see if it can sustain the maximum DC voltage that it was designed for, namely 30 kV. The metal surface was conditioned by slowly bringing the inner conductor to the maximum operating voltage.

A cylindrically symmetric field map for this structure, calculated with SUPERFISH [15], is shown in Fig. 3.2. The dimensions of the inner conductor, outer conductor, glass ring and ceramic part of the feedthrough, as listed in Table 3.1, together with their relative permittivity, are used as input. The holes in the outer conductor, which break cylindrical symmetry, are left out. In the figure, the equipotential lines are shown. The electric field strength at the acceleration point is 0.37 kV/cm per kV input voltage. The field map is used for analysis and simulations.

In our first experiments we are going to use typical electric field's rise times of 30 ns. The corresponding wavelength is in the order of meters. This is much larger than the

Table 3.1: Parameters used in the design of the accelerator.

Parameter	Value
Inner conductor maximum outer diameter	58 mm
Inner conductor length	205 mm
Outer conductor inner diameter	90 mm
Outer conductor length	230 mm
Radius of curvature on the inner conductor R_i	10 mm
Radius of curvature at the acceleration point R_a	7 mm
Glass ring outer diameter	98 mm
Glass ring inner diameter	50 mm
Glass ring thickness	6 mm
Glass ring relative permittivity	1.7
Ceramic feedthrough relative permittivity	9

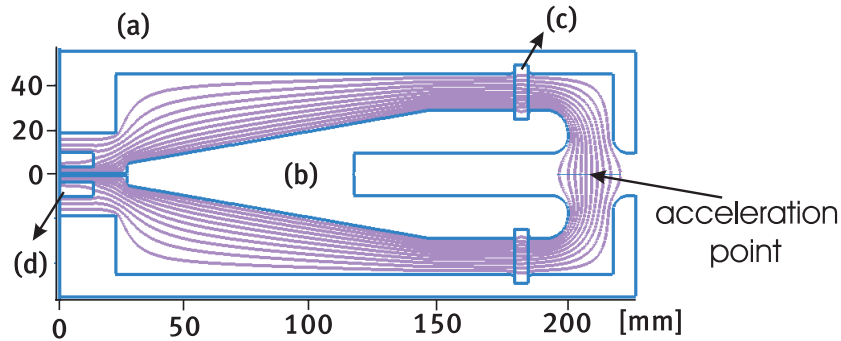


Figure 3.2: Equipotential field lines inside the accelerating structure calculated with SUPERFISH. (a) outer conductor; (b) inner conductor; (c) glass ring; (d) ceramic of the high voltage feedthrough.

dimensions of the accelerating structure. Therefore, the electric field rises uniformly in the entire structure, not causing reflections. Subsequently, the static map can also be used for a pulsed situation.

The same accelerating structure can be used with even shorter rise time, in the order of 150 ps, which we plan to employ in the future. The wavelength corresponding to sub-nanosecond rise time becomes comparable with the structure dimensions. In this case, the field can be diminished in amplitude before it reaches the acceleration point due to reflections associated with impedance mismatch. By tapering the inner conductor, the impedance mismatch, and therefore reflections, are minimized.

To check that the combination of the high voltage feedthrough and the accelerator also works at high frequencies, a Hewlett Packard 8753C network analyzer was used. The amplitude and phase of the electric field reflected by the setup were measured as function of the electromagnetic waves frequency. The frequency interval used in this experiment

was between 300 kHz and 1 GHz, corresponding to a rise time between $1.2 \mu\text{s}$ and 350 ps, respectively. The amplitude of the reflected signal was found to be constant within 0.6 dB over this range. A near-linear dependence of the phase lag versus frequency is observed in the 200 - 900 MHz range (Fig.3.3), corresponding to a reflection of the wave at a fixed point located at 0.70 ± 0.02 m beyond the point where the network analyzer is connected to the accelerating structure. This is the effective distance that a pulse has to travel from the input on the feedthrough up to the acceleration point, namely firstly through the 0.1 m long feedthrough from a ceramic with $\epsilon_r = 9$, secondly through a 0.2 m long connection pipe, and thirdly through the 0.2 m long acceleration. We conclude that up to 350 ps rise time there is no significant distortion of an input high voltage signal.

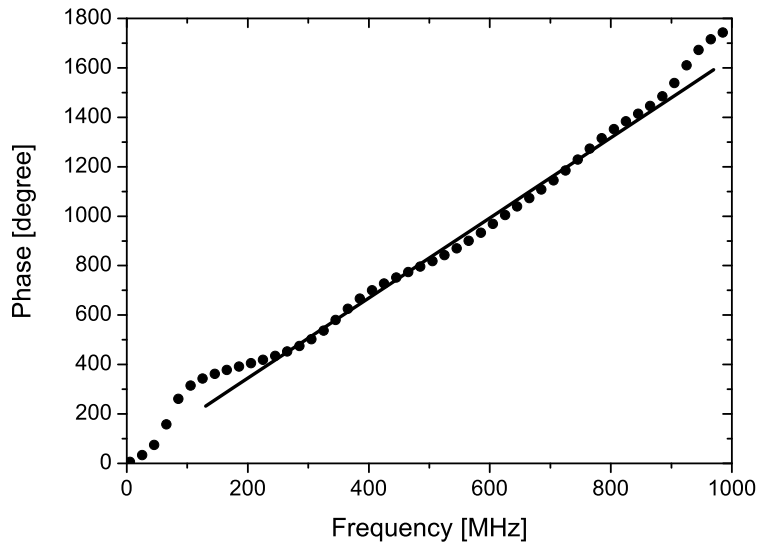


Figure 3.3: Phase shift of the reflected signal as given by a network analyzer.

We have also analyzed the pulse propagation with the 3D time domain solver CST-Microwave Studio (MWS). An illustration of the process can be seen in Fig. 3.4. Here, the pulse is shown at three different moments in time: as the pulse enters the structure (a), halfway the structure (b), and as it reaches the acceleration point (c). In this simulation, the access holes in the outer conductor are also included. For 150 ps rise time, we find an electric field strength at the accelerator point of 34 kV/cm per kV input voltage, i.e., 8% decrease compared to SUPERFISH calculations. The rise time behavior at the accelerator entrance and acceleration point was also monitored in the MWS simulations, as shown in Fig. 3.5. It can be seen from Fig. 3.5 that the 150 ps rise time of an input pulse remains the same at the acceleration point. The accelerator structure is therefore very well suited for sub-ns risetime voltage pulses.

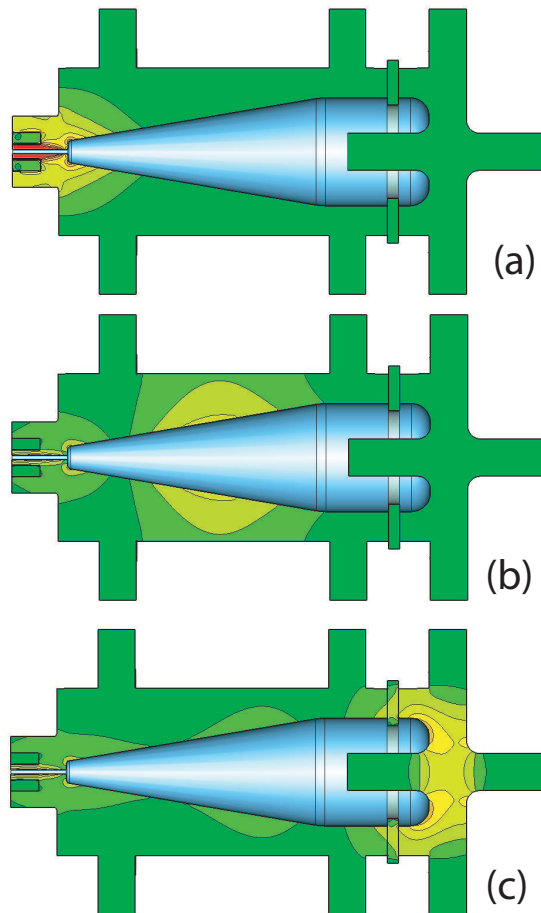


Figure 3.4: CST-Microwave Studio simulation for a pulse with a rise time of 150 ps. (a) the pulse at the entrance; (b) the pulse half way the accelerator; (c) the pulse reaches the acceleration point. In these pictures the vacuum is visualized. The electric field strength is indicated by colors. Red is the maximum electric field strength and green minimum.

3.3 Fast high voltage generation

As it has been stated in our proposal [9], to produce bright electron bunches, a high electric field should be turned on very fast. The proposed source works at a voltage of 1 MV switched on in 150 ps, which in principle can be produced with state-of-the-art technology [14]. The required laser-triggered sparkgap technology is however very cumbersome in use and needs further development before it can be applied in practice. In our first experiments we will use commercially available technology to switch 30 kV in tens of nanoseconds. The corresponding fields are high enough to extract bunches up to 1 pC from a UCP, with a very low emittance.

The system used to produce fast and high electric fields consists of two components: a DC high voltage power supply, and a transistor-based switch setup. The high voltage supply unit is a Brandenburg Model 807R. It produces a maximum DC voltage of 30 kV

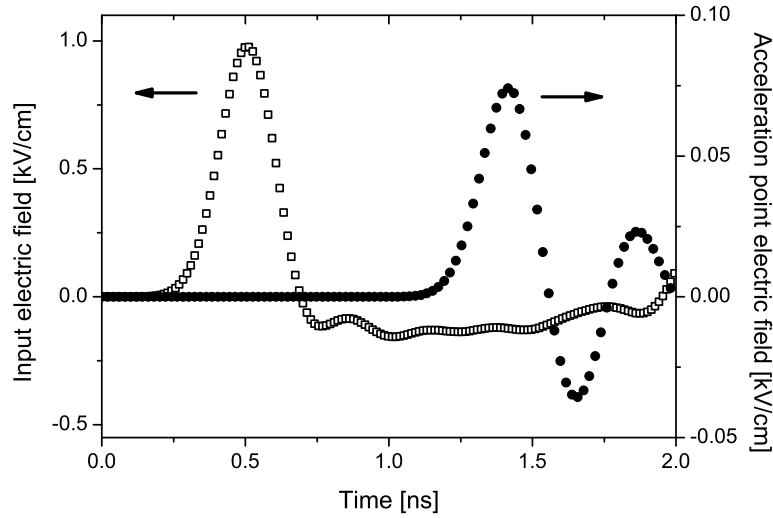


Figure 3.5: CST-Microwave Studio simulation results for a pulse with a rise time of 150 ps. The input electric field is represented by squares \square (left axis) and the electric field at the acceleration point is represented by bullets \bullet (right axis). The maximum electric field at the input was scaled to 1 kV/cm.

and it delivers a maximum current of 1 mA. The DC power supply is connected via a high voltage coaxial cable to the switch box. The power supply feeds the transistor based switch. The fast high voltage transistor switch is a Behlke Model HTS 300. It is a solid state switch used to generate high voltage pulses with a very fast leading edge. The maximum operating voltage is 30 kV, with a peak current of 30 A. The rise time given in the specifications (with a loading capacitance of 20 pF) is 15 ns at a voltage of 24 kV. Pulse duration is 150 ns.

To produce the desired rise time of the voltage, the switch is inserted in a classical pulsed discharge circuit (Fig. 3.6). This means that the energy is collected from a primary energy source (a DC power supply in this case) and is then rapidly released from storage and converted to pulsed form. The output signal goes via a commercial DC ultra-high-vacuum feedthrough (Kurt J. Lesker Co. Ltd. Model EFT 3012093) into the accelerator structure.

The charging resistor R_1 is a 40 M Ω high voltage resistor (Caddock, Type MX485), which limits the current to less than 1 mA. The charging capacitor C_1 is 2 nF. The time constant for the charging circuit is 80 ms. The system can therefore be operated at a repetition rate of a few Hertz. After the switch is closed, the charge accumulated on C_1 is transferred to the accelerator structure, represented by a capacitor C_2 with 12 pF capacitance. Because of the large difference between the buffer capacitor C_1 and C_2 , there is only a small decrease in voltage on C_1 after closing the switch. The resistor R_2 is a 50 Ω current limiting resistor that protects the switch. The time constant for the loading of the

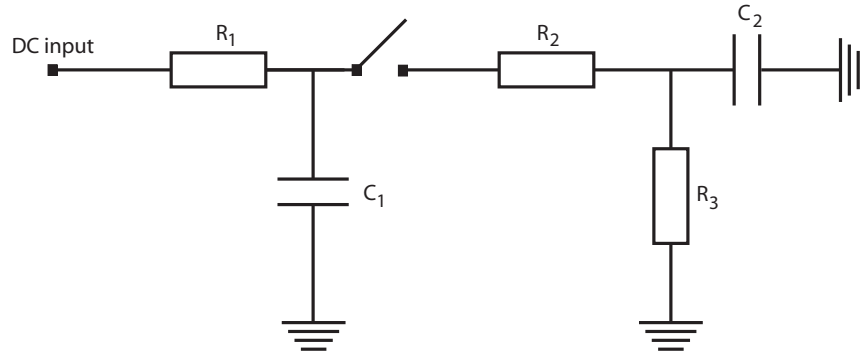


Figure 3.6: Schematics of the transistor based switch used to produce a pulsed high voltage. The values of the components are $R_1 = 40 \text{ M}\Omega$, $R_2 = 50 \text{ }\Omega$, $R_3 = 5 \text{ k}\Omega$, and $C_1 = 2 \text{ nF}$. Capacitor $C_2 = 12 \text{ pF}$ represents the accelerator structure.

accelerator is $R_2 C_2 \approx 0.6 \text{ ns}$, so voltage rise time is determined by the rise time of the transistor switch.

The droop time of this circuit is $R_3 C_1 = 10 \text{ }\mu\text{s}$. After 150 ns, the switch opens again. The influence of droop on the voltage on C_2 during the switch closure time is only 2% of the maximum voltage. At this point the voltage on C_2 will drop and, together with the leakage resistor R_3 of 5 k Ω , it will give a decay time constant of 60 ns.

Using a Tektronix high voltage probe (Model P6015A) with a capacitance of 3 pF, the output signal given by this switch circuit has been measured on the inner wire of the vacuum feedthrough. A typical voltage-time characteristic is shown in Fig. 3.7. The negative high voltage pulse first increases linearly, and is followed by a flat top of 150 ns length, and an exponential decay, in accordance with the design values.

The rise time (defined as 10% – 90% of voltage amplitude) has been measured as a function of the DC voltage (see Fig. 3.8). Above 5 kV, the rise time depends linearly on voltage, with a slope of $(0.70 \pm 0.01) \text{ kV/ns}$. Accordingly, one gets a rise time of 24.5 ns at a voltage of 24 kV, somewhat larger than the specifications of the switch.

3.4 Electric field measurement

This section deals with static and dynamic measurement of electric fields produced in the accelerating structure.

3.4.1 Static electric field measurement with cold ions

A possibility of measuring the static electric field produced at the acceleration point is by using a time-of-flight (TOF) method. A cloud of cold atoms is produced at the acceleration point using the same procedure as described in [16]. The cold atoms are subsequently ionized by a pulsed dye laser with a wavelength of 480 nm and a 6 ns pulse length. The ionization volume has a cylindrical shape with a radius of 70 μm and a height of a few

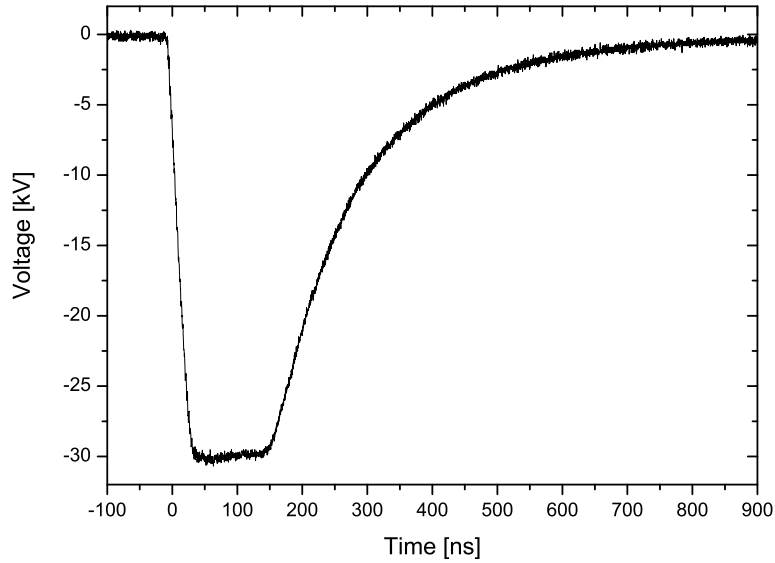


Figure 3.7: Output signal $V(t)$ of the switch measured using a Tektronix P6015A high voltage probe.

millimeters. The orientation of the cylindrical volume is perpendicular to the acceleration direction. A positive DC voltage is applied to the inner conductor of the accelerator. After the ionization, the ions are accelerated towards a microchannel plate (MCP) detector placed at a distance $L = 282$ mm from the acceleration point. With the help of an oscilloscope triggered by the ionization laser pulse, it is possible to measure the TOF τ between the photoionization and the moment that the ions reach the detector.

The TOF measurement can be used to calculate the energy U the ions gain in the accelerator:

$$U = \frac{1}{2}m\left(\frac{L + l_0}{\tau}\right)^2, \quad (3.4)$$

where $l_0 = 14.5$ mm corrects for the fact that the ions are accelerated in the first few millimeters and are not immediately at their maximum velocity. The value of l_0 is determined from simulations. The ionization volume can be precisely moved to different axial positions z , within a few millimeters. The TOF measured in this manner gives a z -dependency. The z -derivative $\frac{1}{q}\frac{dU}{dz}$ of energy is equal to the local electric field.

Fig. 3.9 shows TOF measurements as a function of initial position z . Also shown is the ion energy U as a function of z calculated with Eq. (3.4). The energy $U(z)$ is found to depend approximately linearly on z , which allows us to calculate the electric field at the acceleration point: $E(z = 0) = 0.33 \pm 0.05$ V/cm per V acceleration voltage, in agreement with the value of 0.37 V/cm calculated with the SUPERFISH field map (see Fig. 3.2). From Fig. 3.9 can also be seen that, e.g. at a voltage of 1.36 kV, the measured energy $U(0) = 665$ eV is also, within experimental uncertainty, in agreement with the

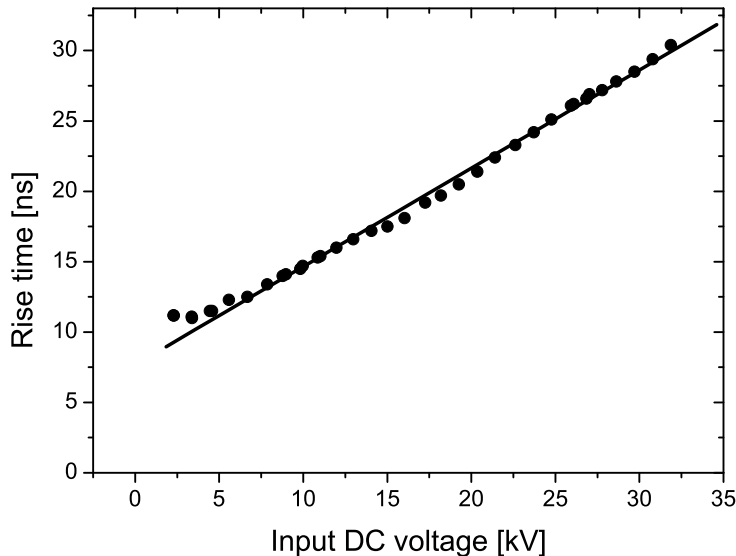


Figure 3.8: High voltage pulse rise time at different input DC voltages.

energy calculated by the electric field integral $\int_0^\infty eE(z)dz = 678$ eV from the SUPERFISH field map.

The main source of uncertainty comes from the determination of the axial position z of the ionization volume. In the setup it is determined by two CCD cameras that image the trapped cold gas in two perpendicular directions. This position accuracy is ± 0.5 mm. We conclude therefore that the local electric field and the beam energy are in agreement within the experimental accuracy of 15% with the calculated design values.

3.4.2 Pulsed electric field measurement with Pockels effect

As explained in Section 3.3, the rise time of the electric field was measured with the help of a high voltage probe at the exit of the switch box. It should also be checked that there is the same rise time at the accelerating point, where the electrons will be created.

To this purpose, an ellipticity measurement method that employs the Pockels effect was used [17]. The method is based on measuring a change in birefringence induced by an electric field.

A lithium niobate crystal ($LiNbO_3$) was used for this purpose. The characteristics of this crystal are given in Table 3.2 [18]. Lithium niobate has been chosen because the saturation time, i.e., the time in which an internal electric field builds up and cancels the external electric field, is much longer than the rise times we want to measure, i.e., in the order of ns. ZnTe crystals, for example, are not suitable for this purpose, but can be used

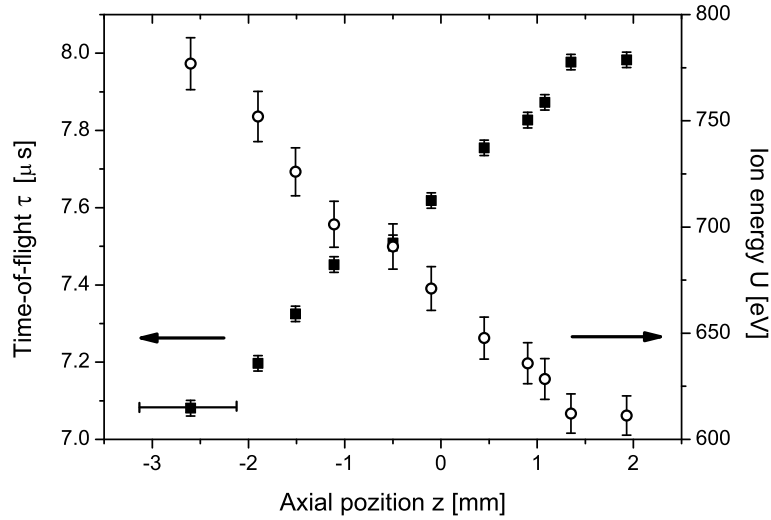


Figure 3.9: Ion time-of-flight ■ (left axis) and energy ○ (right axis) versus axial position at an acceleration voltage of 1.36 kV. The systematic uncertainty in $z \pm 0.5$ mm is represented for a single point (left bottom).

for sub-picosecond rise times when combined with an ultrafast laser [19].

Table 3.2: Characteristics of lithium niobate crystal [18].

Parameter	Value
Size and orientation	5x5x6 mm; z-cut
Electro optic coefficient r_{21}	6.5 pm/V
Refractive index n_0	2.3
Relative permittivity ϵ_r	85

The setup consists of a HeNe laser with a wavelength of 633 nm, a polarizing beam splitter (PBS) cube, a quarter-waveplate (QWP), another PBS cube and two photodiodes (P_1 and P_2) (see Fig. 3.10). The lithium niobate crystal is placed with the help of a small PVC mount between the high voltage electrodes. The first PBS makes the laser beam linearly polarized. After passing the crystal, it passes through the QWP and becomes circularly polarized. It is subsequently divided by the second PBS. Diodes P_1 and P_2 will measure therefore two equal signals when no electric field is present. When a voltage is applied, the electric field induces birefringence and therefore an ellipticity in the laser beam polarization, which results in a difference between the two photodiodes signals:

$$\sin(\Delta\varphi) = \frac{I_1 - I_2}{I_1 + I_2}. \quad (3.5)$$

The phase shift due to the crystal can be written as:

$$\Delta\varphi = \arcsin\left(\frac{2\pi}{\lambda}r_{21}n_0^3Ed\right), \quad (3.6)$$

where λ is the laser wavelength, r_{21} the electro-optical coefficient, n_0 the refractive index, E the internal electric field in the crystal, and d the length that the laser beam travels through in the crystal.

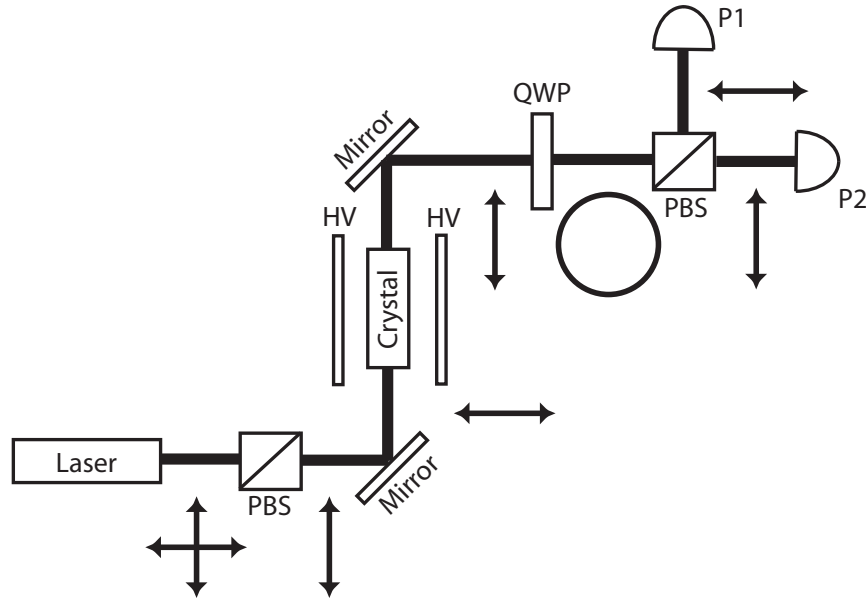


Figure 3.10: Drawing of the optical setup used in the electro-optical measurement. PBS is a polarizing beam splitter cube, QWP is a quarter-waveplate, high voltage electrodes are indicated by HV, and P_1 and P_2 are photodiodes. The light polarization is indicated with arrows and a circle.

A measurement of the electric field with the crystal placed at the acceleration point is shown in Fig. 3.11. Here is also plotted a signal given by the high voltage probe as measured on the inner conductor of the accelerator. It can be seen that the signal on the inner conductor of the accelerator has the same rise time as the signal measured by the lithium niobate crystal at the acceleration point.

In the quasi-static situation, applying a DC external field of 3 kV, a ratio $(I_1 - I_2)/(I_1 + I_2)$ of 0.042 was found. Using Eq. (3.6), this leads to an electric field inside the crystal of 90 V/cm. A calculation of the electric field with the CST-EM Studio simulation program gave 65 V/cm, which is 30% lower. In view of the fact that the electro-optic coefficient r_{21} is not very accurately known and the lithium niobate crystal has a strong influence on the field geometry, this is a satisfactory agreement.

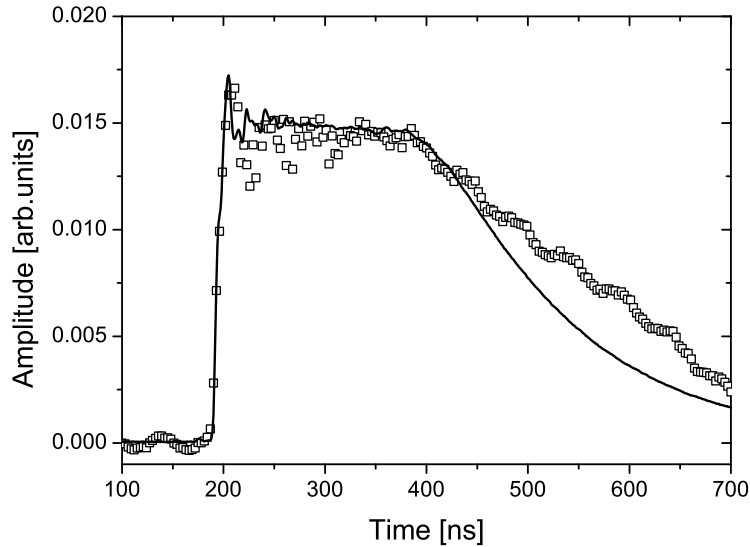


Figure 3.11: Electric field measured with electro-optical technique (\square) and output of high voltage source measured with high voltage probe (continuous line) placed on the inner conductor of the accelerator.

3.5 Valorization of the design

As stated in Sec. 3.2, an electric field map was made in SUPERFISH for the DC case (see Fig. 3.2). By multiplying the electric field of the map with the measured time dependency of the voltage source output (Fig. 3.11), the map can also be used in the pulsed situation. Fields generated in this way were used in the GPT code to simulate the behavior of an electron bunch accelerated in the designed structure. GPT calculates charged particle trajectories in 3D electromagnetic fields, including all space-charge effects [20].

As initial bunch conditions, exactly the same pancake conditions as in Claessens *et al.* [9] were chosen, i.e., a radial distribution of $R = 2$ mm and a thickness of $15 \mu\text{m}$. The simulations have been performed for two different charges, 100 fC and 1 fC. The high voltage slew rate, which is an essential parameter for our simulations, was 0.7 kV/ns (see Sec. 3.3). The rms normalized emittance (see Eq. (3.3)) and the rms bunch length as function of longitudinal position z obtained from these simulations are shown in Fig. 3.12.

It can be seen from Fig. 3.12a that the beam has in both situations a very low rms normalized emittance of 0.039 mm mrad (100 fC) and 0.035 mm mrad (1 fC). These remain constant after leaving the accelerating structure. For 100 fC, the electron bunch is initially compressed to $\approx 20 \text{ ps}$ due to velocity bunching [9](Fig. 3.12b) and then expands linearly in time, reaching a length of 80 ps after 300 mm from the initial point. In case of a smaller charge, 1 fC, the velocity bunching effect brings the bunch to a 0.7 ps length. By applying for example a pulse of 1 MV in 150 ps , a 100 fC bunch can be compressed to

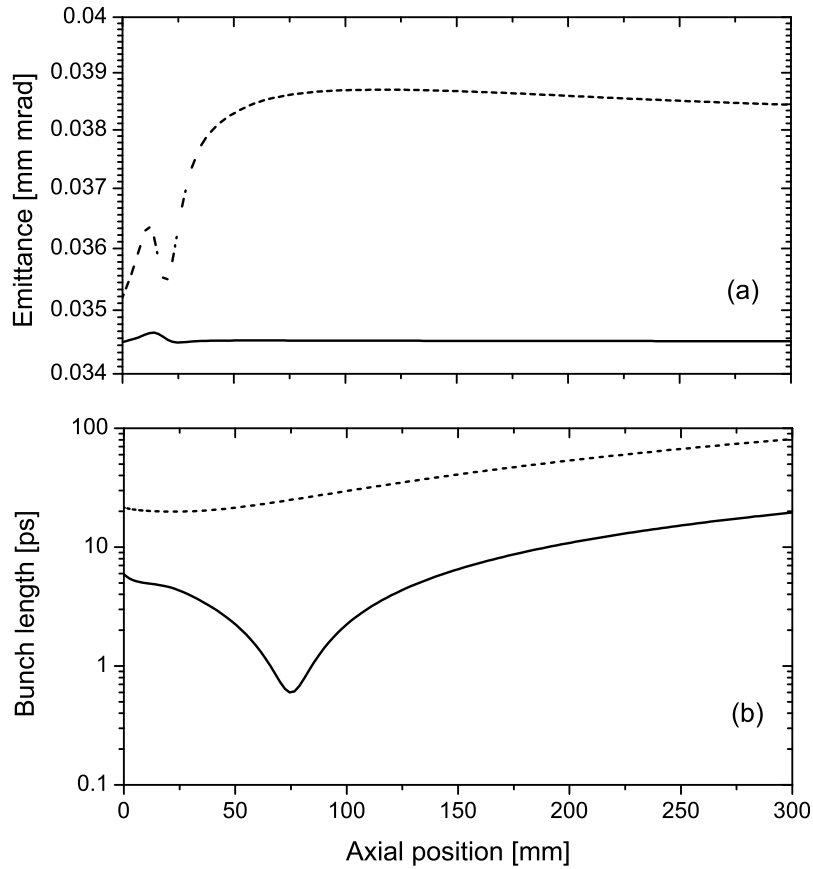


Figure 3.12: GPT simulations using a SUPERFISH field map with a slew rate of 0.7 kV/ns: (a) rms normalized emittance; (b) rms bunch length; both of them as a function of axial position z . The dashed line is for 100 fC and the solid line for 1 fC.

20 fs. Clearly, the amount of bunch compression is limited by space charge forces.

Compared with the LCLS injector at SLAC [13], where electron bunches of 1 nC have been measured with a length of 10 ps and an emittance of 1 mm mrad, our intermediate setup will be able to deliver a 130 times lower brightness. However, our final configuration of 1 MV in 150 ps will be able to deliver a 100 fC bunch with a 30 times higher brightness.

3.6 Conclusions and outlook

A setup specially developed for a new type of pulsed high brightness electron source based on cold atom traps has been described. It consists of a DC power supply, switch setup, and dedicated accelerator. The electric field rise time has been measured with an electro-optical method. The static electric field at the acceleration point and the energy the

accelerated particles gain have also been measured using cold ions TOF measurements. The experimental results and the calculated values agree within the error limits.

Compared with the experiment described in [16], this accelerator has the advantage of being cylindrically symmetric, and provides a higher energy of the electron bunches, making them less sensitive to stray magnetic fields. Simulations show that this setup will be able to produce 100 fC electron bunches with an emittance of 0.04 mm mrad and a bunch length of 80 ps.

For shorter bunch length, an important step is to further reduce the rise time of the electric field. A possible solution is magnetic compression of the high voltage pulse using saturable ferrite cores. In the past, this method produced pulses in the same voltage range with sub-nanosecond rise time [21], [22]. The advantage of a shorter rise time is that the beam energy will be higher. Then, the electrons are less sensitive to space-charge effects and the emittance will therefore be even lower. Also the bunch length will be smaller due to stronger velocity bunching, leading to higher current and thus higher brightness.

A Transmission Line Transformer (TLT) can be used after the sharpener to increase the amplitude of the high voltage. One specially designed broad band TLT will be available in our group in the future [23]. It is capable of multiplying sub-nanosecond high voltage pulses by a factor of 10. In this way, the final goal of 1 MV – 150 ps technology can be reached.

Bibliography

- [1] H.E. Elsayed-Ali and J.W. Herman, *Appl. Phys. Lett.* **57**, 1508 (1990).
- [2] J. Cao, H. Ihee, and A.H. Zewail, *Proc. Natl. Acad. Sci. USA* **96**, 338 (1999).
- [3] R.W. Schoenlein *et al.*, *Science* **274**, 236 (1996).
- [4] For an overview see P. Piot, in *The Physics and Applications of High Brightness Electron Beams* edited by J. Rosenzweig, G. Travish, and L. Serafini (World Scientific, Singapore, 2003), p. 127.
- [5] N. de Jonge, M. Allieux, J.T. Oostveen, K.B.K. Teo, and W.I. Milne, *Phys. Rev. Lett.* **94**, 186807 (2005).
- [6] B.J. Siwick, J.R. Dwyer, R.E. Jordan, and R.J.D. Miller, *Science* **302**, 1382 (2003).
- [7] *TESLA, the superconducting electron-positron linear collider with an integrated X-ray laser laboratory*, DESY technical design report (2001), available from <http://www-hasyllab.desy.de/facility/fel>.
- [8] R.W. Schoenlein *et al.*, *C.R. Acad. Sci. Paris t.2 Serie IV* (2001) 1373.
- [9] B.J. Claessens, S.B. van der Geer, G. Taban, E.J.D. Vredenburg, and O.J. Luiten, *Phys. Rev. Lett.* **85**, 164801 (2005).
- [10] H.J. Metcalf, P. van der Straten, *Laser Cooling and Trapping* (Springer, Berlin, 1999).
- [11] T.C. Killian, S. Kullin, S.D. Bergeson, L.A. Orozco, C. Orzel, and S.L. Rolston, *Phys. Rev. Lett.* **83**, 4776 (1999).

- [12] W. Ketterle, K.B. Davis, M.A. Joffe, A. Martin, and D.E. Pritchard, *Phys. Rev. Lett.* **70**, 2253 (1993).
- [13] A. Cianchi *et al.*, *Phys. Rev. ST-Accel. Beams* **11**, 032801 (2008)
- [14] S. Brussaard and D. Vyuga, *IEEE Trans. Plasma Sci.* **32**, 1993 (2004).
- [15] J.H. Billen and L.M. Young, POISSON SUPERFISH, Los Alamos Nat. Lab. Rep. LA-UR-96-1834.
- [16] B.J. Claessens, S.B. van der Geer, G. Taban, O.J. Luiten, and E.J.D. Vredenburg, *Phys. Plasmas* **14**, 093101 (2007).
- [17] G.E. Jellison, Jr., C.O. Griffiths, and D.E. Holcomb, *Appl. Phys. Lett.* **81**, 1222 (2002).
- [18] A.M. Prokhorov and Y.S. Kuzminov, *Physics and chemistry of crystalline lithium niobate* (Adam Hilger, Bristol and New York, 1990).
- [19] Q. Wu and X.-C. Zhang, *Appl. Phys. Lett.* **71**, 1285 (1997).
- [20] <http://www.pulsar.nl/gpt>.
- [21] J.E. Dolan, H.R. Bolton, and A.J. Shapland, *Electron. Lett.* **33**, 2049 (1997).
- [22] N. Seddon and E. Thornton, *Rev. Sci. Instrum.* **59**, 2497 (1988).
- [23] D.B. Pawelek, P.A.A.F. Wouters, A.J.M. Pemen, A.H. Kemper, and G.J.H. Brussaard, *IEEE Trans. Dielectrics and Electrical Insulation* **14**, 900 (2007).

4

Pulsed photoionization source³

Abstract.

We present measurements of the transverse momentum spread of pulsed electron beams created by near-threshold photoionization of a cloud of ultracold rubidium atoms that is magneto-optically trapped at the center of an accelerator structure. Equivalent transverse electron temperatures ranging from 200 K down to 15 K are demonstrated, easily controllable with the wavelength of the ionization laser. Temperature and emittance are deduced from images of the electron pulses created on a phosphor screen, using a model of the beam transport system.

³The work described in this Chapter will be submitted for publication by G. Taban, B. Fleskens, M.P. Reijnders, E. Sachteleben, O.J. Luiten, and E.J.D. Vredenburgt.

4.1 Introduction

4.1.1 Cold electron sources

In a previous publication [1] we proposed a new type of pulsed electron source based on ultracold plasmas (UCPs), which are formed by photoionization of laser cooled atoms [2] just above the ionization threshold [3]. Such a source could have high brightness because a UCP can store a large amount of electrons (in practice up to 1 nC) with a low kinetic energy spread (characterized by a temperature of a few K) that can be extracted rapidly using a fast electric field pulse. The resulting current pulse would have high angular intensity $\partial I/\partial\Omega$ due to the low source temperature, but moderate current density $\partial I/\partial A$ due to the appreciable source area $A \approx 1 \text{ mm}^2$. The latter reduces detrimental space-charge effects, which play an important role in needle-type sources [4]. In a subsequent proof-of-principle experiment [5], pulsed beams were generated by converting a laser-cooled atom cloud to a highly excited Rydberg gas, which subsequently developed into a UCP, followed by extraction of the electrons with a simple acceleration structure. An upper limit of 500 K for the source temperature was obtained, appreciably lower than the 5,000 K typically found for field-emission and photo-emission sources [6], but substantially higher than the predicted few K, due to the limitations of the experiment.

In the current publication, we present an improved version of such a source, as well as a much improved measurement of the source temperature. The new source consists of a magneto-optical trap for rubidium atoms located inside a recently developed, dedicated accelerator structure [7]. Detailed knowledge of the properties of the accelerator and the magnetic fields associated with the atom trap allow us to derive the source temperature from measurements of the cross section of the electron beam on a downstream detector, using an optical model of the beam transport system. Temperatures down to 15 K are obtained when the wavelength of the pulsed laser that is used to photoionize the trapped atoms is set near the ionization threshold.

In the experiments discussed here, electrons are not produced via the creation of a UCP as reported previously [5], but instead by direct photoionization in a DC electric field so that plasma effects do not come into play. In that sense, the present work is related to the generation of low-energy photo-electrons for the study of electron-atom and electron-molecule collisions [8], [9], [10]. Pioneering work in this field was reported by Kennerly *et al.* [8], who obtained sub-eV electrons with less than 5 meV energy spread (which can be translated into a corresponding source "temperature" of 100 K) by photoionizing barium atoms using a continuous-wave He-Cd laser. The technique was further perfected in the Hotop group, which has used it in many electron-atom and electron-molecule scattering experiments, with the most recent work reported in [11] and references cited therein. Energy spread as low as 20 μeV (0.5 K) has been achieved at sub-meV average energy by carefully reducing the ambient electric fields [10]. Low-energy photo-electrons with 3.5 meV energy spread have also been produced using synchrotron radiation [9].

Our experiments take this work to a different regime, and also demonstrate a different, direct way to assess the source temperature. For one, we concentrate on pulsed operation,

with peak currents that are several orders of magnitude higher than the 100 pA commonly achieved in DC photoelectron sources. Second, our goal is to produce beams with (several) keV average energy, requiring photoionization in electric fields of kV/cm magnitude. This is not the case for the electron collision work referenced above, where one is interested in achieving low energy spread, therefore by photo-ionization in low fields of a few V/cm. Finally, we determine the source temperature by studying the kinetic properties of the electron beam itself, while in the electron scattering work this was inferred from the observed width of scattering resonances.

Our goal is in fact not to produce beams with low energy spread, which is crucial for high resolution scattering studies, but instead to produce beams with high brightness, which is crucial for applications such as ultrafast electron diffraction [12]. Therefore, optimization of the source quality is related to achieving low momentum spread only in the transverse direction. This is expressed by the definition of the transverse brightness B_{\perp} of a source, which is the current density per unit solid angle subtended by the beam, normalized for the beam energy. It is usually expressed in terms of peak current I and source emittance $\varepsilon_{x(y)}$ for the x (y) direction as [13]

$$B_{\perp} = \frac{I}{4\pi^2\varepsilon_x\varepsilon_y}. \quad (4.1)$$

For a thermal source, emittance ε is proportional to the product of the root-mean-square (rms) source size σ_x and the rms momentum spread σ_{p_x} ,

$$\varepsilon_x = \frac{\sigma_x\sigma_{p_x}}{mc} = \sigma_x\sqrt{\frac{k_B T}{mc^2}}, \quad (4.2)$$

where k_B is Boltzmann's constant, T the source temperature, m the electron mass, and c the speed of light.

Here we establish the source temperature by what is in essence a measurement of the transverse emittance of the beam. The minimum electron temperature of 15 K that we observe corresponds to a normalized transverse emittance of 0.0025 mm mrad. The temporal length of the generated electron bunches is limited by the length of the ionization laser pulse and is measured to be 4.7 ns FWHM (full width at half maximum). For a bunch charge of 10 fC, a transverse brightness of $B_{\perp} = 8 \times 10^9$ A/(m² sr) is calculated, which is 3 orders of magnitude higher than we reported previously [5]. Possible further brightness improvements are also discussed.

4.1.2 This experiment: an overview

In the experiment reported here, rubidium atoms are cooled and trapped in a magneto-optical trap (MOT) [2] by an arrangement of six laser beams and a quadrupole magnetic field (Fig. 4.1(a)). A small cylinder of these atoms is photoionized, producing free electrons. Under the influence of a DC electric field (Fig. 4.1(d)), the electrons are extracted using a specially designed accelerator structure [7]. Images of the cylinder-like electron beam are

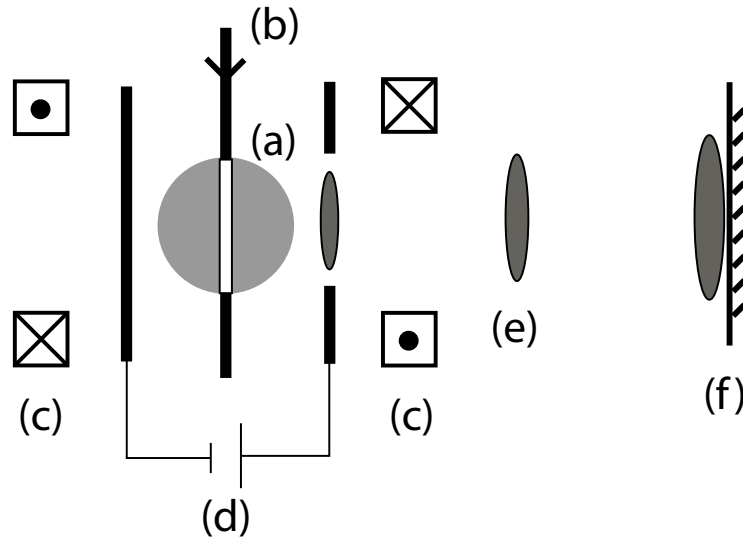


Figure 4.1: A simplified version of the experimental setup used in this experiment (not to scale): (a) cloud of cold atoms; (b) photoionizing laser beam; (c) trapping coils; (d) accelerator electrodes; (e) electron bunches; (f) detector.

obtained on the detector. On the path that they travel to a phosphor screen (Fig. 4.1(f)), they interact with an electromagnetic beam transport system, composed of an electrostatic lens (the accelerator itself) and a magnetic lens (the trapping coils). Due to the magnetic lens, this "optical" system is energy dependent. A dependence between the size of the small axis of the cylinder at the detector and the beam energy can be obtained. With the help of an optical matrix that describes this electromagnetic system, the size of the cylinder is related to the initial electron temperature, which is the parameter that we are actually interested in.

This article is organized as follows: Section 4.2 presents the experimental setup. In Section 4.3 the procedure for measuring the temperature of the electrons is explained. In Section 4.4 the electron source temperature results are presented. Section 4.5 contains a discussion of the implications of these measurements. In Section 4.6 conclusions and an outlook are presented.

4.2 Experimental setup

A schematic overview of the setup used in this experiment is in Fig. 4.2.

4.2.1 Electron production from cold atoms

Cooling and trapping of rubidium atoms. The starting point of the experiment is a classical MOT [2]. Rubidium atoms are cooled down and trapped on the $5s^2S_{1/2}(F = 3) \leftrightarrow 5p^2P_{3/2}(F = 4)$ optical transition in a 3D-vapor-cell MOT (Fig. 4.3). A cloud of

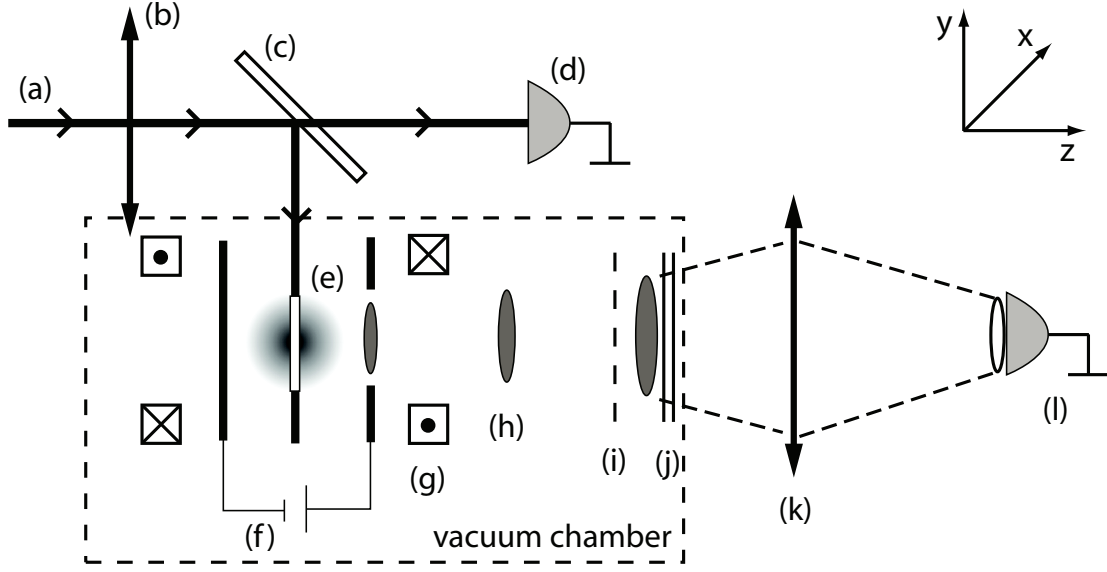


Figure 4.2: The experimental setup used in this experiment (not to scale): (a) photo ionization laser beam; (b) 500 mm lens; (c) partially transparent mirror; (d) CCD camera for monitoring of the ionization laser profile; (e) cloud of cold atoms; (f) accelerator electrodes; (g) trapping coils; (h) electron bunches; (i) grid; (j) MCP + phosphor screen assembly; (k) lens; (l) CCD camera for imaging the electron beam.

about 3×10^7 atoms in a volume with a 3D-Gaussian distribution having a 0.9 mm rms size is created. About 50% of the atoms is in the $5p^2P_{3/2}$ excited state. The magnetic trapping field is produced by two coils in an anti-Helmholtz configuration. Each coil has four windings with a radius of 72 mm made of copper wires that are water cooled. The distance between the centers of the two coils is 66 mm. A current of 190 A flows through the coils. The magnetic field gradient was measured with a Hall probe and has a gradient of $(7.1 \pm 0.2, 7.2 \pm 0.1, 11.6 \pm 0.4)$ G/cm in the x, y, and z directions, respectively. Extra compensation coils are used to set a zero magnetic field at the accelerating point, shown in Fig. 4.4.

Ionization laser. The atoms are ionized by tuning a pulsed dye laser from the $5P_{3/2}$ state slightly above the ionization limit, i.e., $\lambda_0 = 479.06$ nm. Given a wavelength of the ionization laser λ_I , we define the excess energy of the laser E_{exc} , and implicitly an electron temperature T , as

$$E_{exc} = hc \left(\frac{1}{\lambda_0} - \frac{1}{\lambda_I} \right) = \frac{3}{2} k_B T, \quad (4.3)$$

with h the Planck's constant. This excess energy is transformed into kinetic energy of the ions and electrons, and thus essentially into temperature. Most of the energy is transferred to the electrons, because of the large mass ratio between electrons and ions. The amount of excess energy can be controlled by tuning the wavelength of the dye laser. This gives the opportunity to set the initial electron temperature.

The central wavelength of the dye laser using Coumarin dye is 480 nm and can be scanned over a large range with a resolution better than 0.01 nm. The wavelength is

measured using a calibrated LM-007 Lambdameter. The ionization laser beam is focused by a 500 mm focal length lens. It is split into two parts: one ionizes the cloud of cold atoms, the other goes to an additional charged-couple device (CCD) camera (Fig. 4.2(d)) where its profile is measured. A cylindrical ionization beam having a Gaussian profile with a $\sim 50 \mu\text{m}$ rms size is obtained. A typical ionization pulse has a 5 ns length and an energy of $15 \mu\text{J}$. This energy has been chosen because it is small enough to prevent saturation of the ionization process, as well as unwanted space-charge effects. The ionization beam can be positioned in the center of the MOT with 0.5 mm precision.

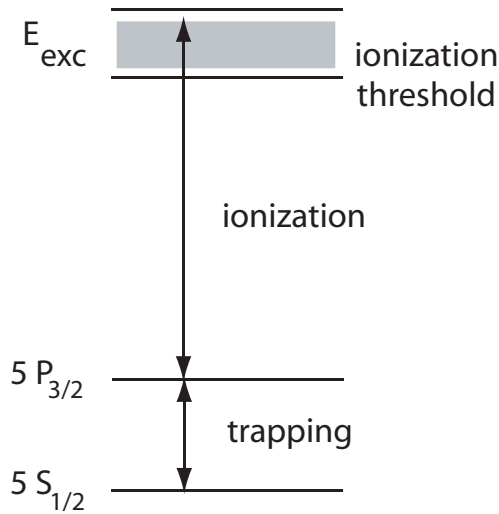


Figure 4.3: Energy diagram for the rubidium levels.

4.2.2 Charged particle beamline

Accelerator. The atomic cloud is created in the center of a specially designed accelerator structure described in detail in [7] (Fig. 4.4). A DC voltage V_{acc} between 0 and 5 kV is applied to the inner conductor. The electric field strength at the acceleration point is $F = 0.33 \pm 0.05 \text{ kV/cm}$ per kV input voltage. Electric fields up to 1.9 kV/cm are thus obtained at the acceleration point. The relation between the electron beam energy U and the voltage placed on the accelerator V_{acc} is

$$U = (0.51 \pm 0.01)eV_{acc}, \quad (4.4)$$

and kinetic energies up to $U = 2.5 \text{ keV}$ can be obtained.

Electric and magnetic lenses. At the moment the electrons are created, they experience an electric field that accelerates them towards the detector. The electron beam is both focused and defocused. Firstly, when leaving the accelerator structure, the beam is defocused. This happens because, for a particle that is not precisely on the central axis, the field lines are not parallel to the acceleration axis, so the particles feel a transverse

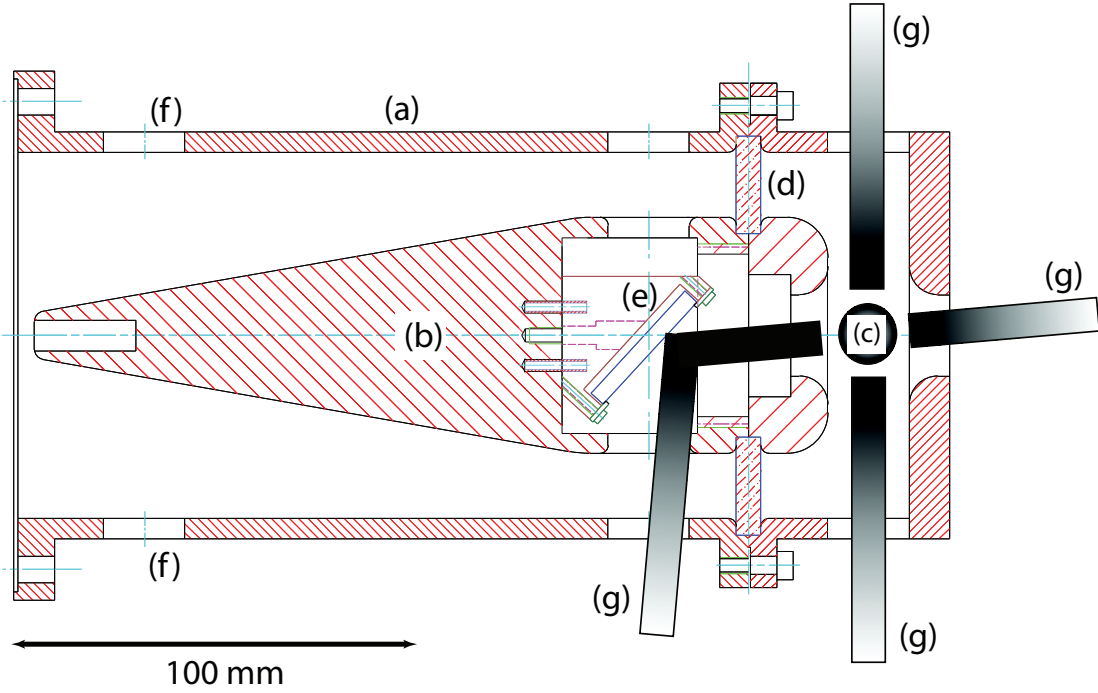


Figure 4.4: Technical drawing of the accelerator (cross section): (a) outer conductor; (b) inner conductor; (c) acceleration point; (d) glass ring; (e) mirror; (f) pumping holes; (g) laser beams.

electric force. The exit hole of the accelerator acts therefore as a negative electrostatic lens with a focal length of 33 mm placed at 9.5 mm in front of the acceleration point. The focal length is independent of the beam energy. Secondly, the magnetic coils act as a focusing lens and also give rise to rotation of the bunch. The focal length of the trapping coils is proportional to the electron energy [14].

The accelerator structure defocuses the beam, while the beam is refocused by the magnetic lens. Depending on the beam energy, the overall action of the two lenses can focus the beam before, precisely on, or after the detector, i.e., the beam is scanned through a waist. A typical picture representing the beam size on the detector as function of beam energy is shown in Fig. 4.5. The curve is not symmetric as expected from an optical system because here not the detector is translated in the longitudinal direction, but the beam kinetic energy is scanned. This behavior is compared with an optical model that describes the system.

Optical description of the system. This system consisting of an electrostatic and a magnetic lens can be described with an "optical" model [15]. Such a model translates the transverse initial position x and velocity v_x of a particle to the final position and velocity via an optical matrix that describes the system. In practice, the transverse velocity v_x is transformed into the divergence $x' \equiv dx/dz = v_x/v_z$ by dividing it by the longitudinal velocity v_z . In the linear approximation, the final particle position x_f and divergence x'_f of each particle as it hits the detector are related to the initial particle position x_i and

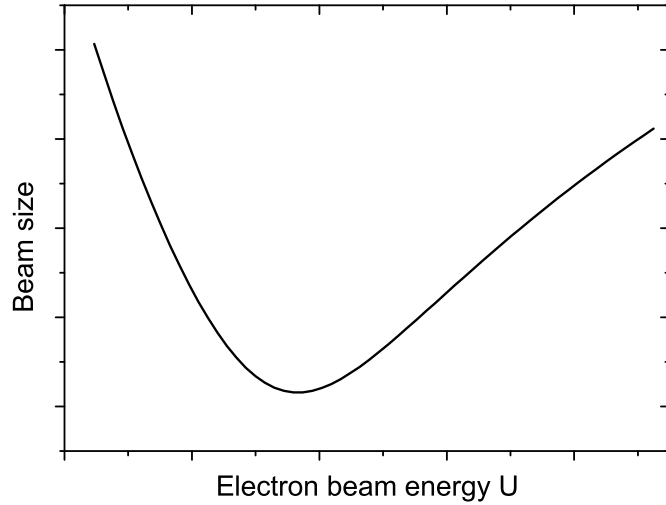


Figure 4.5: Beam size on the detector as function of its longitudinal energy.

divergence x'_i through

$$\begin{pmatrix} x_f \\ x'_f \end{pmatrix} = \begin{pmatrix} A & B \\ C & D \end{pmatrix} \begin{pmatrix} x_i \\ x'_i \end{pmatrix}. \quad (4.5)$$

For our setup, the A and B parameters have been determined using the established computer code General Particle Tracer (GPT) [16], that tracks charged particles in electromagnetic fields. The electrostatic field map of the system was generated with SUPERFISH [17] and imported into GPT. The magnetic lenses are standard elements in GPT. Each of the eight windings is approximated by an infinitely thin circular wire. To determine A, a particle is placed at different transverse positions on the x axis, having a null initial transverse velocity ($x'_i = 0$). The particle position is monitored at the detection plane and, using Eq. (4.5), the ratio of the two positions gives the optical parameter A. To determine the parameter B, a particle is placed at the acceleration point ($x_i = 0$), this time with different transversal velocities. The particle position is monitored at the detection plane and, using Eq. (4.5), the ratio of the final position and transverse initial velocity gives the optical parameter B. Note that both A and B depend on the beam energy. The behavior of the optical matrix coefficients A and B as function of energy U is plotted in Fig. 4.6. It can be seen that A becomes zero at about 1100 eV and B at about 800 eV.

4.2.3 Electron bunches detection

Bunch imaging. An assembly consisting of a microchannel plate (MCP) together with a phosphor screen is placed (Fig. 4.2(j)) at a distance of 282 mm from the acceleration point (Fig. 4.4(c)). The field created at the MCP is screened from the rest of the setup by a

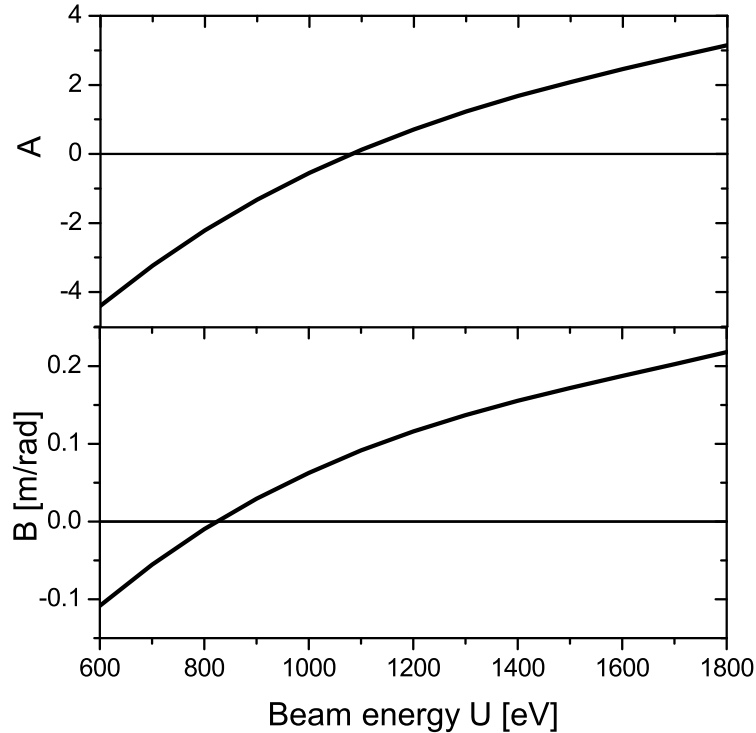


Figure 4.6: The optical coefficients A and B as function of beam energy.

grounded grid placed 22 mm in front of the MCP (Fig. 4.2(i)). The MCP has an effective circular detection area with a 40 mm diameter. To get a sufficient number of electrons that can be imaged on the phosphor screen, the MCP is biased so that the initial number of electrons is strongly amplified (a 1000 V voltage difference between front and back sides is always used in this experiment). The images obtained on the phosphor screen are in turn imaged on a CCD camera (Fig. 4.2(l)). A lens with a 200 mm focal length (Fig. 4.2(k)) is placed at 600 mm from the screen. The CCD camera is 250 mm behind the lens. A magnification of 0.4 is obtained for this imaging system. The imaging system resolution is $21.35 \mu\text{m}/\text{pixel}$, calibrated with the help of the known grid dimensions.

Charge measurement. To measure the bunch charge, the MCP was used as a Faraday cup. With the use of a charge amplifier, we find charges of up to 10 fC that we typically use in this experiment. This is not the smallest detectable amount, since charges of 10 aC can also be measured.

Bunch length. To characterize the brightness of this electron source, we also need to know the temporal bunch length. It has been measured by directly connecting the front of the MCP (used as a Faraday cup) to the input of a 50Ω terminated scope. From the resulting time dependent current, a bunch length of 4.7 ns FWHM is observed (Fig. 4.7,

continuous line). It matches very well the expected value given by the temporal length of the ionization laser pulse. This has been measured separately using a fast photodiode (Fig. 4.7, open circles). If the charge is 10 fC, then the resulting peak current is $2 \mu\text{A}$.

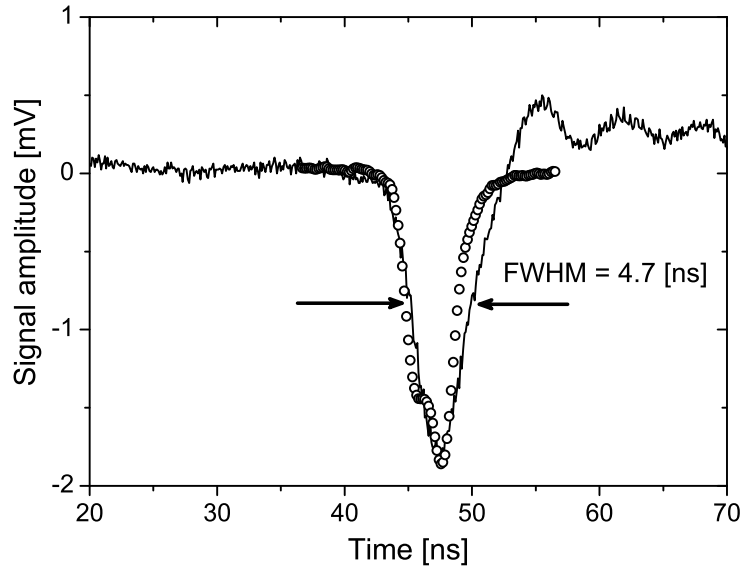


Figure 4.7: Charge arriving on the MCP as a function of time (continuous line). For comparison, a photodiode signal that measures the ionization laser intensity is shown (open circles).

4.3 The experimental method for the source temperature measurement

Here we present the method used to measure the electron beam temperature produced from a cloud of cold atoms. As explained in the previous section, in a typical experiment a cloud of cold rubidium atoms is trapped at the acceleration point. A cylinder-like volume of these atoms is ionized and electrons are created. The electrons are instantaneously accelerated in the static electric field created by the accelerator structure.

The electrons are accelerated towards the MCP, where they are multiplied, and subsequently hit the phosphor screen. Images of these electron bunches are created on the screen and imaged on the CCD. A typical picture of the CCD images is in Fig. 4.8. Indeed, the image on the screen has a cylinder-like shape and is rotated under the influence of the magnetic field, as explained in Subsection 4.2.2.

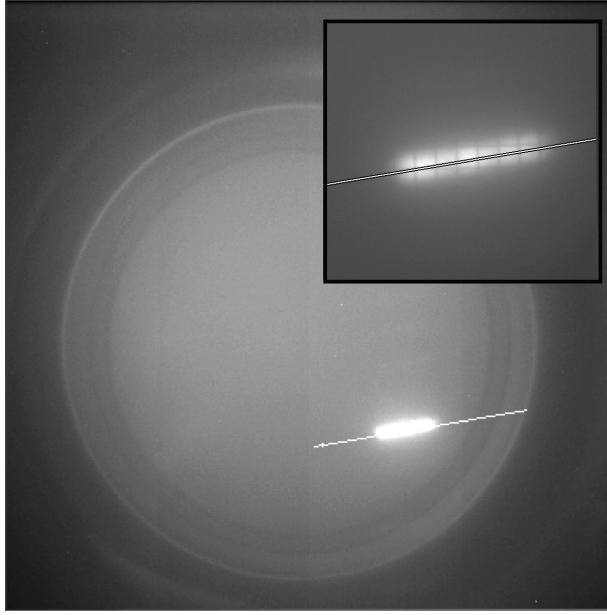


Figure 4.8: A typical CCD image of an electron beam on the phosphor screen. Inserted is a zoom on the electron bunch.

4.3.1 Size dependent measurement

We are interested in measuring the size of the small axis of the cylinder, as observed on the screen. Using the optical model formalism described in the previous section, the rms size of the small axis of the cylinder σ_{x_f} can be calculated as

$$\sigma_{x_f}^2 = A^2\sigma_{x_i}^2 + B^2\sigma_{x'_i}^2. \quad (4.6)$$

The rms size σ_{x_f} depends on the initial rms size of the beam σ_{x_i} and the initial rms divergence of the beam $\sigma_{x'_i}$. A and B are the optical matrix coefficients described in Section 4.2, and

$$\sigma_{x'_i} = \frac{\sigma_{v_x}}{v_z} = \sqrt{\frac{k_B T}{2eU}}. \quad (4.7)$$

Therefore, knowing the beam energy and the initial beam size, the rms size of the small axis in the images on the phosphor can be translated into the initial electron temperature at the source. In the experiment, for a fixed λ_I , i.e., a fixed excess energy, the beam energy is varied by changing the voltage on the accelerator. A scan of the beam size as function of energy as in Fig. 4.5 is obtained. Fitting the experimental points with Eq. (4.6), the initial electron temperature at the source can be found.

4.3.2 Size independent measurement

When $A = 0$, the first term in Eq. (4.6) becomes null and thus the beam size does not depend on the source size σ_{x_i} . According to the model of Fig. 4.6, if one is able to produce

a beam with precisely 1100 eV kinetic energy, then it is possible to measure the source temperature independent on the source size. At this specific energy, by simply scanning the λ_I for a fixed accelerating voltage, the electron temperature can be measured. To experimentally determine this point, different ionization volumes are used and an energy scan around 1100 eV was performed. The point where the different lines are crossing each other is the point where $A = 0$. The result of this experiment is reported in the next section.

4.3.3 Image analysis

The images obtained on the CCD (Fig. 4.8) are analyzed by fitting them with a 2D Gaussian curve (Fig. 4.9). In general, the image intensity is described by a narrow Gaussian peak on top of a lower, also nearly Gaussian background. At this moment this effect is not understood. The background (the dashed line) is subtracted from the total signal (continuous line). The rms size of the difference (dotted line) is used in the reported results.

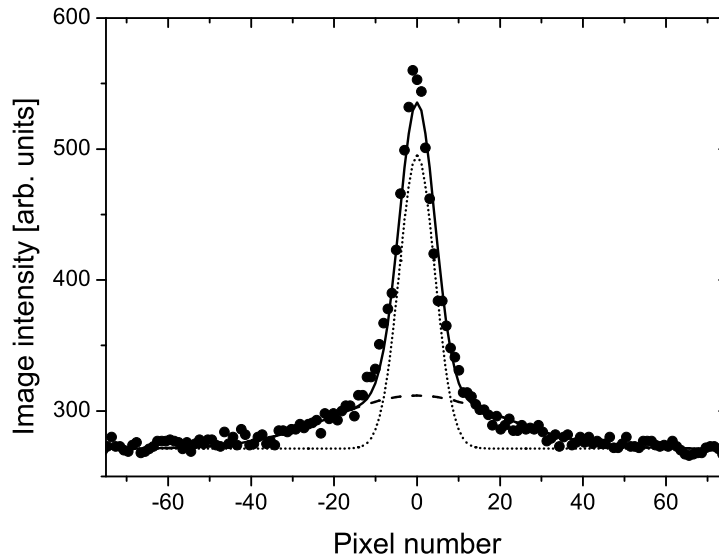


Figure 4.9: Typical Gaussian curve fit of the images on the phosphor screen. The experimental points are represented by circles, the dashed line is the Gaussian background, the dotted line is the actual peak and the continuous line is the total Gaussian fit.

4.4 Experimental results

As explained in Section 4.3, the method used here to determine the electron temperature is to model the final bunch size σ_{x_f} as a function of the electron beam energy U . As

previously explained, the variation of the beam energy is obtained by variation of the voltage on the accelerator. The results for a typical experiment are shown in Fig. 4.10. Every experimental point is the average of at least ten single shot images. By fitting the experimental points with Eq. (4.6), the initial electron temperature can be determined. It can be seen that the fit describes the data quite well, indicating that the beam transport is adequately modeled.

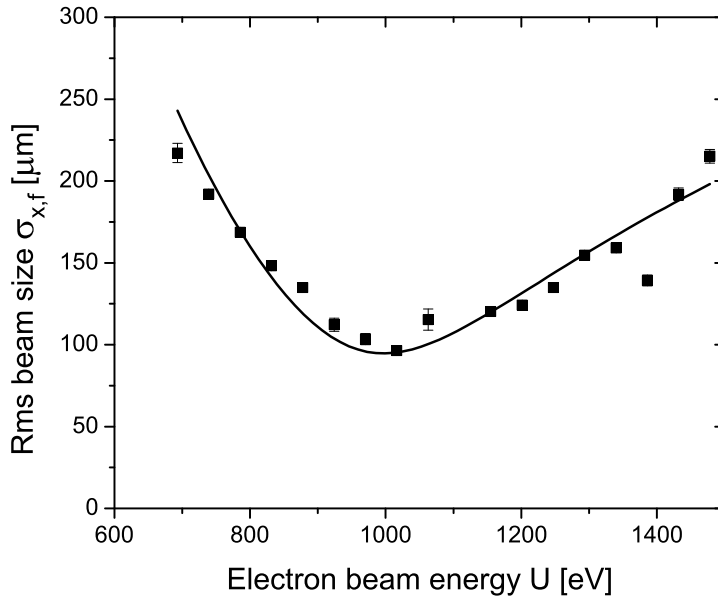


Figure 4.10: Transverse beam size σ_{x_f} as function of electron beam energy U in a typical measurement, here for $\lambda_I = 480.5$ nm. A fit with Eq. (4.6) is represented by the solid line.

The same type of scan was performed for different λ_I . A representation of the rms beam size as function of the kinetic energy U for all λ_I is shown in Fig. 4.11. A simultaneous fit of all data is performed. The rms beam size σ_{x_i} is a constant fit parameter common to all data sets. The beam energy is replaced by αU in Eqs. (4.6) and (4.7), and α is used as an additional fit parameter common to all data sets. This is realistic because, as explained in Subsection 4.2.1, the energy has an uncertainty due to the dependency on the acceleration voltage (Eq. 4.4), and due to the ionization beam position. The electron temperature T is the only fit parameter that is specific for each data set. From the fit, the rms size of the beam σ_{x_i} is found to be $55.9 \pm 0.1 \mu\text{m}$, in good agreement with the ionization beam size as recorded on the additional CCD camera. The scaling factor $\alpha = 0.925 \pm 0.001$ is realistic given the uncertainty in the beam energy U .

The most important result of the fit with Eq. (4.6), the dependence between the electron temperature and ionization laser wavelength λ_I , is plotted in Fig. 4.12. We note that, firstly, a minimum temperature of 15 K is measured at the highest possible λ_I . This temperature is about 30 times lower than the previously reported result [5] and in line with

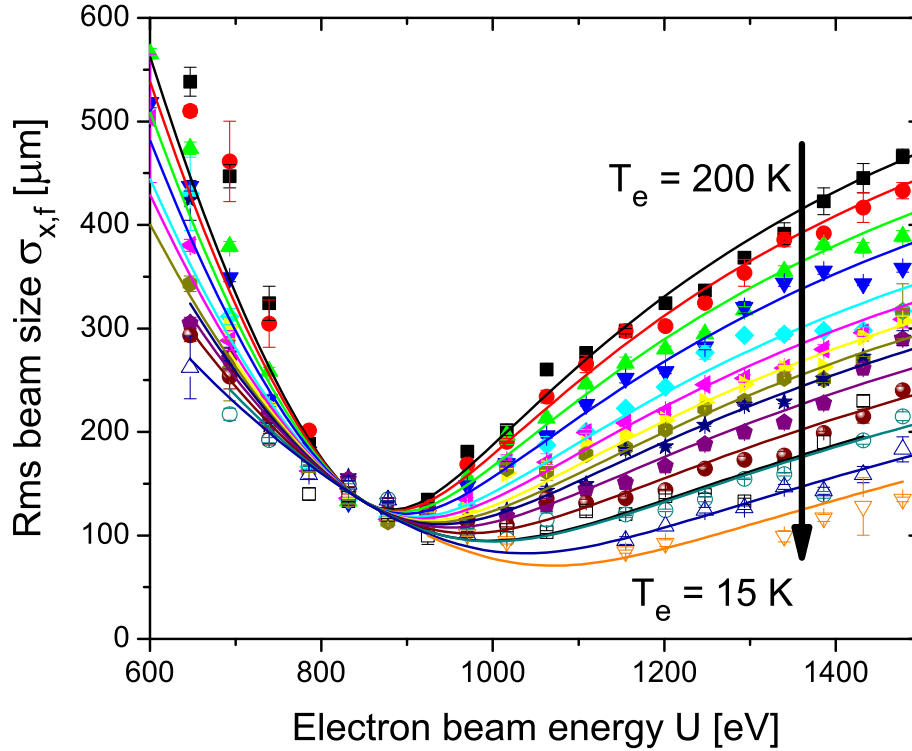


Figure 4.11: Transverse beam size σ_{x_f} as function of electron beam energy U for all experimental wavelengths. A fit with Eq. (4.6) is represented by the solid lines.

the expectations from a UCP source. Secondly, it is important to note that the electron temperature can be easily set on a broad range. Thirdly, the dependence of the electron temperature on λ_I is not precisely as the model of Eq. (4.3) predicts. For temperatures above 50 K, the slope $dT/d\lambda$ of the experimental points does match that of the theoretical line described by Eq. (4.3), but below 50 K the experimental data deviate from this slope. Also an almost constant offset of about 40 K can be seen between the model and the measured temperatures.

Another method of measuring the temperature was described in Subsection 4.3.2. At the point where $A=0$, σ_{x_f} is directly related to the electron temperature. To check at which energy $A=0$ occurs, the beam size was measured as a function of the beam energy for two different sizes of the ionization beam, made by placing the lens (b) from Fig. 4.2 at two different positions. As measured on the CCD camera that monitors the ionization beam, the beam sizes were $\sigma_{x_i} = 30 \mu\text{m}$ and $140 \mu\text{m}$, corresponding to the \blacksquare and \circ points in Fig. 4.13, respectively. The two data sets indeed cross each other around 1100 eV, so again the model matches the expectations.

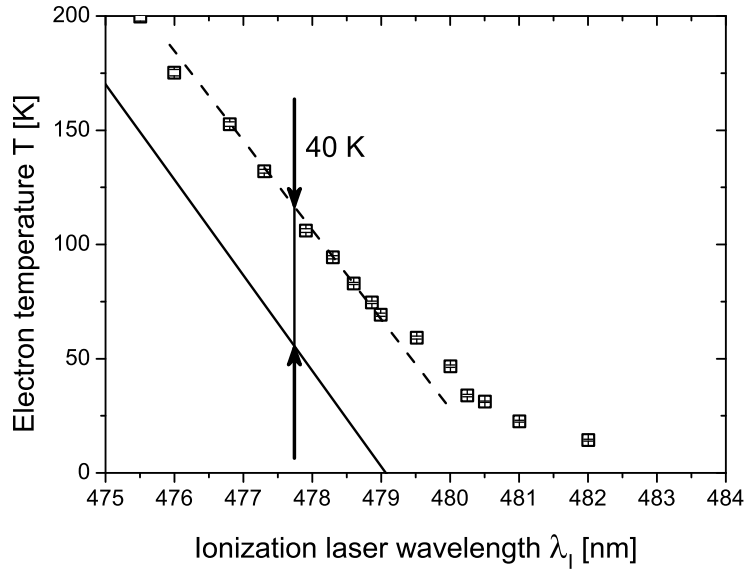


Figure 4.12: The curve fitted electron temperature as function of λ_I . The continuous line is for the model described by Eq. (4.3).

For a fixed beam energy of about 1100 eV, the electron temperature can be measured directly as a function of λ_I by measuring σ_{xf} . Because the crossing of the two data sets of Fig. 4.13 has a certain uncertainty, three different accelerating voltages were used around the expected beam kinetic energy of 1100 eV. The accelerating voltages of 2200 V, 2300 V and 2400 V correspond to beam energies between 1100 and 1300 eV. The measured temperatures are presented in Fig. 4.14, where the squares, the circles, and the triangles represent the three mentioned voltages, respectively. This method is less accurate than the one shown in Fig. 4.12, as evidenced by the scatter of the experimental points. This happens because in the previous experiment of Fig. 4.12 the temperature was measured on a large energy interval, but here it is measured at only one specific energy. However, the data are very similar to the data of Fig. 4.12: for high temperatures the experimental data have the same slope as the theoretical curve, but the points deviate from the linear behavior at lower temperatures. Nevertheless, temperatures under 25 K are obtained consistently for $\lambda_I \gtrsim 481$ nm.

4.5 Discussion

The expectation expressed by Eq. (4.3) is that the electrons will have a zero temperature at the source if $\lambda_I = \lambda_0$, but this is definitely not the case. For wavelengths above λ_0 , contrary to expectations, free electrons are still produced (see Fig. 4.12). Also it can be

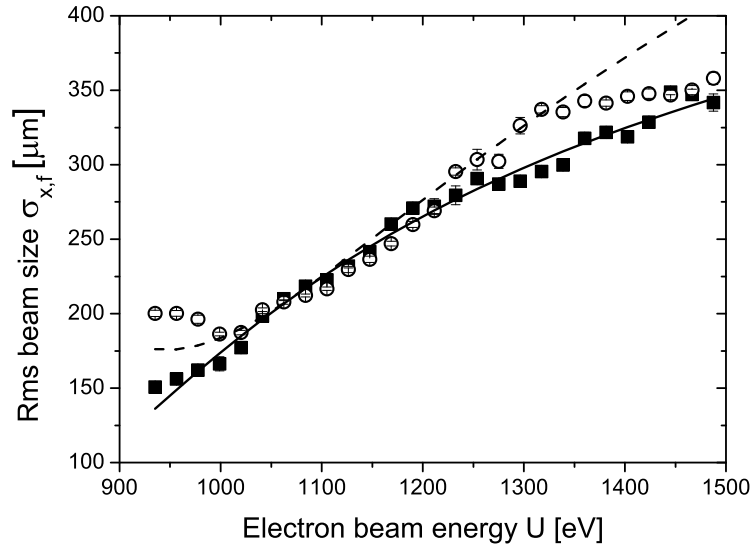


Figure 4.13: Transverse beam size as function of electron beam energy U for an ionization volume of $30 \mu\text{m}$ (full squares ■) and $140 \mu\text{m}$ (open circles ○). The continuous and dashed lines are the corresponding model lines.

seen that the difference in temperature between the experimental points and the classical limit (continuous line) is a constant of about 40 K. These two observations are qualitatively explained by the presence of the accelerating external electric field.

Fig. 4.15 shows the potential of the outer electron of a rubidium atom as function of the distance to the rubidium core in the presence of an external field. Without an external electric field, the potential has the form given by the dashed curve. The outer electron will be ionized when the ionization laser energy $h\nu$ exceeds this classical limit E_0 , as given in the figure. The excess energy E_{exc1} is then given by Eq. (4.3). If it is completely transferred to the electrons and distributed isotropically in all directions, the classical limit can be plotted as the continuous line of Figs. 4.12 and 4.14.

In the presence of an external electric field, the electron potential is influenced and has the form given by the continuous curve in Fig. 4.15. The potential is then tilted by the presence of this external field. In this case, the outer electron will be ionized when the ionization laser energy exceeds the saddle point energy (field lowered limit in Fig. 4.15), which is lower than the previous value E_0 . The excess energy transformed into electron kinetic energy in the field dependent case is therefore E_{exc2} , thus larger than the field free excess energy E_{exc1} .

The ionization energy of an atom in the presence of an electric field is reduced according to [18]:

$$\Delta E_{exc} = E_{exc2} - E_{exc1} = 2\mathcal{H}\sqrt{\frac{F}{F_0}}, \quad (4.8)$$

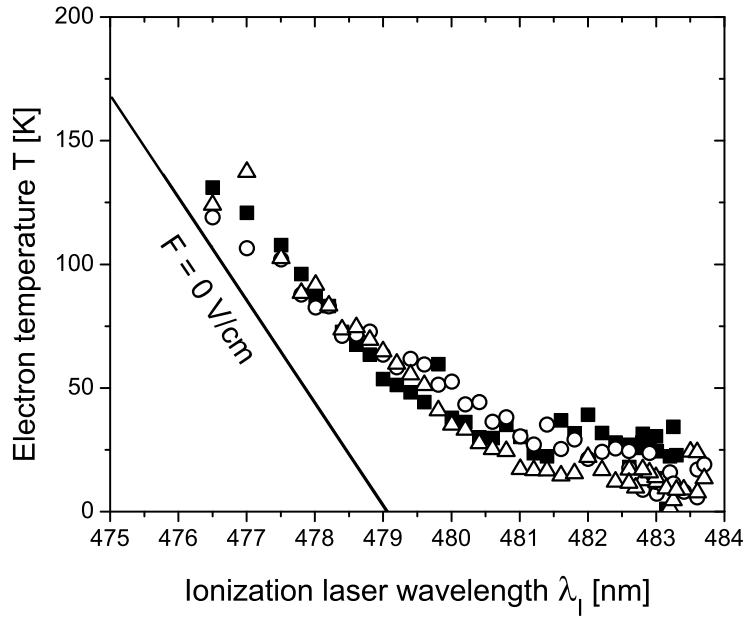


Figure 4.14: The fitted electron temperature as function of λ_I at 2200 V (square), 2300 V (circles), and 2400 V (triangles). The continuous line is for the field free model.

where $\mathcal{H} = 27.2$ eV, F is the externally applied electric field, and $F_0 = 5.14 \times 10^{11}$ V/m the atomic unit scaling factor. For a voltage of 2.3 kV, the corresponding electric field $F = 760$ V/cm lowers the ionization threshold wavelength from $\lambda_0 = 479.06$ nm to $\lambda_{0,F} = 482.95$ nm. Indeed, in the experiment of Fig. 4.14, we were able to observe electrons up to wavelengths closely corresponding with $\lambda_{0,F}$. For shorter wavelengths, the shift ΔE_{exc} can lead to an increase in temperature over that predicted by Eq. (4.3) if part of the additional energy becomes available as kinetic energy of transverse motion. For this electric field $F = 760$ V/cm and its corresponding ionization limit $\lambda_{0,F} = 482.95$ nm, the excess energy of Eq. (4.3) becomes 210 eV, which means, using the same equation, a temperature of 160 K. This can easily explain the observed shift of ≈ 40 K.

It is unclear what limits the electron temperature to the value of 15 K that we observe. It seems likely that this is an instrumental, rather than a fundamental limit. We have investigated a number of instrumental effects with the help of GPT. The effect of space-charge, ionization in a finite magnetic field, uncertainty in A and B coefficients, electron - atom and electron - ion interactions, aberrations in beam line, and MCP saturation are phenomena that have been investigated in detail. All these effects show an influence on the minimum detectable temperature, but the differences are very small, in the order of 1 K, and cannot fully explain the lowest temperatures measured in this experiment.

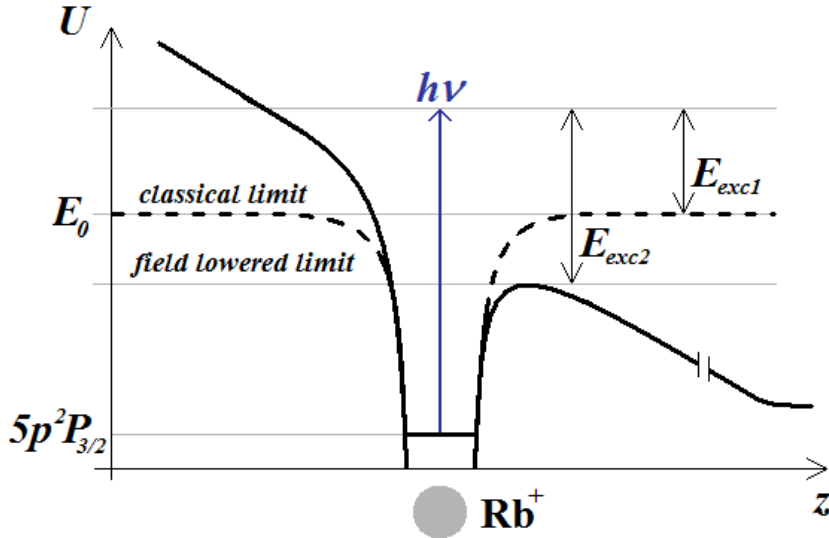


Figure 4.15: Electron energy around a rubidium atom inside the MOT.

4.6 Conclusions and outlook

In conclusion, we have produced electron bunches from a source size of $55 \mu\text{m}$, with charges in the order of 10 fC , bunch lengths of 4.7 ns , and measured temperatures down to 15 K . A thermal emittance as small as 0.0025 mm mrad can be calculated. This was actually the main idea of the new type of low emittance electron source based on cold atoms. Together with the other parameters, we calculate a normalized transverse brightness of $8 \times 10^9 \text{ A}/(\text{m}^2 \text{ sr})$, which is 3 orders of magnitude higher compared to the previously reported result of $2.9 \times 10^6 \text{ A}/(\text{m}^2 \text{ sr})$ [5]. The state-of-the-art LCLS photoinjector [19] produces beams with 1 nC charge, 5 ps bunch length, and an emittance of 1.2 mm mrad , resulting in a transverse brightness of $3 \times 10^{12} \text{ A}/(\text{m}^2 \text{ sr})$. Despite the very low electron temperature, the brightness of the present source still falls short of the state-of-the-art.

However, there are a few different possibilities to further improve the brightness of the cold-atoms-based electron source: to produce bunches with more charge, or to lower the bunch length. The first improvement can be realized by, e.g., increasing the trapped atom density. This will deliver from the same ionization volume more electrons. A disadvantage of this method is that space-charge effects spoil the emittance; however, this can be prevented by using ellipsoidal bunches [20]. The second improvement can be realized by applying a pulsed electric field instead of the present DC field, and subsequently make use of the velocity bunching effect [1]. In this case, the electrons can be temporarily "stored" in a UCP or a highly excited Rydberg gas before being extracted by the field pulse. In either

way, the bunch can get much shorter than the present 4.7 ns, and simulations show that a length in the range of a few tens of ps might be possible to be achieved. The brightness will become correspondingly higher, in the order of 10^{11} A/(m² sr). This is much closer to our goal presented in [1]. Experiments to achieve this goal are in progress.

Bibliography

- [1] B.J. Claessens, S.B. van der Geer, G. Taban, E.J.D. Vredenburg, and O.J. Luiten, *Phys. Rev. Lett.* **95**, 164801 (2005).
- [2] H.J. Metcalf, P. van der Straten, *Laser Cooling and Trapping* (Springer, Berlin, 1999).
- [3] T.C. Killian, T. Pattard, T. Pohl, and J.M. Rost, *Phys. Rep.* **449**, 77 (2007).
- [4] C. Hernandez-Garcia and C.A. Brau, *Nucl. Instr. Meth. Phys. Res. A* **483**, 273 (2002).
- [5] B.J. Claessens, S.B. van der Geer, G. Taban, O.J. Luiten, and E.J.D. Vredenburg, *Phys. Plasmas* **14**, 093101 (2007).
- [6] For an overview see P. Piot, in *The Physics and Applications of High Brightness Electron Beams* edited by J.Rosenzweig, G.Travish, and L.Serafini (World Scientific, Singapore, 2003).
- [7] G. Taban, M.P. Reijnders, S.C. Bell, S.B. van der Geer, O.J. Luiten, and E.J.D. Vredenburg, *Phys. Rev. ST Accel. Beams* **11**, 050102 (2008), Chapter 3 of this Thesis.
- [8] R.E. Kennerly, R.J. van Brunt, and A.C. Gallagher, *Phys. Rev. A* **23**, 2430 (1981).
- [9] D. Field, D.W. Knight, G. Mrotzek, J. Randell, S.L. Lunt, J.B. Ozenne, and J.P. Ziesel, *Meas. Sci. Technol.* **2**, 757 (1991).
- [10] A. Schramm, J. M. Weber, J. Kreil, D. Klar, M.-W. Ruf, and H. Hotop, *Phys. Rev. Lett.* **81**, 778 (1998).
- [11] K. Franz, T. H. Hoffmann, J. Bömmels, A. Gopalan, G. Sauter, W. Meyer, M. Allan, M.-W. Ruf, and H. Hotop, *Phys. Rev. A* **78**, 012712 (2008).
- [12] J.R. Dwyer, C.T. Hebeisen, R. Ernstorfer, M. Harb, V.B. Deyirmenjian, R.E. Jordan, and R.J.D. Miller, *Phil. Trans. R. Soc. A* **364**, 741 (2006).
- [13] O.J. Luiten, B.J. Claessens, S.B. van der Geer, M.P. Reijnders, G. Taban, and E.J.D. Vredenburg, *Int. J. Mod. Phys. A* **22**, 3882 (2007).
- [14] S. Humphries, Jr., *Principles of Charged Particle Acceleration* (John Wiley and Sons, 1999), pag. 127.
- [15] Ref. [14], pag. 165.
- [16] <http://www.pulsar.nl/gpt>.
- [17] J.H. Billen and L.M. Young, POISSON SUPERFISH, Los Alamos Nat. Lab. Rep. LA-UR-96-1834.
- [18] T.F. Gallagher, *Rydberg atoms* (Cambridge University Press, 1994).
- [19] R. Akre, D. Dowell, P. Emma, J. Frisch, S. Gilevich, G. Hays, Ph. Hering, R. Iverson, C. Limborg-Deprey, H. Loos, A. Miahnahri, J. Schmerge, J. Turner, J. Welch, W. White, and J. Wu, *Phys. Rev. ST Accel. Beams* **11**, 030703 (2008).

- [20] O.J. Luiten, S.B. van der Geer, M.J. de Loos, F.B. Kiewiet, and M.J. van der Wiel, Phys. Rev. Lett. **93**, 094802 (2004).

Pulsed field-ionization source⁴

Abstract.

We present measurements of the transverse momentum spread of pulsed electron beams created by field ionization of rubidium atoms in an excited Rydberg state. Rubidium atoms are firstly magneto-optically trapped at the center of an accelerator structure. Subsequently, they are excited to Rydberg states with principal quantum number between $n = 26$ and 35 , and then field ionized by a pulsed electric field with a slew rate of 58 (V/cm)/ns . Electron source temperatures in the order of 10 K are measured. The temperature is deduced from images of the electron pulses created on a phosphor screen, using a model of the beam transport system. An advantage of this method is that sub-ns temporal bunch lengths may be reached. Here, an upper limit for the length of 2 ns full-width-at-half-maximum is measured.

⁴The work described in this Chapter will be submitted for publication by G. Taban, B. Fleskens, M.P. Reijnders, O.J. Luiten, and E.J.D. Vredenburgt.

5.1 Cold electron sources

5.1.1 The new idea of a cold electron source

The new idea of a high brightness electron source based on cold atoms was proposed in [1]. This new type of pulsed electron source may allow advances of orders of magnitude in brightness compared to traditional photoemitters. In the first try to prove the feasibility of the new method [2], an experiment was carried out, where electrons were extracted from Rydberg atoms that develop into an ultracold plasma (UCP) [3]. The reported results show there an upper limit of 500 K for the electron source temperature, and a temporal bunch length of 200 ns full-width-at-half-maximum (FWHM). Recent measurements [4] brought the temperature upper limit down to only 15 K and the temporal bunch length to 4.7 ns FWHM. There, the free electrons are produced by photoionizing rubidium atoms near the ionization threshold in an already present DC electric field, which is also used to accelerate the electrons. To produce even shorter electron bunches, field ionization of Rydberg atoms can be employed [5]. The cold atoms can be excited very precisely to a Rydberg state and then, making use of a high voltage pulse, they are field ionized. The free electrons that are produced in this way should have comparable low temperatures at the source, but the bunches can be shorter because their length is no longer limited by the length of the ionization laser.

Lowering the electron temperature and shortening the bunch length is a way to improve brightness of the electron sources, because the 6D brightness is defined as the current density per unit solid angle subtended by the beam, and per unit energy spread. As discussed in [6], if the energy spread is not of high importance, the source is usually characterized by the so-called transverse brightness, defined as:

$$B_{\perp} = \frac{I_p}{4\pi^2 \varepsilon_x \varepsilon_y}, \quad (5.1)$$

where $\varepsilon_{x(y)}$ is the source emittance in the x (y) direction. The peak current I_p for a Gaussian bunch can be calculated from the total charge Q and the temporal bunch length σ_t :

$$I_p = \frac{Q}{\sqrt{2\pi}\sigma_t}. \quad (5.2)$$

The emittance of a thermal source is the product of the source size σ_x and the momentum spread σ_{p_x} :

$$\varepsilon_{th,x} = \frac{\sigma_x \sigma_{p_x}}{mc} = \sigma_x \sqrt{\frac{k_B T}{mc^2}}, \quad (5.3)$$

where k_B is the Boltzmann's constant, T the electron source temperature, m the electron mass, and c the speed of light. The peak current I_p in turn is inversely proportional to the bunch length. Therefore, if one is able to produce short pulses, the brightness will be further improved.

5.1.2 This experiment: an overview

In the experiment reported here, rubidium atoms are cooled and trapped in a magneto-optical trap (MOT) [7]. With the help of a tunable pulsed laser, a cylinder-like shape of these atoms is brought to different excited Rydberg states [5]. A fast electric field pulse is subsequently applied, and free electrons are produced by field ionization. The electrons are accelerated towards a detector by a specially designed accelerator structure [8]. Images of the cylinder-like electron beam are obtained on the detector. As in the previously reported experiment [4], a dependence between the size of the small axis of the cylinder and the beam energy can be obtained. On their way to the phosphor screen detector the electrons are first defocused by an electrostatic lens (the accelerator itself) and subsequently focused by a magnetic lens (the trapping coils). If the electrons are produced from different Rydberg states, they gain different energies in the accelerator. Due to the magnetic lens, this optical system is energy dependent. Therefore, the electrons obtained from different Rydberg states will be imaged differently on the detector. With the help of an optical matrix that describes the electromagnetic beam transport system, the size of the small axis of the cylinder is translated back to the initial electron source temperature. The detector can also be used to measure the bunch length. The focus in this article is on demonstrating that this source has low emittance, or equivalently that it has a low electron temperature.

The article is organized as follows: Section 5.2 presents the experimental setup, in Section 5.3 the procedure of measuring the electron temperature is explained in detail, in Section 5.4 the source temperature results are presented, and Section 5.5 contains a discussion of the implications of these measurements.

5.2 Experimental setup

The experimental setup used in this experiment is almost identical to the one described in [4] and is shown in Fig. 5.1. It consists of the components described below.

5.2.1 Electron production from cold atoms

Cooling and trapping of rubidium atoms. The starting point of the experiment is a classical magneto-optical trap (MOT) [7]. Rubidium atoms are cooled down and trapped by the $5s^2S_{1/2}(F = 3) \leftrightarrow 5p^2P_{3/2}(F = 4)$ optical transition in a 3D-vapor-cell MOT (Fig. 5.2). A cloud of about 3×10^7 atoms in a volume with a 3D-Gaussian distribution having a 0.9 mm standard deviation is created. The intensity of the trapping beams is such that at any time about 50% of the atoms are in the $5p^2P_{3/2}$ excited state. The magnetic field required for trapping is produced by two coils in an anti-Helmholtz configuration. Each coil has four windings with a radius of 72 mm. The distance between the centers of the two coils is 66 mm. A current up to 200 A flows through the coils.

Production of Rydberg atoms. To produce atoms in a Rydberg state, the rubidium atoms are excited from the upper level $5p^2P_{3/2}$ of the cooling transition with a pulsed dye laser operating on Coumarin 480 dye. By tuning the wavelength of the dye laser between

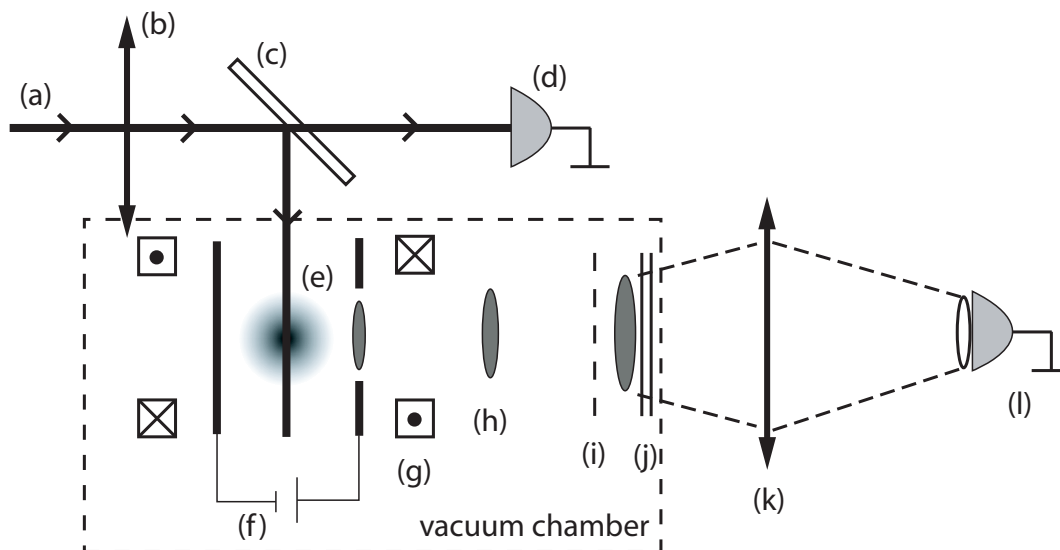


Figure 5.1: The experimental setup used in this experiment (not to scale): (a) ionization laser beam; (b) 500 mm lens; (c) partially transparent mirror; (d) CCD camera for monitoring of the ionization laser profile; (e) cloud of cold atoms; (f) accelerator electrodes; (g) trapping coils; (h) electron bunches; (i) grid; (j) MCP + phosphor screen assembly; (k) lens; (l) CCD camera for imaging the electron beam.

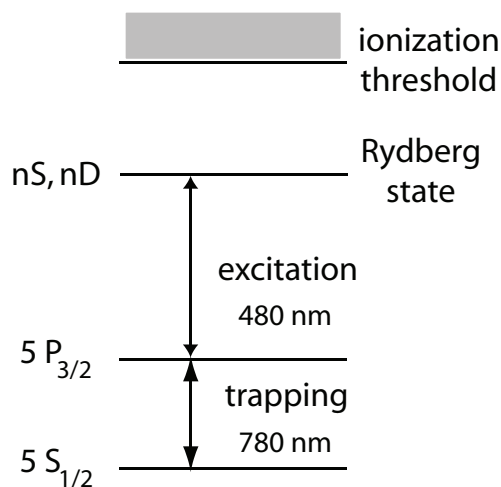


Figure 5.2: Simplified energy diagram of rubidium showing optical transitions used for trapping and for excitation of Rydberg states.

481 nm and 484 nm (tabulated in Table 5.1 [9]), nS and nD states with principal quantum number $n = 26$ to 35 are selectively produced. These states are characterized by a loosely bound valence electron, that is easily removed from the Rb^+ core by the action of an external electric field.

However, the external field also causes the Rydberg levels to split up due to the Stark

Table 5.1: Excitation wavelength, ionization field and output kinetic energy for each Rydberg state used in this experiment. The kinetic energies are calculated with GPT [12] and assume that the electrons start precisely at the acceleration point (for details see Subsection 5.3.2).

Rydberg state n	nS Excitation wavelength [nm]	nD Excitation wavelength [nm]	Adiabatic ionization field F_a [V/cm]	Diabatic ionization field F_d [V/cm]	Adiabatic kinetic energy [eV]	Diabatic kinetic energy [eV]
26	483.921	483.236	703	1250	956	1639
27	483.518	482.914	605	1075	834	1419
28	483.164	482.628	523	930	734	1237
29	482.850	482.373	454	808	650	1085
30	482.571	482.144	397	705	581	958
31	482.321	481.938	348	619	523	851
32	482.098	481.752	307	545	474	760
33	481.896	481.583	271	482	434	683
34	481.714	481.430	241	428	399	618
35	481.549	481.291	214	381	370	562

effect, and as a result the outer electron has to travel through a complicated energy landscape before it reaches the ionization threshold [5], [10]. For the Rydberg states used in this experiment, a so-called Stark-map is represented in Fig. 5.3(a). The dashed line represents the classical ionization field strength limit, which depends on the square of the energy E , according to

$$F = F_0 \left(\frac{E}{2\mathcal{H}} \right)^2, \quad (5.4)$$

where $F_0 = 5.142 \times 10^{11}$ V/m is the atomic unit for electric field, and $\mathcal{H} = 27.2$ eV.

The path that the electron follows through the Stark manifold is dependent on the slew rate of the external field. A simplified version of Fig. 5.3(a), used to explain the field ionization process, is shown in Fig. 5.3(b), with the ionization threshold represented by the thick continuous line. As shown in the figure, the nS and nD -states that we excite in the experiment are separated in energy from $n\ell$ states with $\ell > 2$. When the field is increased, they become entangled with the $n\ell$ manifolds before the ionization continuum is reached. If the field is turned on rapidly, a so-called diabatic path is followed (dashed line with ionization point (2)) and ionization occurs at a field value near $F_d = F_0/9n^4$ [5]. If, however, the field is turned on slowly, an adiabatic path is followed (dotted line with ionization point (1)), leading to field-ionization at a field closer to $F_a = F_0/16n^4 < F_d$. In between these cases, in general a large number of different paths to the ionization threshold have high probability, which results in a range of fields between F_a and F_d at which Rydberg atoms are ionized. Both diabatic and adiabatic ionization threshold fields are listed in Table 5.1 for states between $n = 26$ and 35, as used in the present experiment.

In this experiment, slew rates of 58 (V/cm)/ns are used, as further discussed in Subsec-

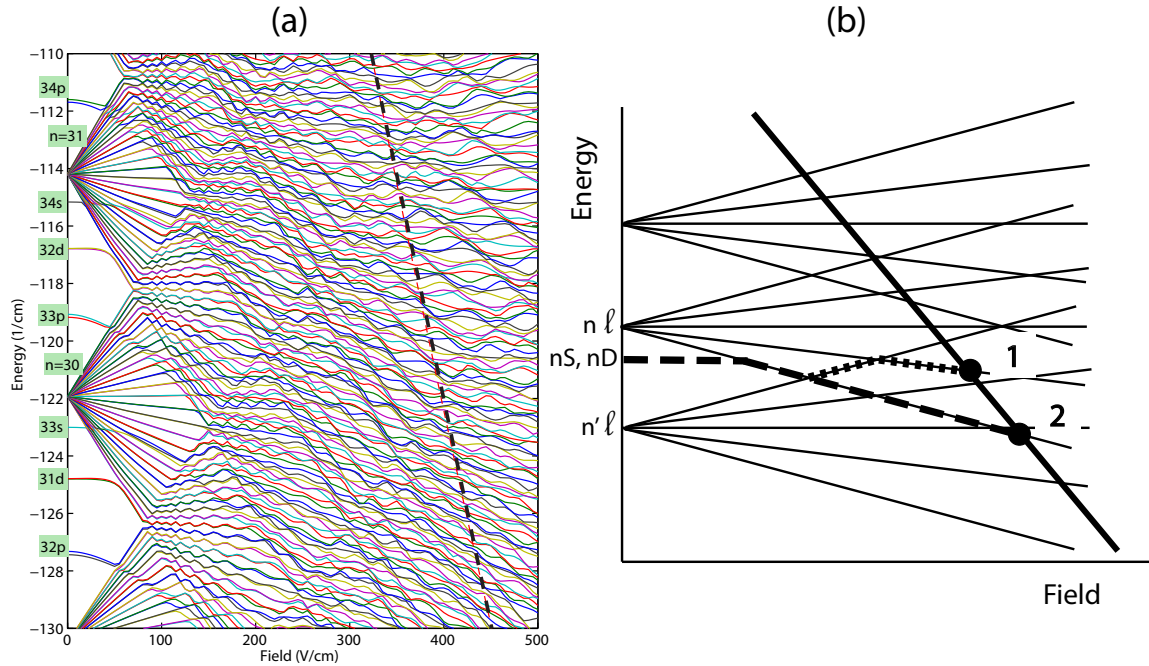


Figure 5.3: (a) Energy levels of rubidium as a function of the electric field around the $n = 30$ Rydberg state. The dashed line is the ionization threshold. (b) A simplified representation of the energy levels of rubidium as function of the electric field; the dashed lines are the ionization pathes, either adiabatic (1) or diabatic (2); the thick continuous line is the ionization threshold.

tion 5.2.2. Comparing to the work reported by Gürtler *et al.* [11], who observed that, for rubidium, field ionization is mostly diabatic for $n = 32$ already at slew rates of 1 (V/cm)/ns , it seems that we should expect to be operating far into the diabatic regime. As it is somewhat uncertain, however, at which electric field the states that we excite ionize, it becomes necessary to measure the resulting beam energy U . The method for doing this is explained in Subsection 5.3.2. However, the kinetic energies reported in Table 5.1 are obtained via simulations with GPT assuming the corresponding tabulated ionization fields.

5.2.2 Charged particle beamline

Accelerator and pulsed high voltage. The atoms are trapped at the acceleration point of a specially designed accelerator [8]. In this experiment, a high voltage pulse with a 3 kV amplitude and a rise time of 17 ns is used, resulting in a slew rate of 58 (V/cm)/ns . A typical pulse (continuous line), is shown in Fig. 5.4. The high voltage pulse arrives at the acceleration point, about 200 ns after the excitation laser pulse (dashed line).

The other components, i.e., the dedicated accelerator, the electric and magnetic lenses, and an optical description of the system are in detail described in Chapters 3 and 4.

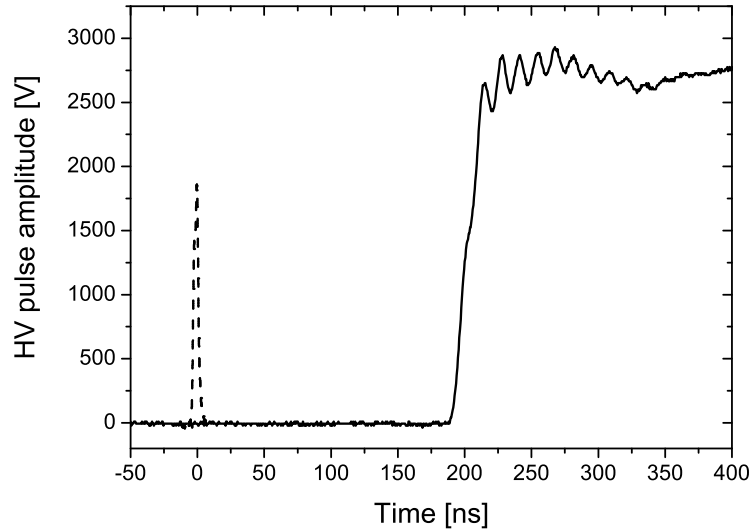


Figure 5.4: A typical high voltage pulse from the high voltage power supply used in the experiment (continuous line). The dashed line indicates the excitation laser pulse.

5.2.3 Electron bunch detection

Detection system. The detection system is the same as the one used in the previous experiment [4]. At a distance of 282 mm from the acceleration point, an assembly consisting of a microchannel plate (MCP) together with a phosphor screen is placed (Fig. 5.1(j)). The field created at the MCP is screened from the rest of the setup by a grounded grid placed 22 mm in front of the MCP (Fig. 5.1(i)). The MCP has an effective circular detection area with a 40 mm diameter. A charged couple device (CCD) camera acquires the images from the phosphor screen with a magnification of 0.4, giving a resolution of $21.35 \mu\text{m}/\text{pixel}$.

Optical description of the system. This system, consisting of an electrostatic lens and a magnetic lens, can be described with an "optical" model. It translates the information present in a system at an initial stage to the information of the final stage via a 2×2 matrix. For each particle, the final parameters as they hit a detector plane (particle position x_f and divergence x'_f) are converted back to the initial values (particle position x_i and divergence x'_i) via

$$\begin{pmatrix} x_f \\ x'_f \end{pmatrix} = \begin{pmatrix} A & B \\ C & D \end{pmatrix} \begin{pmatrix} x_i \\ x'_i \end{pmatrix}. \quad (5.5)$$

For this system, the A and B coefficients have been determined using GPT [12], as explained in [4]. Because the current through the trapping coils is different here, i.e., 175 A, the A and B coefficients are different. They are shown in Fig. 5.5.

Bunch length measurement. In the previous experiment [4], the temporal bunch length was limited by the length of the ionization laser pulse to 4.7 ns FWHM. Here,

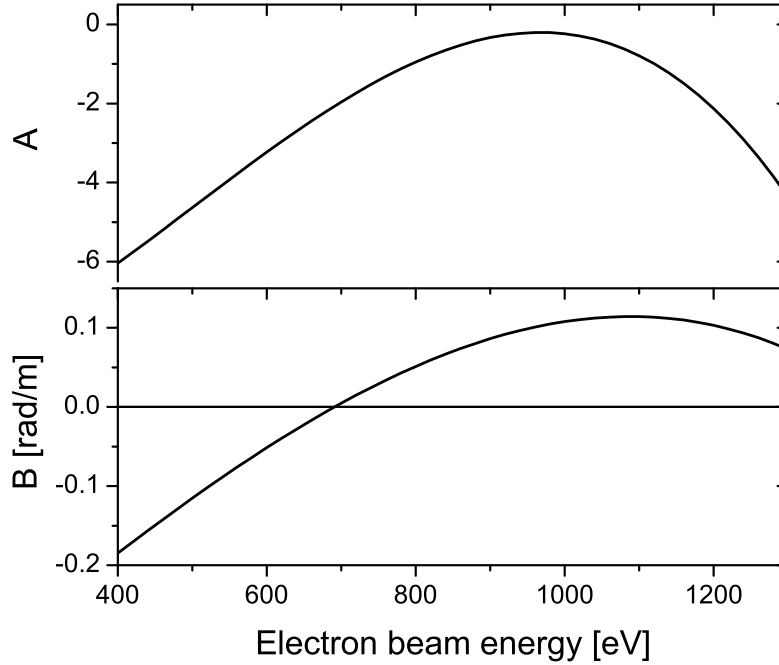


Figure 5.5: The optical coefficients A and B as function of beam energy.

however, all electrons are simultaneously extracted. If indeed this is the case, then, from the GPT simulations, a bunch length of about 50 ps FWHM is expected at the detector, limited by the spread in beam energy due to the $\sim 50 \mu\text{m}$ spatial extent of the excited atom cloud. This represents a large improvement with respect to the previous experiment.

In practice, a few effects also influence the minimum bunch length that can be obtained at the detector. Firstly, the electric field is not perfectly uniform along the entire ionization volume and in practice not all the atoms will be ionized at the same time. For an rms beam size σ_{x_i} , one can estimate an rms field inhomogeneity of $\sigma_F/F \simeq 7 \times 10^{-3}$. The minimum initial temporal spread would amount to $7 \times 10^{-3} \times \text{rise time}$ (10 ns), i.e., a minimum of $\simeq 70$ ps bunch length. Secondly, the lifetime of the Rydberg states employed here is not very well known, especially since the electric field continues to rise above the field ionization limit. This may also give a minimum bunch length [5]. Thirdly, as suggested in Subsection 5.2.1, Fig. 5.3, if the atoms follow different paths to the ionization threshold, this results in a range of fields at which Rydberg atoms are ionized. Given a slew rate of 58 (V/cm)/ns, this could mean a large spread in the ionization field, which subsequently means a bunch length that might be substantially larger than 50 ps.

To check in practice these effects, the bunch length has been measured directly on a 50 Ω terminated oscilloscope, by bleeding the charge directly from the front side of the

MCP (used as a Faraday cup). Following the electron signal in time, a bunch length of 2.0 ns FWHM has been measured (Fig. 5.6). It is indeed, as expected, shorter than the previous result of 4.7 ns FWHM [4], showing that the bunch length is no longer limited by the pulse length of the laser. At this moment it is not known if the time response of the electronics is the cause of the relatively long bunch length. A future experiment will try to clarify this question.

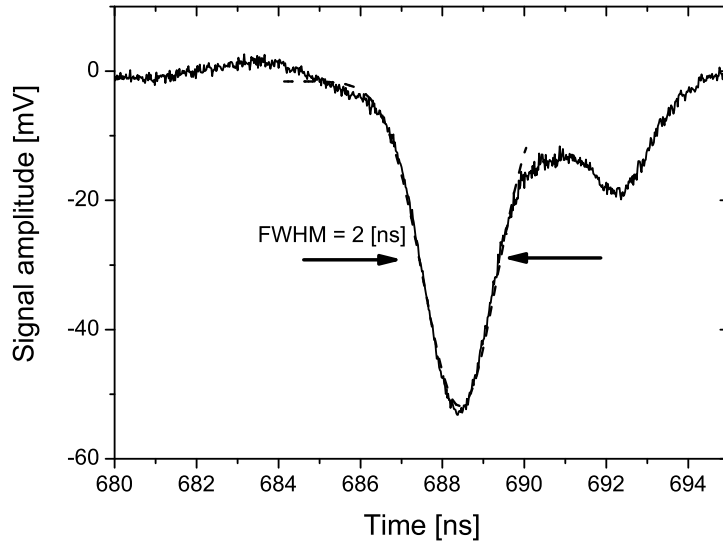


Figure 5.6: The beam current as function of time measured on the MCP as an electrical signal. A temporal bunch length of 2 ns FWHM is extracted from this figure.

Bunch charge. To measure the bunch charge, the MCP was again used as a Faraday cup. Charges of up to 10 fC were typically used in this experiment.

5.3 Measurement procedure

5.3.1 Temperature determination using different Rydberg states

To determine the electron temperature at the source, the variation of the size of the small axis of the cylinder-like beam as function of the kinetic energy of the bunches is followed. From the optical model of Subsection 5.2.3, this behavior is described by:

$$\sigma_{x_f}^2 = A^2 \sigma_{x_i}^2 + B^2 \sigma_{x'_i}^2, \quad (5.6)$$

where σ_{x_i} is the rms initial size, $\sigma_{x'_i}$ the initial divergence of the beam, and A and B the optical matrix coefficients. The initial rms divergence $\sigma_{x'_i}$ of the beam can be written as

the ratio between the rms transverse velocity σ_{v_x} and the longitudinal velocity v_z , which in turn can be related to an effective source temperature T :

$$\sigma_{x'_i} = \frac{\sigma_{v_x}}{v_z} = \sqrt{\frac{k_B T}{2eU}}, \quad (5.7)$$

where U is the beam energy in eV.

The method used to determine the electron source temperature is equivalent to the one used previously in Chapter 4, i.e., it is extracted from the dependence of the beam size at the detector on the beam energy, with the help of Eqs. (5.6) and (5.7). In [4], different DC voltages were applied on the accelerator to vary the electron kinetic energies up to 1800 eV. Here, different Rydberg states are employed to obtain a variation of the beam energy. The cooled and trapped atoms are first excited to a Rydberg state. After the atoms are excited, the electric field is switched on. Because each of these Rydberg states ionizes at a different electric field amplitude, the free electrons gain a different kinetic energy for each value of the principal quantum number n . The states chosen in this experiment provide free electrons within the same energy range $U = 300 - 1700$ eV as in the previous experiment [4].

5.3.2 Beam energy measurement

Given the uncertainties discussed in Subsection 5.2.1, an important issue is to measure the kinetic energy of the electron bunches produced from different Rydberg states. The method employed here to measure the energy uses some additional results of the DC electric field experiment not yet reported in [4]. There, the dependence between the voltage on the accelerator and the kinetic energy was accurately established. Under the influence of the magnetic field created by the trapping coils, the beam also rotates while traveling through the system. As shown in [13], the rotation angle φ depends inversely proportional on the square root of the kinetic energy:

$$\varphi(z_{det}) = -\frac{e}{2m} \int_0^{z_{det}} \frac{B_z(0, z)}{v_z(z)} dz \simeq -\int_0^{z_{det}} \frac{eB_z(0, z)}{\sqrt{8mU}} dz, \quad (5.8)$$

where $B_z(0, z)$ is the longitudinal magnetic field on the symmetry axis, and the upper limit z_{det} of the integration is the distance to the detector. When the images of the beam as recorded on the screen are fitted, the rotation angle the beam makes with the initial vertical orientation is also determined. For the experiments presented in [4], a current of 190 A through the trapping coils was used. The dependence between the rotation angle and the well known kinetic energy for that experiment is shown in Fig. 5.7. It is in a very good agreement with the expected behavior of Eq. (5.8). It can be seen that the rotation angle cannot be very well determined if the beam energy is in the neighborhood of 1000 eV, the electron bunch being there in focus. In this case, the projection on the screen is nearly circular and the fit program can not properly determine the rotation angle.

The function that fits these data depends inversely on the square root of the kinetic energy, as expected from Eq. (5.8). The fit can be further used as calibration. Knowing

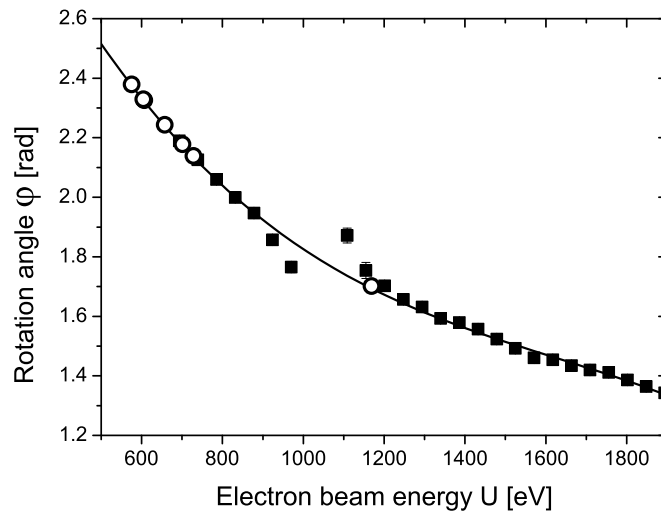


Figure 5.7: Rotation angle as function of beam energy in the DC experiment [4], for a current of 190 A through the trapping coils. The full squares are the experimental points, the continuous line is a fit with a $1/\sqrt{U}$ dependence, and the open circles the Rydberg states used in the present experiment.

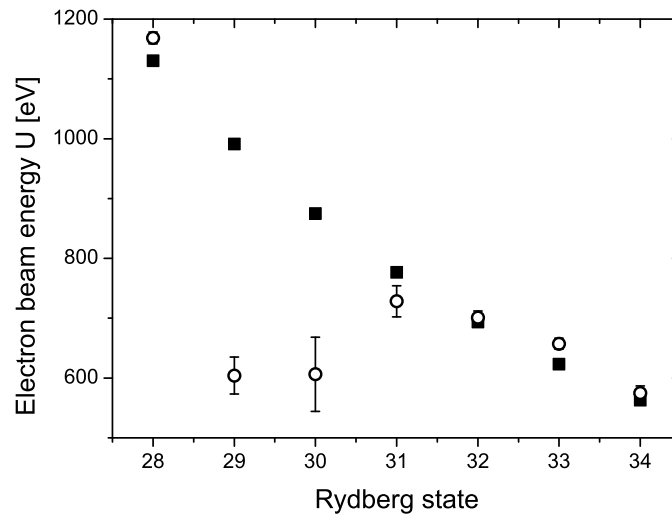


Figure 5.8: Beam energy for different Rydberg states, compared to GPT simulations described in the text. The full squares are the GPT results and the open circles are the energies determined from the rotation angle.

the rotation angle, one can calculate the corresponding beam energies. For a current of 190 A, this method was used for different Rydberg states, where the kinetic energy was unknown, and the results are represented in Figs. 5.7 and 5.8. Please note that the S and D Rydberg states for the same principal quantum number gain the same energy. In Fig. 5.8, the results of this method are compared to GPT simulations. In the calibration experiment, the ionization volume is at about 1 mm off of the acceleration point, therefore the GPT simulations are also carried out with this offset in the initial position of the bunch. Consequently, there is a difference of about 10% between the values of Table 5.1 and the simulated energies of Fig. 5.8. Nevertheless, the tabulated values of kinetic energy are calculated for the actual acceleration point. The diabatic value of ionization field F_d is used in the GPT simulations. The time dependence of the electric field pulse is similar to the one shown in Fig. 5.4. A high voltage pulse with the same amplitude of 3 kV was used for all Rydberg states. After the field reaches the ionization value given in Table 5.1 for each Rydberg state, the electrons are considered free. Both results, of the GPT simulations (full squares) and of the experimental values (open circles), are presented in Fig. 5.8. Except for $n = 29$ and $n = 30$, a very good match between the two can be observed. At $n = 29$ and $n = 30$, the beam is focused, so the rotation angle cannot be measured accurately in the experiment.

5.3.3 Data analysis

The images as obtained on the phosphor screen are fitted with a 2D-Gauss distribution as explained in [4]. A value for the small axis σ_{x_f} is obtained from this fit. Because in this experiment the ionization laser pulse does not always have exactly the same wavelength, a different number of electrons are extracted with each pulse. Also because all the electrons are extracted in a short time interval from the trapped atom cloud, space-charge effects are here more likely to occur than in [4], where the electrons were extracted one by one in a quasi-continuous current. To correct for the influence of space-charge, an extra term that depends on the charge Q can be added to Eq. (5.6):

$$\sigma_{x_f}^2 \simeq A^2 \sigma_{x_i}^2 + B^2 (\sigma_{x_i}^2 + C_q Q). \quad (5.9)$$

The average potential energy of an electron in the bunch is proportional to Q . This gives an additional transverse velocity v_q that depends on the square root of charge Q . It induces an extra expansion of the bunch and thus contributes to a larger transverse size on the detector, proportional to \sqrt{Q} .

For each Rydberg state, if the square of the small axis $\sigma_{x_f}^2$ is plotted as function of the total charge for each shot, as in Fig. 5.9, a linear dependence is found, as expected. It is important to mention that what is here called charge is in fact the total amount of light collected from the phosphor by the CCD camera for each shot. From the linear fit of this dependence, the value of σ_{x_f} for zero charge is obtained and used in Section 5.4.

From Eq. (5.9), one would expect the slope $d\sigma_{x_f}^2/dQ$ to be proportional to B^2/U . However, the comparison in Fig. 5.10 shows that this is not the case. The reason for this

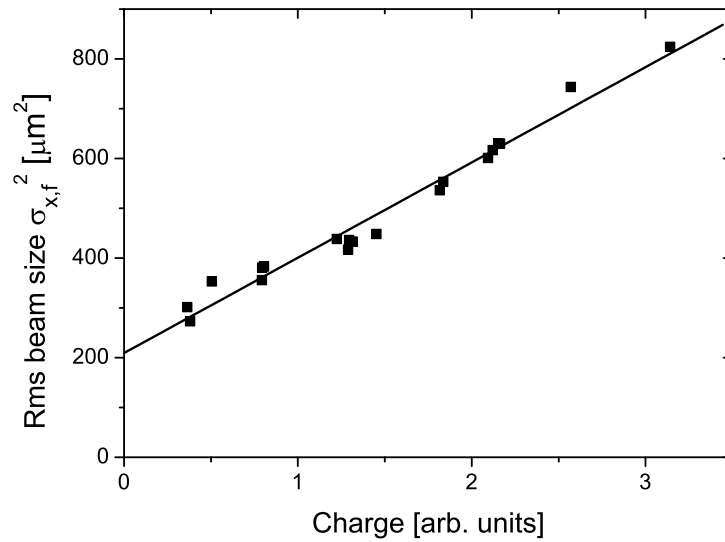


Figure 5.9: The square of the beam size at the detector as function of charge, here for the $31S$ Rydberg state.

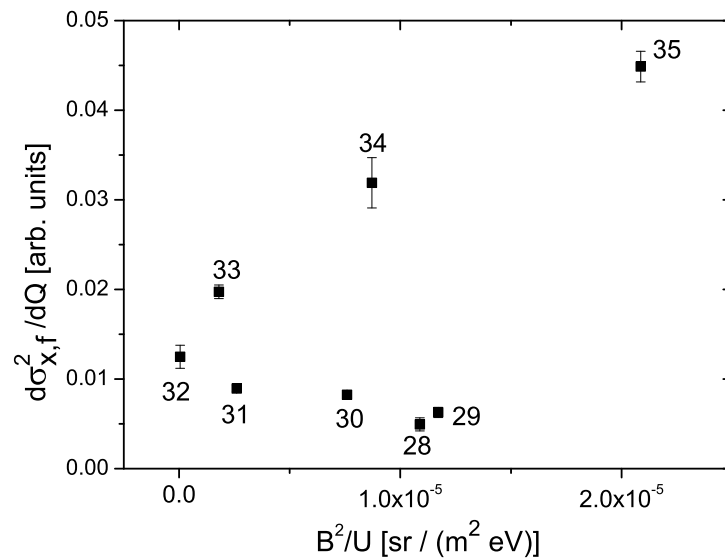


Figure 5.10: The slope of the linear fit from Fig. 5.9 as function of B^2/U , for each Rydberg state.

is at present not clear.

5.4 Experimental results

Now that the kinetic energies U of different states are known and the rms beam size at the detector σ_{x_f} is calculated for charge $Q = 0$, the rms beam size can be represented as function of U . All experimental data for the S and D states are fitted together with Eq. (5.6). A common rms initial size σ_{x_i} of $31 \pm 4 \mu\text{m}$ is obtained, and the kinetic energy U is scaled as αU , with the α scaling factor of 0.92 ± 0.02 , which is also in accordance with the energy scaling factor reported in [4]. The effective source temperature T is specific for each data set.

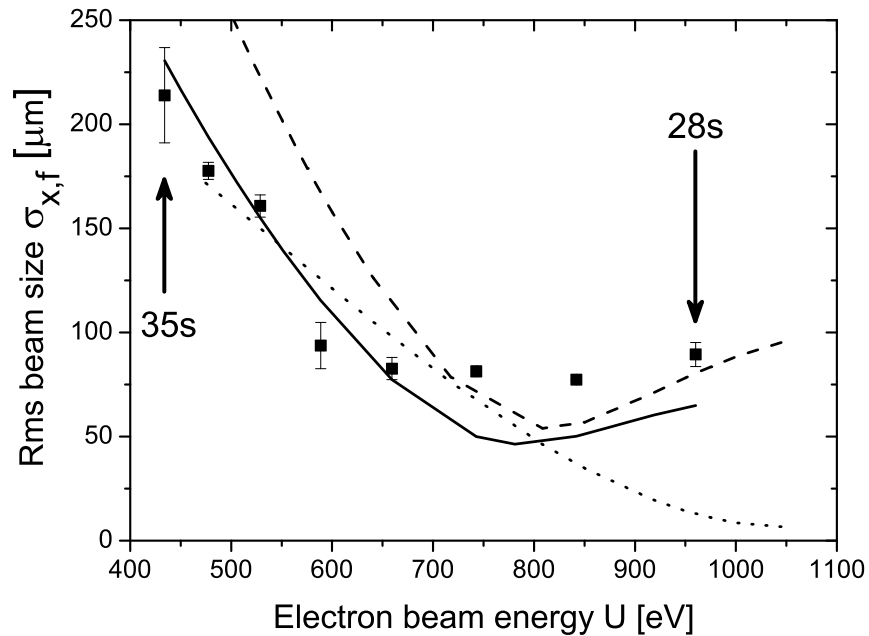


Figure 5.11: Zero charge beam size on the detector as function of the beam energy, for different S -Rydberg states. The continuous line gives the best fit for the electron temperature (9 K), the dashed line is a representation for 21 K, and the dotted line is a representation for 0 K.

When Rydberg S states between $n = 28$ and 35 are used, the resulting zero charge beam size on the screen as function of the beam energy is given in Fig. 5.11. The model of Eq. (5.6) for the best fit gives an electron temperature of 9 ± 4 K and is represented by the continuous line. This gives a reasonable representation of the data, in particular at lower energies. Choosing an electron temperature three standard deviations σ higher, i.e., 21 K, the dashed line in Fig. 5.11 is obtained, while choosing an electron temperature 3σ lower,

i.e., 0 K, the dotted line is obtained. We conclude that electron temperatures in the order of 10 K have been obtained.

The same can be done for Rydberg D states between $n = 26$ and 35 and the result is given in Fig. 5.12. The model of Eq. (5.6) for the best fit gives an electron temperature of 36 ± 5 K and is represented by the continuous line. This model fits the experimental points very well. By choosing an electron temperature 3σ higher, i.e., 51 K, the dashed line is given in Fig. 5.12. By choosing an electron temperature 3σ lower, i.e., 21 K, the dotted line is given in Fig. 5.12. From these three representations we conclude that the effective source electron temperatures is indeed very low, in the order of 36 K.

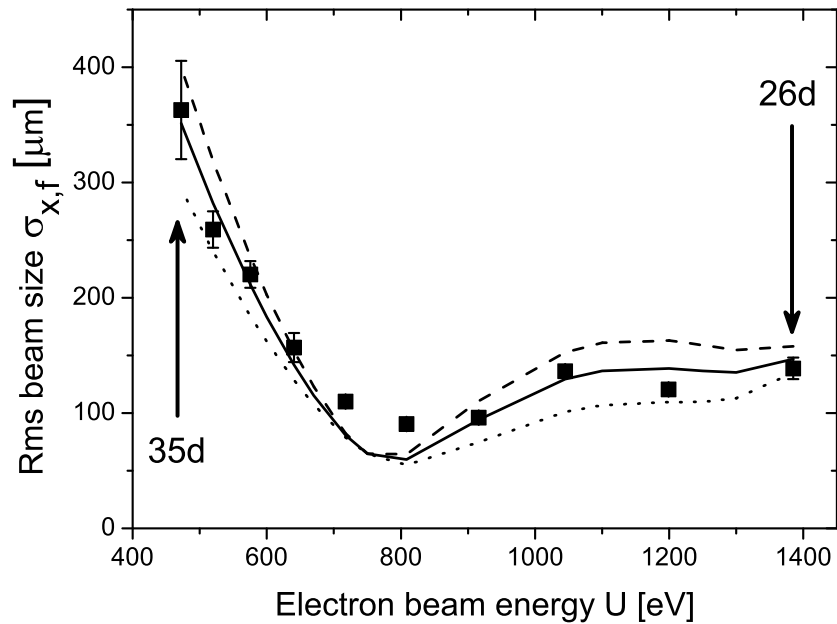


Figure 5.12: Beam size on the detector as function of energy, for different D -Rydberg states. The continuous line gives the best fit for the electron temperature (36 K), the dashed line is a representation for 51 K, and the dotted line is a representation for 21 K.

5.5 Conclusions and outlook

In conclusion, we have produced pulsed electron bunches from Rydberg excited states. A source size of $30 \mu\text{m}$, charges up to 10 fC, and temperatures in the order of 10 K have been measured. Together with the measured source temperature of 15 K reported in [4], it seems that this is the detection limit for our system. An upper limit for the bunch length of 2 ns FWHM was obtained, probably limited by the response time of the electronics. As discussed earlier, bunch lengths nearer to ~ 50 ps should be expected.

At this moment, the system is limited by the high voltage power supply to a few Rydberg states that can be used. If one wants to obtain higher energy beams, Rydberg states with a lower quantum number can be employed. The required ionization fields will be much higher and consequently also the energy that the electrons will gain. The high voltage power supply described in [8] can switch voltages of up to 30 kV, therefore Rydberg states up to $n = 15$ can be field ionized. However, because the focal length of the beam transport system for these higher energies is too long to focus the beam on the detector, here it was not possible to perform the same analysis for Rydberg states with such a low n . An additional focusing element such as an Einzel lens should be added to the system. Experiments in this regime are reported in Chapter 6.

Bibliography

- [1] B.J. Claessens, S.B. van der Geer, G. Taban, E.J.D. Vredenburg, and O.J. Luiten, *Phys. Rev. Lett.* **95**, 164801 (2005).
- [2] B.J. Claessens, S.B. van der Geer, G. Taban, O.J. Luiten, and E.J.D. Vredenburg, *Phys. Plasmas* **14**, 093101 (2007).
- [3] T.C. Killian, S. Kulin, S.D. Bergeson, L.A. Orozco, C. Orzel, and S.L. Rolston, *Phys. Rev. Lett.* **83**, 4776 (1999).
- [4] G. Taban, B. Fleskens, M.P. Reijnders, E. Sachteleben, O.J. Luiten, and E.J.D. Vredenburg, *to be submitted*, Chapter 4 of this thesis.
- [5] T.F. Gallagher, *Rydberg atoms* (Cambridge University Press, 1994).
- [6] O.J. Luiten, B.J. Claessens, S.B. van der Geer, M.P. Reijnders, G. Taban, and E.J.D. Vredenburg, *Int. J. Mod. Phys. A* **22**, 3882 (2007).
- [7] H.J. Metcalf, P. van der Straten, *Laser Cooling and Trapping* (Springer, Berlin, 1999).
- [8] G. Taban, M.P. Reijnders, S.C. Bell, S.B. van der Geer, O.J. Luiten, and E.J.D. Vredenburg, *Phys. Rev. ST Accel. Beams* **11**, 050102 (2008), Chapter 3 of this thesis.
- [9] J.E. Sansonetti, *J. Phys. Chem. Ref. Data* **35**, 301 (2006).
- [10] M.G. Littman, M.M. Kash, and D. Kleppner, *Phys. Rev. Lett.* **41**, 103 (1978).
- [11] A. Gürtler and W.J. van der Zande, *Phys. Lett. A* **324**, 315 (2004).
- [12] <http://www.pulsar.nl/gpt>.
- [13] S. Humphries, Jr., *Principles of Charged Particle Acceleration* (John Wiley and Sons, 1999), pag. 127.

6

High energy bunches

Abstract.

As a continuation of the experiments presented in Chapter 4 and 5, a method to produce electron bunches with high energy and a low source temperature is presented here. Rydberg atoms with principal quantum number n between 15 and 25 are employed. It is shown that energies up to 14 keV can be reached. Source temperatures of about 15 K are expected, but, due to major discrepancies in the measurements, it is not possible to determine the source temperature unambiguously.

6.1 Introduction

This chapter is a continuation of the experiments already carried out, whose results are presented in Chapter 4 and 5. The goal here is to produce bunches with high kinetic energy and low source temperature. This chapter presents the measurements carried out to show how this goal can be achieved.

In the experiments described in Chapter 4 (see Table 6.1), electrons were produced by photoionization of cooled and trapped rubidium atoms. After creation, they were instantaneously extracted by a DC electric field. In that experiment, electrons with energies up to 2.5 keV were produced. The source temperature was measured to be 15 K. A temporal bunch length was measured of 4.7 ns FWHM, which was limited by the ionization laser pulse length.

In the experiments described in Chapter 5 (see Table 6.1), Rydberg atoms with principal quantum numbers between 26 and 35 were employed. The cooled and trapped rubidium atoms were excited to different Rydberg states. They were subsequently field ionized by a pulsed electric field. The electrons obtained with this method have a measured temperature at the source in the same range, of about 10 K. An improvement with this experiment was that the temporal bunch length was measured to be 2 ns FWHM. The kinetic energies were in the same range as in Chapter 4, limited to a few keV.

As suggested in Chapter 5, with the present setup there is the possibility of producing cold electrons with even higher energies, if Rydberg states with the principal quantum number n lower than 26 are employed. They can be excited by the same pulsed dye laser, and can be field ionized by the electric fields produced by the power supply described in [1] (Chapter 3 in this thesis). Therefore, Rydberg states down to $n = 15$ can be reached, which in turn means kinetic energies of the electron bunches up to 14 keV. However, for these energies, the solenoidal magnetic lens cannot focus the electron beam on the detector screen. The spot size is for a single shot bunch too large and too weak to be properly analyzed. The solution to overcome this problem is to use an additional optical element that can focus the electrons on the detector. The choice was made for an electrostatic lens, an Einzel lens. The focal length of the lens can be modified by changing the DC voltages applied to the lens.

Table 6.1: The experimental results of the present research project as reported in Chapters 4 and 5.

Source	Rms size σ_x	Temp. T [K]	Charge Q	Bunch length σ_t	Emittance ε [mm mrad]	Brightness B_{\perp} [A/(m ² sr)]	Ref.
Pulsed 1	50 μm	15	10 fC	2 ns	0.0025	8×10^9	Ch. 4
Pulsed 2	30 μm	10	10 fC	0.85 ns	0.0012	8×10^{10}	Ch. 5

6.2 Experimental setup

The experimental setup is represented schematically in Fig. 6.1. It is the same setup used in Chapter 4 and Chapter 5, with an additional element, the Einzel lens. Rubidium atoms are cooled and trapped in a magneto-optical trap [2]. Subsequently, they are excited to a Rydberg state and from there field ionized [3]. The electrons are extracted and accelerated by a specially designed accelerator structure (Chapter 3). On their way to the detector screen, the electrons interact with a beam transport system, which consists of an electrostatic lens (the exit hole of the accelerator), a magnetic lens (the trapping coils), and another electrostatic lens (the Einzel lens). The size of the bunch on the screen can be related via an "optical" model to the electron temperature of the source. The focus in this chapter is on Rydberg atoms with principal quantum number n between 15 and 25. Also the design and the working principle of the Einzel lens are discussed.

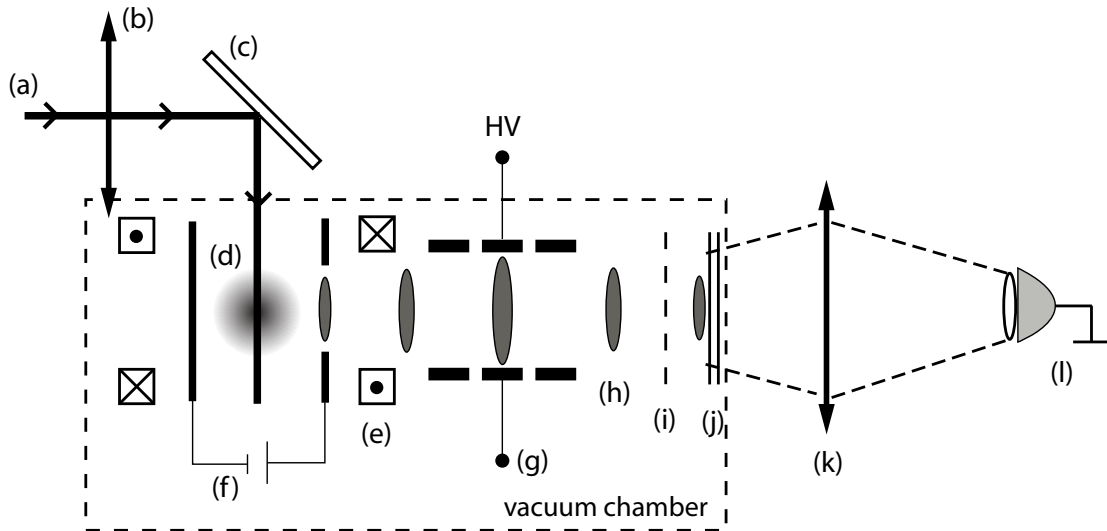


Figure 6.1: The experimental setup used in this experiment (not to scale): (a) pulsed dye laser beam; (b) 500 mm lens; (c) partially transparent mirror; (d) cloud of cold atoms; (e) trapping coils; (f) accelerator electrodes; (g) Einzel lens; (h) electron bunches; (i) grid; (j) MCP + phosphor screen assembly; (k) lens; (l) CCD camera for imaging the electron beam.

6.2.1 Production of high energy electron bunches from Rydberg atoms

The wavelength λ of the pulsed dye laser can be tuned in very small steps so that individual Rydberg states can be excited. With the Coumarin 480 dye, a large range of wavelengths around 480 nm can be achieved (the required wavelengths are listed in Table 6.2). Also the electric fields for ionization of states up to $n = 15$ are achievable [3]. The kinetic energies U of electrons resulting from this field ionization process, assuming diabatic ionization and electrons starting precisely at the acceleration point, are calculated with the General Particle Tracer (GPT) code [4] and presented in Table 6.2. Two high voltage pulsed power

supplies were used in these experiments, one that switches a maximum voltage of 3 kV in 17 ns (also used in the experiments presented in Chapter 5) and another one, described in detail in Chapter 3 and [1], that switches a maximum of 30 kV in 30 ns. A check has been carried out to see if all these Rydberg states can indeed be found. The corresponding wavelengths are in very good agreement with the tabulated values [5] and from each state free electrons could indeed be produced by field ionization.

Table 6.2: Excitation wavelength, ionization field and output kinetic energy for each Rydberg state used in this experiment. The power supply described in Chapter 5 is used for the $28S$ state, and the power supply described in Chapter 3 is used for all other Rydberg states.

Rydberg state n	Excitation wavelength λ [nm]	Diabatic ionization field F_d [kV/cm]	Kinetic energy U [keV]
$28S$	483.164	0.93	1.24
$22D$	485.034	2.44	3.37
$19D$	487.274	4.38	5.73
$15D$	492.951	11.29	14.00

6.2.2 Einzel lens

When the electrons are created, they experience an electric field that accelerates them towards the detector. When leaving the accelerator structure, the pulsed beam is defocused due to the exit kick of the exit accelerator hole and then focused by a solenoidal magnetic lens. In Chapter 5, bunches with energies up to 2.5 keV were produced. For higher beam energies, for example in the order of 14 keV, produced in this experiment, the beam is totally defocussed. To be able to detect single shot beam images on the detector screen, one has to focus the beam back with the help of an extra optical element. An Einzel lens was chosen.

A technical drawing is presented in Fig. 6.2. The Einzel lens consists of three conducting rings with an inner diameter of 30 mm and a outer diameter of 35 mm, each separated by a gap of 5 mm. The first ring and the third ring are 10 mm long, the middle ring is 20 mm long. The distance is fixed by two ceramic rings made of Boron Nitride (relative permittivity $\epsilon_r = 4$). The distance between the accelerator and the first ring is 45.3 mm, as indicated in Fig. 6.2. The Einzel lens was designed such that a maximum DC voltage V_E of 30 kV can be applied on the middle ring. The middle ring is connected via a high voltage feedthrough to a 30 kV DC power supply. The outer rings are grounded.

In [6] the action of an Einzel lens is explained in detail. The beam envelope is indicated schematically in Fig. 6.3 and was generated in a standard GPT simulation. The equipotential field lines represented in the map are generated with SUPERFISH [7]. The focusing action of the lens comes from the change in the radial position r of the electrons, and also from the change in their longitudinal velocity v_z . In the first gap, the particles are first deflected inward when they enter the gap, then deflected outward as they exit the gap. The opposite takes place at the second gap, i.e., the particles are first deflected outward

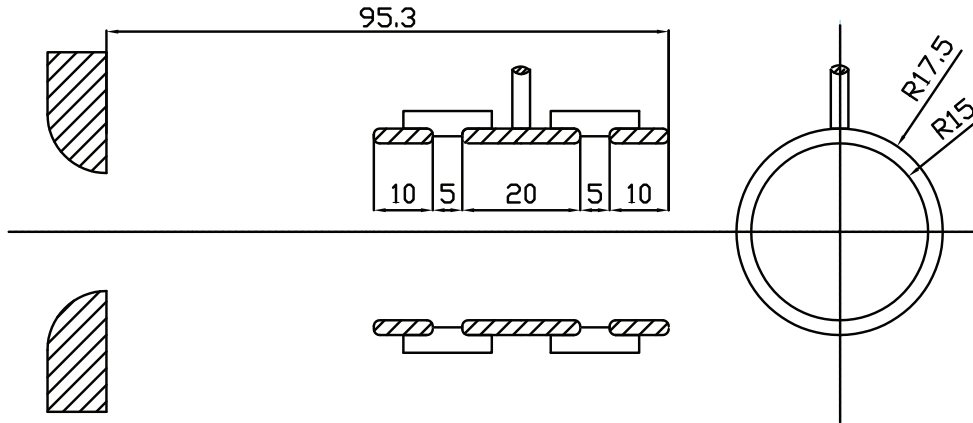


Figure 6.2: Technical drawing of the Einzel lens used in this experiment. Left is a side view of the Einzel lens together with the exit hole of the accelerator. Right is a front view of the lens. All dimensions are in mm.

and then inward. These deflecting actions do not cancel because the electrons are either accelerated or decelerated while crossing the gaps. The overall effect is focusing (an Einzel lens is always a positive lens), because, when deflected inward, the longitudinal velocity v_z is lower and the action of the lens stronger. Also important is that, when they exit the lens, the electrons will regain their initial speed, so the kinetic energy is not modified by an Einzel lens.

6.2.3 Optical matrix

As done previously in Chapter 4 and 5, also this system can be described with an optical matrix, whose elements were calculated with GPT, as explained in Chapter 4. The optical system consists here of a negative electrostatic lens (the accelerator), a positive magnetic lens (the trapping coils), and a positive electrostatic lens (the Einzel lens). This time the matrix elements are not calculated as function of beam energy U , but for different voltages V_E applied on the Einzel lens. Because beams obtained from different Rydberg states have different kinetic energies (see Table 6.2), for each state used in this experiment, a specific optical matrix is built. The behavior of the optical matrix coefficients A and B for the Rydberg states used in this experiment as function of V_E is plotted in Fig. 6.4.

6.3 Method

The method to measure the source temperature T is equivalent to the method presented in Chapter 4 and 5. The behavior of the beam size on the detector σ_{x_f} is given by Eq. (5.6) and is written as function of the rms initial size σ_{x_i} and the initial rms divergence of the beam $\sigma_{x'_i}$. Here, for each measurement set, one single Rydberg state is employed, which means one specific beam energy U . To carry out a beam waist scan, different voltages are applied to the Einzel lens.

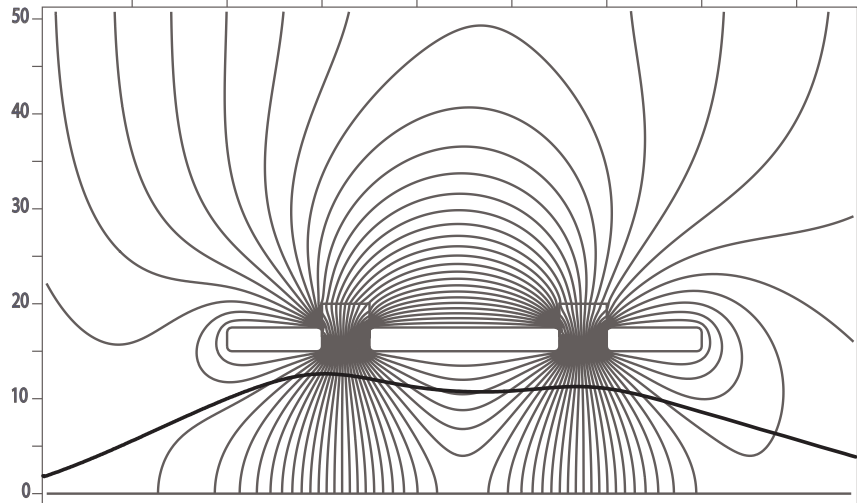


Figure 6.3: A representation of the equipotential electric field lines and the beam envelope (not to scale) in the Einzel lens. The field map is generated with SUPERFISH and the beam envelope with GPT.

To correct for the influence of different number of electrons extracted with each pulse and for the space-charge effects, as explained in Chapter 5, an extra term that depends on the total charge Q is added to Eq. (5.6). Eq. (5.9) is subsequently obtained. From the linear dependence expressed by this equation, the beam size σ_{x_f} for zero charge is obtained by linear regression of the data. It is further used as input for the analysis in Section 6.4.

6.4 Results

Three different experiments, with the $28S$, $22D$, and $19D$ Rydberg states have been carried out to measure the source temperature.

Firstly, with a wavelength $\lambda = 483.17$ nm, the $28S$ Rydberg state is selected. The high voltage power supply that switches 3 kV in 17 ns is used. The kinetic energy of the bunches is not precisely known, as explained in Chapter 5, Section 5.2; therefore it must be measured. The rotation that the bunches get from the magnetic field of the trapping coils is extracted from a fit of the images. Making use of the rotation angle vs. energy calibration of Chapter 5, the kinetic energy of the bunches can be found; in this case $U = 1250$ eV, close to the corresponding value given in Table 6.2. To gain this kinetic energy, the Rydberg atoms had to be ionized in an electric field $F = 1025$ V/cm. This is in agreement with the value for diabatic field ionization $F_d = 930$ V/cm, given the uncertainty in the field measurement.

Subsequently, the beam is scanned through a waist with the help of the Einzel lens. The variation of σ_{x_f} as function of V_E is shown by the experimental points in Fig. 6.5. Using the matrix coefficients A and B of Fig. 6.4, a model with Eq. (5.6) can be built. It is represented in Fig. 6.5 by the thick continuous line, for $\sigma_{x_i} = 50$ μm and a source

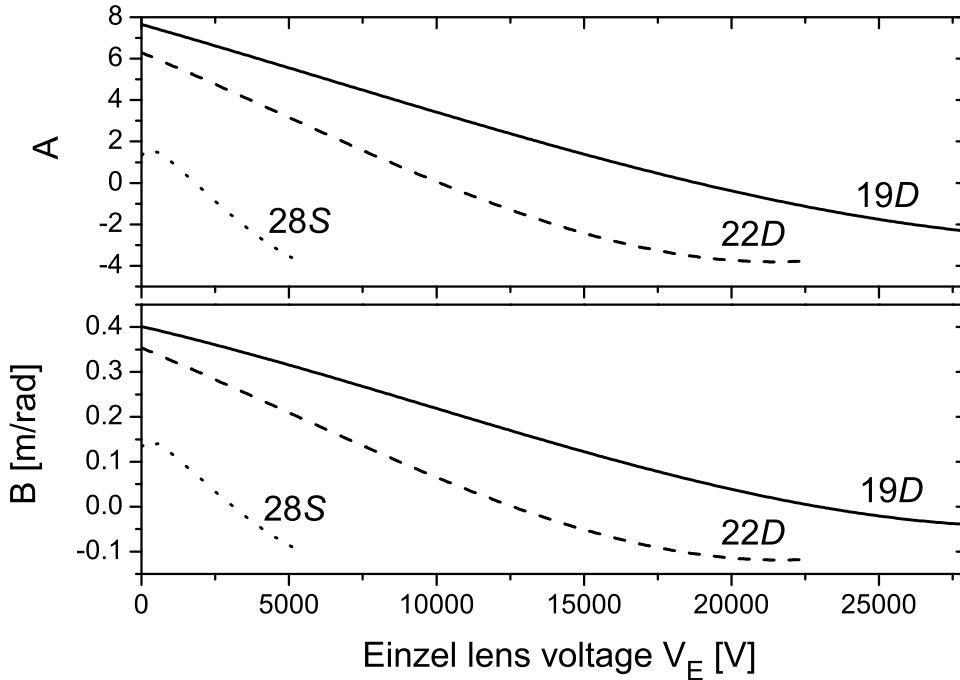


Figure 6.4: A representation of the A and B coefficients as function of the voltage on the Einzel lens. The continuous line is for the 19D Rydberg state, the dashed line for the 22D state, and the dotted line for the 28S state.

temperature $T = 15$ K. It can be seen that the model does not match the experiment at all. A much better match between the experimental points and the model is achieved when the lens voltage V_E is decreased by a factor of two in the model calculation. The resulting model curve is shown as the thin solid line in the figure. Also, for comparison, two additional model lines for which V_E is scaled in the same way by a factor of two are added to this figure, one for $T = 0$ K (dashed) and $T = 30$ K (dotted).

From Fig. 6.5 it can be seen that up to $V_E = 1500$ V, there is not a very good match between the adjusted experimental data points and the model. The model shows a focusing action of the lens, but the experimental points show no modification. Above 1500 V, the model follows the adjusted experimental points quite well. Adjustment of V_E was the only way we could get an approximate fit. However, we have no explanation for it at this moment. Given these discrepancies it is difficult to extract a precise source temperature from this measurement. Comparing the adjusted model curve with the experimental data, we conclude that a source temperature of ≈ 15 K as we obtained in the experiments described in the previous chapters, is at least consistent with the data.

Next, with the wavelengths of 485.03 nm and 487.27 nm, the 22D and 19D Rydberg states are excited, respectively. To field ionize these states, the supply that switches 30 kV in 30 ns is used. The kinetic energy in this experiment cannot be obtained from the rotation

angle, because the energy here is outside the range of the calibration. Given the good match in the previous experiment, we use the kinetic energy U calculated for an adiabatic field ionization (see Table 6.2). Again different voltages are set on the Einzel lens and a scan of the beam size as function of V_E is carried out. The experimental points are given in Figs. 6.6 and 6.7. Using the specific matrix coefficients for each state (Fig. 6.4), a model with Eq. (5.6) can be built. It is represented in these two figures by the continuous lines, for $\sigma_{x_i} = 50 \mu\text{m}$, and $T = 1000 \text{ K}$. To obtain this match, the corresponding voltage on the Einzel lens had to be divided by a factor of 1.7, not so far off from the previous value 2. The model without this additional factor is shown in Figs. 6.6 and 6.7 as the thick line. It can be seen that, without this adjustment, the model does not match the experiment at all.

From Figs. 6.6 and 6.7 it can be seen that the model matches the experiments for voltages below 6 kV and 12 kV, respectively. Above these voltages, the model does not follow the experimental points very well, even if the general behavior seems to be the same. Also, the source temperature $T = 1000 \text{ K}$ is very high compared to all of our previous results, such as the one measured for the $28S$ Rydberg state. If a temperature of 15 K is set in the model, the dashed lines in Figs. 6.6 and 6.7 are obtained; obviously these do not describe the data.

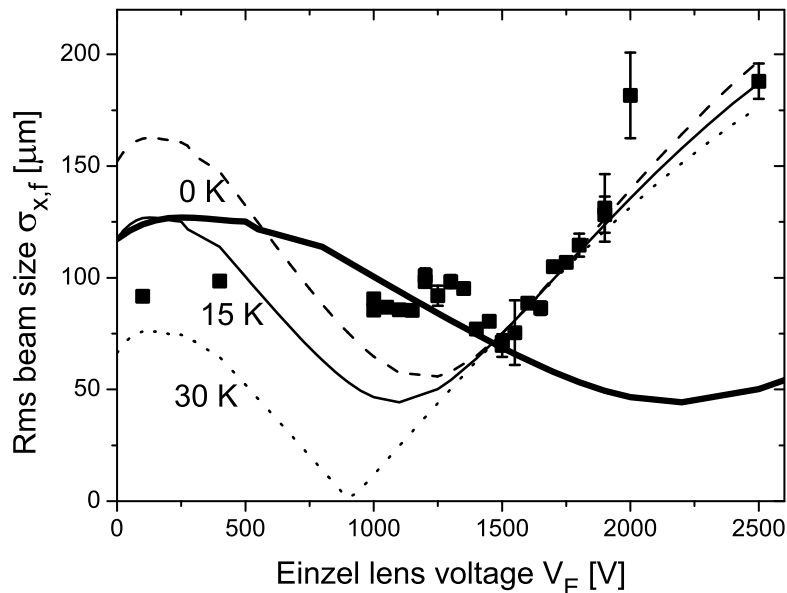


Figure 6.5: Small axis size of the bunch for the $28S$ Rydberg state as function of the voltage applied on the Einzel lens. The continuous line represents the optical model for 15 K , the dashed line for 0 K and the dotted line for 30 K . The thick continuous line represents the model without the adjustment factor discussed in the text.

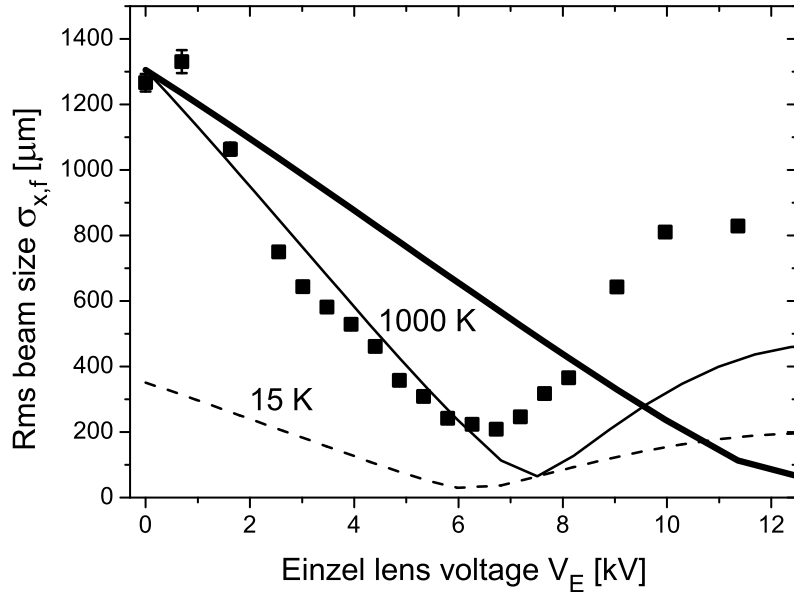


Figure 6.6: Small axis size for the $22D$ Rydberg state as function of the voltage on the Einzel lens. The continuous line represents the optical model for a temperature of 1000 K, the dashed line represents the optical model for 15 K. The thick line represents the optical model without the adjustment factor discussed in the text.

6.5 Conclusions

In the experiments reported here, we have found a method to produce bunches with kinetic energy up to 14 keV. Rydberg atoms with the principal quantum number n between 15 and 28 have been employed to produce electrons by field ionization. This method offers the possibility to produce bunches with a very short length.

Because the kinetic energies are higher than in the previously described experiments, an Einzel lens is used to focus the bunches on the detector. A scan of the beam waist as function of the voltage applied on the Einzel lens is carried out. The optical model has been adapted to the new system and used to calculate the electron temperature at the source. We have found that there are major discrepancies in the measurements reported here. One concerns the strengths of the Einzel lens, which seems to deviate a factor of two from the calculated value. Another is the apparent source temperature, which instead of 15 K comes out to be somewhere near 1000 K.

Both effects are not understood at this moment. The mismatch between the data and the model might be caused by different effects. One might be the aberrations in the lens that are caused by misalignment. Another might be the energy spread in the electron bunch that induces chromatical aberrations. The latter might explain the minimum size of the bunch that in the experiment cannot be achieved. Therefore, we conclude that

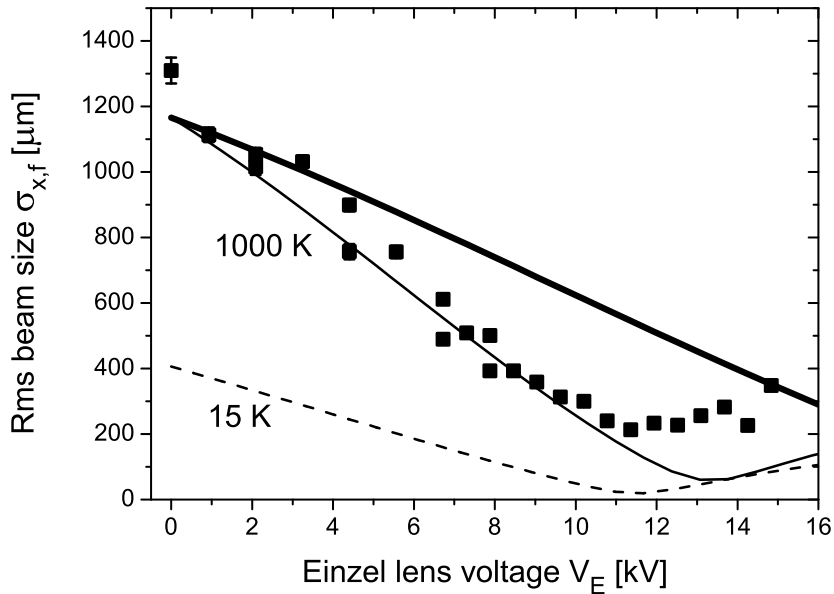


Figure 6.7: Small axis size for the $19D$ Rydberg state as function of the voltage on the Einzel lens. The continuous line represents the optical model for a temperature of 1000 K, the dashed line represents the optical model for 15 K. The thick line represents the optical model without the adjustment factor discussed in the text.

additional research should be carried out to quantitatively explain all these results.

Bibliography

- [1] G. Taban, M.P. Reijnders, S.C. Bell, S.B. van der Geer, O.J. Luiten, and E.J.D. Vredenburg, *Phys. Rev. ST Accel. Beams* **11**, 050102 (2008), Chapter 3 in this thesis.
- [2] H.J. Metcalf and P. van der Straten, *Laser Cooling and Trapping* (Springer, Berlin, 1999).
- [3] T.F. Gallagher, *Rydberg atoms* (Cambridge University Press, 1994).
- [4] <http://www.pulsar.nl/gpt>.
- [5] J.E. Sansonetti, *J. Phys. Chem. Ref. Data* **35**, 301 (2006).
- [6] S. Humphries, Jr., *Principles of Charged Particle Acceleration* (John Wiley and Sons, 1999), pag. 121.
- [7] J.H. Billen and L.M. Young, POISSON SUPERFISH, Los Alamos Nat. Lab. Rep. LA-UR-96-1834.

Concluding remarks

The goal of this project was to develop a new type of electron source based on ultracold plasma. The approach was to increase the angular intensity by lowering the temperature of the source, for moderate values of the emission area. The technique is based on trapping and cooling rubidium atoms in a MOT. To obtain a UCP, the atoms are photoionized just above threshold. Assuming that about 10^{10} atoms are ionized from a $\sigma = 1$ mm cloud and the electron temperature is $T = 10$ K, bunches with $Q = 1$ nC charge and $\varepsilon = 0.04$ mm mrad emittance could be extracted. If the emittance is not degraded and bunch compression to 100 fs temporal length can be reached, then the estimation shows that a transverse brightness of about 6×10^{16} A/(m² sr) can be produced.

Here, in this Thesis, the first steps towards this goal are reported. A few important achievements result from this research project and are summarized in Table 7.1. A new accelerator, together with a high voltage switch, were specially developed for this project. The most important result is that an electron source with a 30 μ m rms size, temperature of 10 K, and normalized transverse emittance of 0.001 mm mrad has been realized. Electron bunches with charges up to 10 fC and kinetic energies up to 14 keV have been produced. An upper limit for the FWHM bunch length of 2 ns has been established. On the basis of these numbers, a transverse brightness $B_{\perp} = 8 \times 10^{10}$ A/(m² sr) can be calculated, which is about 6 orders of magnitude away from the "ultimate limit" of 6×10^{16} A/(m² sr).

Table 7.1: The first experimental results of the present research project and the prospects for a new type of ultracold source.

Source	Rms size σ_x	Temp. T [K]	Charge Q	Bunch length σ_t	Emittance ε [mm mrad]	Brightness B_{\perp} [A/(m ² sr)]	Ref.
Pulsed 1	50 μ m	15	10 fC	2 ns	0.0025	8×10^9	Ch. 4
Pulsed 2	30 μ m	10	10 fC	0.85 ns	0.0012	8×10^{10}	Ch. 5
DC-RF		10	100 fC	100 fs	0.001	1×10^{16}	Ch. 7

7.1 Improvements and limitations

To further improve the brightness of this source, one has to look at the definition of brightness of Eq. (1.11) and see that this can be accomplished by improving either the source temperature T , the charge column density $Q/(\sigma_x\sigma_y)$, the bunch length σ_t , or a combination of these. Each of these parameters is discussed below.

Temperature. Temperature source measurement is practically no issue because, if we want to employ the UCP as source of cold electrons, the temperature will be limited to 10 K, the same order of magnitude as measured here. The temperature measurement of electrons extracted from UCP show that, due to the heating effects discussed in Chapter 2, electrons with about 10 K temperature can be produced at densities of 10^{18} m^{-3} [1]. In our experiment described in Chapter 4, an upper limit for the source temperature has been measured to be 15 K. Therefore the initial goal is actually achieved.

Because we do not use the UCP as a source of cold electrons in this experiment, it should be possible to produce electrons with a lower temperature. Here, instead of a UCP, we directly photoionize the cold atoms and extract electrons immediately after they are created. In the photoionization process, the accuracy with which the wavelength of the ionization laser can be set is 0.001 nm. Therefore electrons with an excess energy of only $5 \mu\text{eV}$ should be produced, meaning a minimum temperature of about 50 mK. Because in both experiments described in Chapters 4 and 5 an upper limit in the same range of 10 - 15 K has been found, we conclude that in our measurements we are limited by the experimental setup rather than by a fundamental limit.

As explained in Chapter 4, different effects that might limit the minimum detectable temperature have been investigated via simulations with GPT. The effect of space-charge, ionization in a finite magnetic field, uncertainty in A and B coefficients of the optical model, electron - atom and electron - ion interactions, aberrations in beam transport, and MCP saturation are phenomena that have been investigated in detail. All these effects show an influence on the minimum detectable temperature, but the differences are very small, in the order of 1 K, and cannot fully explain the lowest temperatures measured in the experiment of ~ 10 K.

Charge column density. In the experiments described in this Thesis we have limited ourselves to bunch charges of maximum 10 fC to prevent emittance degradation due to space-charge effects. To minimize the space-charge effects, the trapped atoms should be excited with a spatially shaped laser beam so as to create a uniformly filled ellipsoidal charge density distribution. It is shown in [2] that such an ellipsoidal bunch has perfectly linear self-fields and thus zero space-charge-induced emittance growth. As a result, more charge may be extracted from the MOT.

The number of atoms and the density of the trapped cloud was fairly low in this experiment, about 10^8 atoms with a maximum density of 10^{15} m^{-3} . The practical maximum that can be achieved, 10^{10} atoms with a peak density of about 10^{18} m^{-3} , is reported in [3]. To produce bunches with more charge, the density of the trapped atom cloud should therefore be increased. The number of atoms trapped in a cloud depends on the loading rate R_L , that is proportional to the density of the atoms in the background vapor n_{BG} , and

on the life time τ of a MOT, that is inversely proportional to the linear loss rate due to collisions with the background gas Γ_{BG} . In the present experiment the atoms were trapped from the background vapor. The measured loading rate was 5×10^7 atoms/s, and the lifetime 3 s.

In a background vapor cell the two parameters are correlated. To be able to separately control them, a solution is to load the actual trap with an additional slow atomic beam, and not as up to now from the vapor pressure. Our choice was to employ a 2D-MOT construction that loads the present 3D-MOT. A standard 2D-MOT consists of two pairs of counterpropagating laser beams that intersect at the center of a two-dimensional quadrupole field. Atoms from the background vapor are cooled and driven towards the axis. The atoms moving along the axis exit through a small hole and go into the chamber where they are trapped in the 3D-MOT. This 2D-MOT is already implemented in the setup and its characterization is reported in [4]. It boosts the loading rate R_L to 5×10^8 atoms/s, and increases the lifetime to 10 s. This additional atom beam can therefore increase the atom number and density by a factor of $\simeq 30$, leading to an increase in brightness by the same factor.

The essential parameter for improving brightness is the charge column density $Q/(\sigma_x\sigma_y)$ (see Eq. (1.11)). From an atom cloud with an rms size $\sigma = 1$ mm and a peak density $n = 10^{18} \text{ m}^{-3}$, about 10^{10} electrons can be extracted, meaning bunches with $Q = 1$ nC charge. The maximum charge column density is therefore about $1 \times 10^{-3} \text{ C/m}^2$. In the experiments reported in this Thesis only a cylinder-like shape is ionized from the entire cloud of trapped atoms. The cylinder contains bunches with 10 fC charge and has an rms radius of $50 \mu\text{m}$ and an rms length of 1 mm given by the atom cloud. This means a column charge density of about $2 \times 10^{-7} \text{ C/m}^2$. Instead of ionizing a vertical cylinder as in this experiment, one can instead ionize a cylinder in the horizontal direction, the so-called "cigar" shape from Chapter 2. Because in this case the entire ionization volume has a projected rms size of $50 \mu\text{m}$ in the radial direction, much smaller than previously, the column charge density for 10 fC is increased to about $4 \times 10^{-5} \text{ C/m}^2$. It means that even without increasing the density, simply choosing another geometry, an increase of ~ 100 times is possible. If at the maximum density of 10^{18} m^{-3} a charge of 250 fC is extracted from the cigar, a surface charge density equal to $1 \times 10^{-3} \text{ C/m}^2$ can be obtained.

The charge column density is, in conclusion, an important parameter to be improved because it can give a significant increase in brightness.

Bunch length. In Chapter 5, we have reported an upper limit of the measured bunch length σ_t at the detector of 2 ns FWHM, probably limited by the response time of the electronics. In Chapter 3 the bunch length on the detector has been shown to be expected in the order of tens of ps. In Chapter 5 it is also discussed that bunch lengths nearer to ~ 50 ps should be expected. Therefore, to further characterize this source, the bunch length should be measured with ps resolution. Efforts are made in this direction by an additional project in our group, together with the Electrotechnical Engineering Department of our university, to develop an electron bunch auto-correlator [5]. It should be further tested in practice. Possibly this will result in the capability of measuring smaller bunch lengths of 1-100 ps in the present setup, and thus higher brightness values.

A possible alternative to measure the bunch length is with a streak cavity. In a streak, an incoming bunch is deflected sideways by a rapidly varying field, in such a way that the front of the bunch is deflected more than the back, or vice versa. This gives the bunch a lateral size which depends on its original duration. This lateral size can be measured on a phosphor screen with the help of a CCD camera. The bunch length can be calculated when the deflecting force is properly characterized. A streak cavity has been built in our group for a different experiment [6]. If one wants to characterize the bunches obtained in the present experiment, a new dedicated cavity should be designed.

In Chapter 2 it has been shown via simulations that a minimum bunch length of 20 fs can be achieved when an accelerating voltage of 1 MV can be turned on in 150 ps. Also for a more realistic setup it has been shown in Chapter 3 that a sub-ps bunch length can be obtained when an accelerating voltage of 30 kV can be turned on in 30 ns. The simulations point out that, to obtain a shorter bunch length, the slew rate of the electric field should be made as large as possible. Due to a faster variation of the electric field with the time, the kinetic energy of the beam would be higher. A higher kinetic energy means automatically a shorter temporal bunch length.

Here the minimum length is reached at a few centimeters after the acceleration point, which is not very practical for applications. A practical solution to obtain short bunches at a more accessible axial position is to compress the bunch after extraction. It can be done downstream on the beam line, using a time-dependent electric field in an oscillating radio-frequency cavity. Such a solution has been proposed in [7]. The idea behind it is to apply an electric field such that the front particles are decelerated, while at the rear the particles are accelerated. This leads to ballistic compression in the subsequent drift space. The field ramp needs to be timed very accurately, in accordance with the bunch, and its characteristics should be adapted to the present parameters of the bunch.

The bunch length is in conclusion an important parameter to be improved. Firstly by improving the temporal resolution of the diagnostics and secondly by trying to produce shorter bunches.

7.2 New directions opened by this project

The experiments reported in this Thesis provide a solid basis for the next generation of cold electron sources [8], that combines the present source based on cold atoms with the radio-frequency technology. As in the project described here, a laser cooled and trapped cloud of atoms is photoionized. The difference is that, after an ultracold plasma is produced, instead of a pulsed electric a combination of DC and RF fields is used, which provides a new way to create the fast-rising high electric field originally envisioned in Chapter 2. Via GPT simulations it is shown that in this new setup 120 keV, 0.1 pC, 100 fs bunches can be produced, with 0.001 mm mrad transverse emittance and 1×10^{16} A/(m² sr) brightness. This brightness is sufficiently high to make possible single shot ultrafast electron diffraction experiments of large biomolecular samples.

If one changes the sign of the electric field inside the accelerator, the extracted particles

are ions instead of electrons. The ion bunches that result from this process can have a very low energy spread. This ion beam can be used for a Focused Ion Beam source, with applications in nanotechnology and mass spectrometry. The feasibility of this ultracold ion source was numerically investigated [9] and it has been shown that it has the potential for generating ion beams which combine high brightness with small energy spread. The first practical investigation shows via time-of-flight measurements that an ion beam with a longitudinal energy spread as low as 0.02 eV can be produced [10]. This is two orders of magnitude lower than the state-of-the-art liquid-metal ion sources used at this moment.

Summarizing, in this project important steps were made towards a bright electron source based on cold atoms. In addition, with this technique new research directions have been opened, as illustrated by the experiment with cold ions.

Bibliography

- [1] J.L. Roberts, C.D. Fertig, M.J. Lim, and S.L. Rolston, *Phys. Rev. Lett.* **92**, 253003 (2004).
- [2] O.J. Luiten, S.B. van der Geer, M.J. de Loos, F.B. Kiewiet, and M.J. van der Wiel, *Phys. Rev. Lett.* **93**, 094802 (2004).
- [3] W. Ketterle, K.B. Davis, M.A. Joffe, A. Martin, and D.E. Pritchard, *Phys. Rev. Lett.* **70**, 2253 (1993).
- [4] D.J.N. Kusters, MSc Thesis (Eindhoven University of Technology, The Netherlands, 2008).
- [5] S.J. Voeten, private communication.
- [6] J.R. Nohlmans, MSc Thesis (Eindhoven University of Technology, The Netherlands, 2007).
- [7] T. van Oudheusden, E.F. de Jong, S.B. van der Geer, W.P.E.M. Op 't Root, O.J. Luiten, and B.J. Siwick, *J. Appl. Phys.* **102**, 093501 (2007).
- [8] S.B. van der Geer, M.J. de Loos, E.J.D. Vredenburg, and O.J. Luiten, submitted to *Microscopy and Microanalysis* (2008).
- [9] S.B. van der Geer, M.P. Reijnders, M.J. de Loos, E.J.D. Vredenburg, P.H.A. Mutsaers, and O.J. Luiten, *J. Appl. Phys.* **102**, 094312 (2007).
- [10] M.P. Reijnders, P.A. van Kruisbergen, G. Taban, P.A.H. Mutsaers, E.J.D. Vredenburg, and O.J. Luiten, *Phys. Rev. Lett.* **102**, 034802 (2009).

Summary - A Cold Atom Electron Source

Pulsed bright electron sources offer the possibility to study the structure of matter in great spatial and temporal detail. An example of an indirect method is to generate hard X-ray flashes with high brilliance, a new Free Electron Laser facility is under construction. It requires an electron source with a very high quality. Electron beams may also be used directly to study matter with, e.g., ultrafast electron diffraction. This also requires a pulsed electron source with high brightness. An overview of experiments that require a bright electron source is presented in Chapter 1. Also the pulsed electron sources used at this moment, i.e., photo-emitters and field-emitters, are described in Chapter 1.

Brightness is an important figure of merit for electron source quality. It is expressed in its most general form as the current density per unit solid angle and unit energy spread. Recent brightness improvements are based on increasing the current density at the source, but this is not sufficient for all types of experiments. A new type of source, based on ultracold plasma, is described in Chapter 2. Contrary to the usual approach to increase the current density at the source to obtain a higher brightness, the new method tries to increase the angular intensity for moderate values of the emission area. For the field-emitters and photo-emitters the effective electron temperature of the source is typically $10^3 - 10^4$ K. If one is able to lower these temperatures at the source, then a gain in brightness proportional to the reduction of the temperature can be achieved for the same current density. The new source concept based on this idea proposes pulsed extraction of electrons from an ultracold plasma, that is created from a laser-cooled cloud of neutral atoms by photoionization just above threshold. These plasmas are characterized by electron temperatures of 10 K. A simple estimate serves to illustrate the possible performance of such a source. Laser-cooled atomic clouds can have central densities up to $n = 10^{18} \text{ m}^{-3}$ and contain up to 10^{10} atoms, requiring a cloud with rms (root-mean-square) size $\sigma = 1$ mm. If all these atoms could be ionized to form a UCP (ultracold plasma) with an electron temperature $T = 10$ K, then an electron bunch with a charge $Q = 1$ nC and an emittance $\varepsilon = 0.04$ mm mrad could be extracted. If, in addition, all of these electrons can be packed into a temporal bunch length on the order of $\sigma_t = 100$ fs, the transverse brightness of the resulting electron bunch would be $B_{\perp} = 6 \times 10^{16} \text{ A}/(\text{m}^2 \text{ sr})$. This is a few orders of magnitude higher than what has been achieved so far in the regime of (sub)-ps electron bunches.

A four-step procedure is used to realize a UCP-based electron source in practice. First, atoms are cooled and trapped in a magneto-optical trap. Second, part of the cold atom

cloud is excited to an intermediate state with a quasi-continuous laser pulse. Third, a pulsed laser beam propagating at right angles to the excitation laser ionizes the excited atoms only within the volume irradiated by both lasers. Subsequently, a UCP is formed. Finally, the electrons of the UCP are extracted by an externally applied electric field pulse.

Each step toward the ultracold plasma is explained in detail in Chapter 2. Subsequently, with the help of simulations with a particle tracking program, the expectations from a more realistic situation are investigated. Two geometries are discussed. First, an initial charge distribution called "pancake" (bunch length much smaller than its transversal size) with a half-circle radial charge density distribution offers for a beam transverse size of 2 mm an emittance of 0.1 mm mrad and a temporal bunch length of 150 fs. This results in a transverse brightness of 6×10^{13} A/(m² sr). Second, a "cigar" geometry (transverse size much smaller than bunch length) with a parabolic longitudinal charge density distribution offers for a beam transverse size of 1 mm an emittance of 0.07 mm mrad and a temporal bunch length of 20 fs. This results in a transverse brightness of 1×10^{14} A/(m² sr).

In this Thesis the first practical steps are reported towards this new concept. In Chapter 3, a specially designed accelerator structure and a pulsed power supply are described. They are essential parts of a high brightness cold atoms-based electron source. The accelerator structure allows a magneto-optical atom trap to be operated inside of it, and also transmits sub-nanosecond electric field pulses. The power supply produces high voltage pulses up to 30 kV, with a rise time of up to 30 ns. The resulting electric field inside the structure is characterized with an electro-optic measurement and with an ion time-of-flight experiment.

In Chapter 4 measurements of the transverse momentum spread of pulsed electron beams are presented. Rubidium atoms are cooled and trapped in a magneto-optical trap. A small cylinder of these atoms is photoionized, resulting in free electrons. The electrons are extracted by a DC electric field. Images of the cylinder-like electron beam are obtained on the detector. On the path that they travel to a phosphor screen, they interact with an electromagnetic beam transport system, composed of an electrostatic lens (the accelerator itself) and a magnetic lens (the trapping coils). Due to the magnetic lens, this optical system is energy dependent. A dependence between the size of the small axis of the cylinder at the detector and the beam kinetic energy is obtained. With the help of an optical matrix that describes this electromagnetic system, the size of the cylinder is related to the initial electron temperature, which is the parameter that we are actually interested in. Transverse electron temperatures ranging from 200 K down to 15 K are demonstrated, easily controllable with the wavelength of the ionization laser. The temperature is influenced due to the Stark effect by the presence of the accelerating electric field. In this experiment the temporal length of the bunch is limited by the length of the ionization laser pulse to 4.7 ns. A typical bunch contains a charge of 10 fC.

To lower the bunch length, another experiment was carried out. The results are presented in Chapter 5. This time, excited Rydberg states of rubidium atoms are field ionized. The atoms are first magneto-optically trapped at the center of the accelerator structure. Subsequently they are excited to a Rydberg state (here between 26 and 35) and then field ionized by a pulsed electric field with a slew rate of 58 (V/cm)/ns. Electron temperatures

at the source on the order of 10 K are measured. In the same way as in Chapter 4, the temperature is deduced from images of the electron pulses on the phosphor screen, using a model of the beam transport system. An advantage of this method is that sub-ns temporal bunch lengths might be reached. Here, the length is measured to be 2 ns FWHM, which is limited by instrumental resolution; particle tracking simulations show that it might be on the order of tens of ps.

As a continuation of the experiments presented in Chapter 4 and 5, a method to produce electron bunches with high energy and low temperature at the source is presented in Chapter 6. Rydberg atoms with the principal quantum number n between 15 and 25 are employed. It is shown that energies up to 14 keV can be produced. An Einzel lens is employed to focus the beam on the detector. An optical model including the Einzel lens is built, this time with the transverse beam size at the detector being dependent on the voltage applied on the Einzel lens. It does not fit very well the expectations due to the work of the Einzel lens, but this is a new model that can be further used to describe the behavior of a bunch in an optical system. Source temperatures of about 15 K are expected, but an upper limit of 1000 K is estimated using the optical model.

In conclusion, in this Thesis an electron source with a 30 μm rms size, temperature of 10 K, and normalized transverse emittance of 0.001 mm mrad has been produced. Electron bunches with charges up to 10 fC and kinetic energies up to 14 keV have been produced. An upper limit for the FWHM length of 2 ns has been established. On the basis of these numbers, a transverse brightness $B_{\perp} = 8 \times 10^{10}$ A/(m² sr) can be calculated.

To further improve the brightness of this source, the source parameters as the charge column density $Q/(\sigma_x\sigma_y)$, the bunch length σ_t , and the source temperature T should be improved. Together they may improve the brightness a few orders of magnitude.

This project provides a solid basis for the next generation of cold electron sources that combines the present source based on cold atoms with radio-frequency technology. In addition, with this technique new research directions have been opened, as illustrated by an experiment with cold ions.

Samenvatting - Een elektronen bron van koude atomen

Gepulste elektronenbronnen geven de mogelijkheid om, direct of indirect, de structuur van materie te bestuderen tot in de kleinste details, zowel in de ruimte als in de tijd. Er wordt bijvoorbeeld een nieuwe Free Electron Laser faciliteit opgericht om harde X-rays met grote helderheid te produceren. Deze faciliteit vereist een elektronenbron met een hoge kwaliteit. Elektronenbundels kunnen ook direct gebruikt worden om materie te bestuderen, bijvoorbeeld door ultrasnelle elektronen diffractie. Deze methode vereist ook een elektronenbron met hogere helderheid. Een overzicht van experimenten die een elektronenbron met een hogere helderheid vereisen wordt in Hoofdstuk 1 gepresenteerd. Ook de gepulste elektronenbronnen die op dit moment in gebruik zijn, photo-emitters en veld-emitters, worden in Hoofdstuk 1 kort beschreven.

Helderheid is een belangrijk maat voor de kwaliteit van een elektronenbron. In algemene zin is het de stroomdichtheid per eenheid ruimtehoek en per eenheid energiespreiding. Tot nu toe zijn helderheidsverbeteringen gebaseerd op het verhogen van de stroomdichtheid bij de bron, maar dit is niet genoeg voor alle verschillende soorten experimenten. Een nieuw type bron, gebaseerd op een ultrakoud plasma, is beschreven in Hoofdstuk 2. Deze bron heeft niet als doel om de stroomdichtheid te verhogen, maar probeert om de ruimtehoek intensiteit te verbeteren zonder het oppervlak van de bron drastisch te verkleinen. Voor veld-emitters en photo-emitters is de effectieve elektronentemperatuur bij de bron typisch $10^3 - 10^4$ K. Als men de temperatuur bij de bron kan verlagen, kan voor gelijke stroomdichtheid een winst in helderheid bereikt worden die omgekeerd evenredig is met de temperatuur. Het nieuwe bronconcept gebaseerd op dit idee stelt voor om elektronen gepulst te extraheren uit een ultrakoud plasma. Het plasma wordt gecreëerd door een wolk neutrale atomen te koelen met een laser, gevolgd door fotonionisatie van de atomen net boven de ionisatie drempel. Dergelijke plasma's worden gekarakteriseerd door elektronentemperaturen van 10 K. Een simpele schatting illustreert de mogelijke prestatie van deze bron. Laser-gekoelde atoomwolken kunnen maximale dichtheden tot $n = 10^{18} \text{ m}^{-3}$ hebben en kunnen tot 10^{10} atomen bevatten. De wolk heeft dan een rms afmeting van $\sigma = 1$ mm. Als alle atomen in de wolk geïoniseerd kunnen worden om zo een ultrakoud plasma met elektronentemperatuur $T = 10$ K te vormen, dan kan er een elektronenpuls uitgehaald worden met een lading $Q = 1$ nC en emittantie $\varepsilon = 0.04$ mm mrad. Als bovendien al deze elektronen zich in een puls bevinden van ongeveer $\sigma_t = 100$ fs, dan is de transversale helderheid van deze elektronen puls $B_{\perp} = 6 \times 10^{16} \text{ A}/(\text{m}^2 \text{ sr})$. Dit is vele malen hoger dan

wat tot nu toe bereikt is op het gebied van (sub)-ps elektronen pulsen.

Een vier-stappen procedure is gebruikt om in de praktijk een elektronenbron gebaseerd op een ultrakoud plasma te maken. Eerst zijn de atomen gekoeld en opgesloten in een magneto-optische val. Daarna is een deel van de koude atomen in de wolk geëxciteerd naar een intermediaire toestand met een quasi-continue laser puls. Vervolgens ioniseert een gepulste laser bundel, die loodrecht staat op de excitatie laser, de geëxciteerde atomen alleen in het volume waar de twee lasers overlappen. Zo is een ultrakoud plasma gecreëerd. Tenslotte zijn de elektronen uit het ultrakoude plasma gehaald door een puls van een extern elektrisch veld.

Iedere stap om het ultrakoude plasma te maken is in detail uitgelegd in Hoofdstuk 2. Vervolgens zijn de verwachtingen van een meer realistische situatie onderzocht met behulp van simulaties met een deeltjes trekker programma. Twee verschillende initiële ladingsverdelingen worden bediscussieerd. De eerste verdeling wordt "pannekoek" genoemd (puls lengte kleiner dan zijn transversale afmeting). Met een radiële halve-cirkel ladingsdichtheidverdeling en een bundel oppervlak van 2 mm resulteert deze geometrie in een puls met een emittantie van 0.1 mm mrad en een duur van 150 fs. De transversale helderheid is 6×10^{13} A/(m² sr). De tweede verdeling is een "sigaar" geometrie (transversale afmeting veel kleiner dan de puls lengte) met een parabolische longitudinale ladingsdichtheidverdeling. Voor een transversale afmeting van 1 mm heeft deze puls een emittantie van 0.07 mm mrad en een lengte van 20 fs. Bijgevolg is de transversale helderheid 1×10^{14} A/(m² sr).

In dit proefschrift worden de eerste praktische stappen naar dit nieuwe concept beschreven. In Hoofdstuk 3 worden een speciaal ontworpen versneller en een gepulste hoogspanningsvoeding beschreven. Dit zijn essentiële onderdelen van een heldere elektronenbron, die gebaseerd is op koude atomen. De versneller is zo ontworpen dat er een magneto-optische val in opgebouwd kan worden en dat sub-nanoseconde elektrische veld pulsen geleid worden. De voeding produceert hoogspanningspulsen tot 30 kV met een stijgtijd tot 30 ns. Het resulterende elektrische veld binnen de versnelstructuur is gekarakteriseerd met een elektro-optische meting en met een 'time-of-flight' experiment met ionen.

In Hoofdstuk 4 worden metingen van de transversale impulsverspreiding van gepulste elektronen bundels gepresenteerd. Deze bundels zijn gemaakt door eerst rubidium atomen te koelen en op te sluiten in een magneto-optische val. Een kleine cilinder van deze atomen is gefotoïoniseerd, zodat een cilinder met vrije elektronen ontstaat. De elektronen zijn uit het ultrakoude plasma gehaald met een DC elektrisch veld. Beelden van deze cilindrische elektronenbundels zijn verkregen met een fosfor detector. Op hun pad naar het fosfor scherm reageren de elektronen met een elektrostatisch lens (de versneller zelf) en een magnetisch lens (de spoelen van de magneto-optische val). Vanwege de magnetisch lens is dit optisch systeem afhankelijk van de snelheid van de elektronen. Een afhankelijkheid tussen de kleine as van de cilinder op de detector en de kinetische energie van de bundel is verkregen. Met behulp van een matrix, die dit elektromagnetische systeem beschrijft, is de maat van de cilinder gerelateerd aan de initiële elektronentemperatuur. Dat is de parameter die ons eigenlijk interesseert. Transversale elektronentemperaturen van 200 K tot 15 K zijn op deze manier gedemonstreerd. De temperatuur is gemakkelijk instelbaar met de golflengte van de ionisatie laser. De temperatuur wordt beïnvloed via het Stark effect door de aanwezigheid

van het versnelveld. In dit experiment is de duur van de elektronenpuls gelimiteerd door de lengte van de ionisatie laser puls tot 4.7 ns. Een typisch puls heeft een lading van 10 fC.

Om de puls korter te maken is een ander experiment uitgevoerd. De resultaten worden gepresenteerd in Hoofdstuk 5. Dit keer zijn geëxciteerde Rydberg toestanden veld geïoniseerd. De atomen zijn eerst magneto-optisch opgesloten in het centrum van de versnelstructuur. Vervolgens zijn ze naar een Rydberg toestand geëxciteerd (hier tussen 26 en 35) en daarna veld geïoniseerd door een gepulst elektrisch veld met een stijging van 58 (V/cm)/ns. Elektronen temperaturen bij de bron van 10 K zijn gemeten. Op dezelfde manier als bij het vorige experiment is de temperatuur af te leiden uit de beelden van de elektronenpulsen op het fosfor scherm. Een voordeel van het tweede experiment is echter sub-ns puls duren bereikt kunnen worden. Er zijn pulsduren gemeten van 2 ns FWHM, maar deze metingen zijn gelimiteerd door de beperkte resolutie van de diagnostiek; simulaties laten zien dat de pulsen ongeveer tientallen ps kort zouden kunnen zijn.

Als vervolg op de experimenten gepresenteerd in Hoofdstukken 4 en 5 wordt in Hoofdstuk 6 een methode beschreven om elektronenbundels met hoge energie en een lage temperatuur bij de bron te maken. Rydberg atomen met een hoofdkwantumgetal n tussen 15 en 25 zijn gebruikt. Het is experimenteel aangetoond dat energieën tot 14 keV geproduceerd kunnen worden. Een Einzel lens is gebruikt om de bundel op de fosfor detector te focussen. Een optisch model inclusief de Einzel lens is gebruikt om de elektronentemperatuur te bepalen. Het model komt niet goed overeen met de verwachtingen vanwege het gedrag van de Einzel lens. Maar dit is een nieuw model dat verder kan gebruikt worden om het gedrag van een puls in een optisch systeem te beschrijven. Brontemperaturen van ongeveer 15 K zijn verwacht, maar een boven limiet van 1000 K is geschat met behulp van het optische model.

Samengevat is in dit proefschrift een elektronenbron met een 30 μm rms afmeting, een temperatuur van 10 K en een genormaliseerde transversale emittantie van 0.001 mm mrad gemeten. Elektronen bundels met lading tot 10 fC en kinetische energieën tot 14 keV zijn gemaakt. Een bovengrens van de pulsduur van 2 ns is vastgesteld. Op basis van deze getallen is een transversale helderheid van $B_{\perp} = 8 \times 10^{10}$ A/(m² sr) berekend.

Om de helderheid van deze bron verder te verhogen, moeten de bron parameters verbeterd worden, zoals de kolom ladingsdichtheid $Q/(\sigma_x\sigma_y)$, de pulsduur σ_t en de bron temperatuur T . Samen kunnen ze de helderheid een paar ordes verbeteren.

Dit project levert een solide basis voor de volgende generatie van koude elektronen bronnen, die de huidige koude bron combineert met microgolf technologie. Bovendien zijn met deze techniek nieuwe onderzoeksrichtingen geopend, zoals een experiment met koude ionen.

Dankwoord

Toen ik voor de eerste keer in een proefschrift naar het Dankwoord heb gekeken vond ik het niet zo indrukwekkend. Nu ik zelf zover ben, denk ik dat het best leuk en belangrijk is om iedereen te bedanken voor wat ze voor mij hebben gedaan in de afgelopen jaren. Dus, terugkijken en, zoals de roeiers zeggen: "Slag klaar maken... slag klaar... go!":

Edgar en Jom: Hartelijk bedankt voor alles wat jullie deze laatste vier jaar voor mij hebben gedaan! Ik kreeg ondersteuning wanneer dat nodig was, hoge kwaliteit discussies over ons project, feedback over resultaten, hulp in het lab, schrijven van artikelen en proefschrift. Dat ons project heel mooie resultaten heeft opgeleverd, heeft veel met jullie invloed te maken.

Herman: Bedankt dat jij me als jouw promovendus hebt aangenomen. Ook bedankt voor de stimulering van persoonlijke ontwikkeling.

Merijn: Bedankt voor de samenwerking, de ontwikkeling en het opbouwen van de nieuwe opstelling, de dagelijkse experimenten en discussies! Een beetje hectisch in het begin, maar daarna heel soepel. Jij had altijd geweldige ideeën en ik weet zeker dat zonder jou dit project in de loop van de tijd zich totaal anders had ontwikkeld. Ik was blij met een collega zoals jij. Bedankt!

Elmer en Bas: Jullie waren "mijn" enige studenten en ik heb veel van jullie geleerd. Ik hoop dat jullie ook van mij hebben geleerd en dat jullie dat verder goed kunnen gebruiken. Geweldig dat jullie mijn paranimfen zullen zijn!

Bas: Bedankt dat je altijd opnieuw voor mij klaar stond om me met GPT, SUPERFISH of MICROWAVE STUDIO te helpen. Ook de "conceptuele" discussies waren altijd een plezier en uitdaging voor de geest.

De CQT technici: Bedankt voor de ontwerpen van de opstelling en de oplossing van de dagelijkse problemen. Leven zonder jullie was zeker veel moeilijker.

Simon: Thanks, mate! Your time in our lab ment the very first ultracold bunches, but also trekking in Crete and, of course, The Cat Empire!!! Without them my beam time was - for sure - far not so exciting!

CQT collega's (en hier noem ik ook de oude AQT en FTV leden): De lekkere koffie, de uitjes, het voetbal toernooi, de borrels. Ik ben blij dat ik vier jaar in deze groep actief

was. Ik heb mijn best gedaan om "kleurig" te zijn en om jullie stof genoeg te geven voor een grappige film...

Dat ik hier ben was ook mogelijk met behulp van andere mensen die voor mijn wetenschappelijke carrière belangrijk waren. Allereerst mijn begeleider van de VU Amsterdam, *Mark van der Putte*, de eerste die vertrouwen in mij heeft getoond en mij in dit eerste jaar in Nederland (echt fantastisch, trouwens!) ondersteunde. Daarnaast ook *Cees Alderliesten* en *Arie de Jong*, mijn AMS Utrecht-collega's met wie mijn tijd in Utrecht heel plezierig was.

Zoals velen van jullie weten, vormden privé en werk altijd een belangrijke mix voor mij, daarom vind ik het niet gek om veel van mijn vrienden hier te bedanken (Als ik nu in mijn adresboek kijk, is het ongelofelijk hoeveel mensen ik intussen ken! En nog gekker, meer Nederlanders dan Roemenen!).

Ik moet beginnen met mijn allerbeste Nederlandse vrienden, *Betty* en *Thijs*, zonder wie mijn Eindhovens leven totaal anders was (en zeker niet van de positieve kant...). Ik weet niet hoe ik jullie moet bedanken voor alles wat we samen hebben ervaren: hard lachen, ook huilen, veel praten, hard zingen, hard zuipen, grote katers, vaak Plaza, veel films, geweldige concerten, af en toe meisjes, ook jongens, (proberen) dansen, Mundial, nog hoger springen, 19 december, gekke en gedurfde ontwerpen, sollicitatie brieven, eigenlijk van alles wat. Als ik ooit uit Eindhoven ga verhuizen, dan zal ik jullie echt missen! Nu kan ik niet anders zeggen dan: "Op Paul!"

Ancuța en *Iulian*: Jullie waren hier aanwezig vanaf het allereerste moment in Nederland en sindsdien zijn jullie altijd aanwezig geweest, wanneer ik jullie dan ook nodig had. Veel dank!

Ancuței și lui *Iulian*: Ați fost alături de mine chiar din prima mea zi olandeză și de atunci sînteți tot timpul în preajmă oricînd și pentru orice am nevoie de voi. Mulțumesc mult!

Other PhD-students that I have met during some courses: *Maaïke*, *Robert*, *Wojciech* en, last but not least, "my hero" *Hiro*. You were the very first to help me realising who's actually "me". Since that moment my life went on "a little bit" different. Thanks guys, I had a wonderful time with you!

De *Wervingsdagen Commissie 2006-2007*: Meisjes, jongens, van jullie heb ik in een rap tempo veel geleerd en dat gebruik ik nog steeds in mijn dagelijkse leven! Hartelijk bedankt om mij als "de enige buitenlandse AIO ooit" binnen de studenten commissie te accepteren!

Ik moet zeker mijn "zaterdagse roeifamilie" hartelijk bedanken. De mede-instructeurs en leerlingen, maar ook de toertochten- en Elfstedenroeimarathonploegen. Ja, inderdaad, jullie zijn mijn Amsterdamse "familie" en iedere zaterdag kom ik bij Willem III met veel plezier om samen van de geweldige Amstel te genieten. Zonder iets te vermoeden hebben jullie mij op vele moeilijke momenten aangemoedigd en zo kon ik ontdekken dat wat ik doe waardevol is. Hopelijk worden jullie binnenkort mijn "alledaagse familie"! Kan niet wachten!

Anke: Bedankt voor de altijd gezellige dansavonden! Altijd als ik een klein beetje moe of

verdrietig was, wist jij een glimlach op mijn gezicht terug te brengen. Ik ben heel blij dat we zo'n lange tijd samen hebben gedanst!

Mijn allerbeste *Roemeense vrienden* (uit Roemenië of wereldwijd): Ondanks dat ik zelden in de buurt was wist ik dat jullie vlakbij mij waren en wat er ook gebeurt: ik kan jullie zonder nadenken "vrienden" noemen.

Dragilor mei *prieteni români* (din România sau din lumea largă): Chiar dacă nu am fost întotdeauna foarte aproape v-am știut întotdeauna alături și, ca și pîna acum, orice s-ar întâmpla vă pot numi fără să stau pe gînduri: "prieteni".

Mama en oom Costel: Lieverds, in de zeven jaren dat ik ver weg van huis ben, waren jullie altijd dichtbij, in lief en leed, zonder iets terug te vragen. Ondanks dat ik het niet zo vaak zeg, weten jullie dat jullie heel belangrijk voor mij zijn en ik hoop dat ik jullie nooit heb teleurgesteld. Ik weet het zeker dat papa en oma samen met ons zouden genieten van dit "boekje"...

Mamei și lui Costel: Dragilor, în toți cei șapte ani de cînd sînt plecat de-acasă mi-ați fost alături cu bune și rele, fără a cere nimic înapoi. Chiar dacă n-o spun prea des, voi știți că sînteți foarte importanți pentru mine și sper să nu fi făcut vreodată ceva care să vă fi dezamăgit. Sigur tata și mamaia s-ar fi bucurat și ei alături de noi pentru "cărțulia" asta...

Ik kan niet eindigen zonder de allerliefste *I's* van mijn leven te bedanken. Alle tijd die we samen hebben doorgebracht was absoluut geweldig en ik kon niet anders doen dan echt ervan genieten. Door jullie invloed en met dank aan jullie liefde ben ik vandaag zoals ik nu ben. Jullie zullen altijd écht speciaal voor mij blijven!

Hartelijk bedankt! Dit waren zeven geweldige jaren! Spannende tijden komen eraan!!!

Gabriel

Curriculum vitae

- 3 maart 1977 Geboren te Focşani, Roemenië.
- 1992 – 1996 Bacalaureate (VWO equivalent),
National College "Al.I. Cuza", Focşani, Roemenië.
- 1996 – 2000 Bachelor student,
Universiteit van Boekarest, Faculteit Natuurkunde, Roemenië.
- 2000 – 2002 MSc Experimentele Natuurkunde,
Universiteit van Boekarest, Faculteit Natuurkunde, Roemenië,
Elementary Particle Physics Groep.
- 2001 – 2002 MSc Experimentele Natuurkunde,
Vrije Universiteit Amsterdam,
Faculteit Natuur- en Sterrenkunde,
Ion Beam Facility Groep.
- 2003 – 2004 Junior Researcher, Utrecht Universiteit,
Faculteit Natuur- en Sterrenkunde,
Accelerator Mass Spectrometry Groep.
- 2005 – 2008 Onderzoeker in opleiding,
Technische Universiteit Eindhoven,
Faculteit Technische Natuurkunde,
Coherence and Quantum Technology Groep.